

UNIVERSITY OF CALIFORNIA
Los Angeles

A Measurement of Low-Mass Drell-Yan
Production at the Collider Detector at Fermilab

*A dissertation submitted in partial satisfaction of the
requirements for the degree Doctor of Philosophy
in Physics*

by

Andrew Ferrell Scott

2000

The dissertation of Andrew Ferrell Scott is approved.

Edward Hoffman

David Saltzberg

Robert Cousins

Jay Hauser, Committee Chair

University of California, Los Angeles

2000

To my wife, Jennifer,
and my parents.

Contents

List of Figures	vi
List of Tables	ix
Acknowledgements	x
Vita	xi
Abstract of the Dissertation	xiii
1 Introduction	1
1.1 The Drell-Yan Process	1
1.2 Previous Measurements	2
1.3 Analysis Strategy	5
2 Theory	6
2.1 The Naive Parton Model	6
2.2 Higher-Order Contributions	8
2.3 Event Kinematics	10
3 Apparatus	16
3.1 The Fermilab Tevatron	16
3.2 The Collider Detector at Fermilab	19
3.2.1 Vertex Time Projection Chamber (VTX)	20
3.2.2 Central Tracking Chamber (CTC)	21
3.2.3 Calorimetry	22
3.2.4 Central Muon Chambers	24
3.2.5 Trigger	24
4 Event Selection	28
4.1 Electron Identification	28
4.1.1 Electron Identification Efficiency	30
4.2 Muon Identification	34

4.2.1	Muon Identification Efficiency	35
4.2.2	Muon Reconstruction Efficiency	39
4.3	SUSY Dilepton Sample	40
4.4	Drell-Yan Dilepton Sample	41
4.5	Other Efficiencies	44
4.5.1	Isolation Cut	44
4.5.2	Z Vertex Cut Efficiency	46
5	Monte Carlo Simulation	47
5.1	Event Generation	47
5.2	Detector Simulation	48
5.2.1	Electron Detector Simulation	48
5.2.2	Muon Detector Simulation	55
5.2.3	Systematic Uncertainty from Detector Simulation	63
6	Trigger Efficiencies and Detector Acceptance	66
6.1	Trigger Efficiency Determination	66
6.1.1	Data Paths	67
6.1.2	Electron Trigger Efficiencies	70
6.1.3	Muon Trigger Efficiencies	75
6.1.4	Trigger Efficiencies of Mass Bins	79
6.2	Smearing and Detector Acceptance	79
6.2.1	Photon and Transverse Energy/Momentum Smearing	81
6.2.2	Detector Acceptance	82
6.3	Systematic Uncertainties of Detection Efficiency	82
6.3.1	Scaling of the Monte Carlo Lepton Pair p_T	91
6.3.2	Varying the Monte Carlo Structure Function	94
7	Background Analysis	106
7.1	Removal of Cosmic Ray Muons (DIMUCOS)	107
7.2	Subtraction of Misidentification Backgrounds	117
7.3	$Z \rightarrow \tau^+ \tau^-$ Background	117
7.4	Heavy Flavor Background	121
7.5	Summary of Estimated Backgrounds	127
8	Results and Conclusions	128
8.1	Cross-Section Calculation	128
8.1.1	Cross-Section Results	134
8.2	Cross Check With Published $\sigma B(Z \rightarrow l^+ l^-)$	141
8.3	Discussion	142
A	Identification Efficiency Method	143

List of Figures

1.1	Feynman diagram for the Naive Parton Model.	2
1.2	Previous measurements of the Drell-Yan differential cross-section. .	3
1.3	Drell-Yan differential cross-section results from Run 0.	4
2.1	Feynman diagrams for corrections to the Naive Parton Model. . . .	9
2.2	Theoretical Drell-Yan cross-sections including corrections of $\mathcal{O}(\alpha_s)$ and $\mathcal{O}(\alpha_s^2)$, using the MRS-R2 structure function set.	12
2.3	k -factors for $\mathcal{O}(\alpha_s)$ and $\mathcal{O}(\alpha_s^2)$ corrections to the theoretical Drell-Yan cross-section, using the MRS-R2 structure function set.	13
2.4	Theoretical Drell-Yan cross-sections with different renormalization scales, using the MRS-R2 structure function set.	14
2.5	Theoretical Drell-Yan cross-sections with several different structure function sets.	15
3.1	Overview of the accelerator complex at Fermilab.	17
3.2	A perspective view of CDF.	19
3.3	A one quarter view of CDF.	20
3.4	The $\eta - \phi$ muon coverage for the central region of the CDF detector. .	25
4.1	Distributions of identification cut variables for electrons passing the tight cuts.	31
4.2	Distributions of identification cut variables for electrons passing the loose cuts.	32
4.3	Distributions of identification cut variables for muons passing the tight cuts.	36
4.4	Distributions of identification cut variables for muons passing the loose cuts.	37
4.5	Isolation and invariant mass distributions for dielectrons.	42
4.6	Isolation and invariant mass distributions for dielectrons.	43
5.1	Generated and accepted Monte Carlo simulated electron E_T distributions.	50
5.2	Generated and accepted Monte Carlo simulated electron E_T distributions.	51

5.3	Generated and accepted Monte Carlo simulated electron E_T distributions.	52
5.4	Generated and accepted Monte Carlo simulated electron η and ϕ distributions.	53
5.5	Comparison of data and Monte Carlo simulated electron η and ϕ distributions.	54
5.6	Comparison of data and Monte Carlo simulated electron ϕ distributions within calorimeter towers.	55
5.7	Generated and accepted Monte Carlo simulated muon p_T distributions.	57
5.8	Generated and accepted Monte Carlo simulated muon p_T distributions.	58
5.9	Generated and accepted Monte Carlo simulated muon p_T distributions.	59
5.10	Generated and accepted Monte Carlo simulated muon η and ϕ distributions.	60
5.11	Comparison of data and Monte Carlo simulated muon ϕ distributions.	61
5.12	Comparison of data and Monte Carlo simulated muon ϕ distributions.	62
5.13	Comparison of data and Monte Carlo simulated muon η distributions.	63
5.14	Comparison of data and Monte Carlo simulated muon ϕ distributions within calorimeter towers.	64
6.1	Electron trigger path.	68
6.2	Muon trigger path.	69
6.3	Level 1 electron trigger efficiency turn-on curve.	71
6.4	Level 2 electron trigger turn-on curves.	72
6.5	Level 3 electron trigger turn-on curve.	73
6.6	L1-L2-L3 combined electron trigger turn-on curves.	74
6.7	Level 1 muon trigger efficiency turn-on curve.	75
6.8	Level 2 muon trigger efficiency turn-on curves.	76
6.9	Level 2 muon trigger efficiency turn-on curves.	77
6.10	Level 3 muon trigger efficiency turn-on curve.	78
6.11	Monte Carlo simulated transverse momentum distributions for dielectrons.	87
6.12	Monte Carlo simulated transverse momentum distributions for dielectrons.	88
6.13	Monte Carlo simulated transverse momentum distributions for dimuons.	89
6.14	Monte Carlo simulated transverse momentum distributions for dimuons.	90
6.15	p_T distributions for data and Monte Carlo with minimized χ^2 and \pm “4 σ ” scaling values on the Monte Carlo p_T	96
6.16	p_T distributions for data and Monte Carlo with minimized χ^2 and \pm “4 σ ” scaling values on the Monte Carlo p_T	97
6.17	p_T distributions for data and Monte Carlo with minimized χ^2 and \pm “4 σ ” scaling values on the Monte Carlo p_T	98

6.18	p_T distributions for data and Monte Carlo with minimized χ^2 and \pm “4 σ ” scaling values on the Monte Carlo p_T	99
6.19	p_T distributions for data and Monte Carlo with minimized χ^2 and \pm “4 σ ” scaling values on the Monte Carlo p_T	100
6.20	p_T distributions for data and Monte Carlo with minimized χ^2 and \pm “4 σ ” scaling values on the Monte Carlo p_T	101
6.21	p_T distributions for data and Monte Carlo with minimized χ^2 and \pm “4 σ ” scaling values on the Monte Carlo p_T	102
6.22	p_T distributions for data and Monte Carlo with minimized χ^2 and \pm “4 σ ” scaling values on the Monte Carlo p_T	103
6.23	p_T distributions for data and Monte Carlo with minimized χ^2 and \pm “4 σ ” scaling values on the Monte Carlo p_T	104
6.24	p_T distributions for data and Monte Carlo with minimized χ^2 and \pm “4 σ ” scaling values on the Monte Carlo p_T	105
7.1	Rapidity distributions of cosmic and filtered events.	108
7.2	Hadron TDC timings for cosmic filter cut placement (2D).	110
7.3	Hadron TDC timings for cosmic filter cut placement (1D).	111
7.4	Differences in opening angles for cosmic filter cut placement.	112
7.5	Impact parameters for cosmic filter cut placement.	113
7.6	Hadron TDC timings versus dimuon η for cosmics and Z events.	114
7.7	Distribution of $\eta_{\mu 1} + \eta_{\mu 2}$ for cosmics and data.	116
7.8	Mass distributions of $\gamma^*/Z \rightarrow \tau^+\tau^-$ Monte Carlo events.	118
7.9	Mass distribution of $Z \rightarrow \tau^+\tau^-$ Monte Carlo events.	119
7.10	Mass distributions of accepted $Z \rightarrow \tau^+\tau^- \rightarrow l^+l^-$ Monte Carlo events.	120
7.11	Mass distributions of e^+e^- data and background.	122
7.12	Mass distributions of $\mu^+\mu^-$ data and background.	123
7.13	Mass distributions of isolated $e\mu$ events with the estimated $\tau\tau$ contribution subtracted.	125
8.1	Run 1B preliminary Drell-Yan plus Z cross-sections.	135
8.2	Run 1B preliminary Drell-Yan plus Z cross-sections.	136
8.3	Drell-Yan cross-sections scaled by M^3 in the 10-70 GeV/c ² range below the Z mass region.	138
8.4	Combined dielectron and dimuon Drell-Yan cross-sections scaled by M^3 in the 10-70 GeV/c ² range below the Z mass region.	139
8.5	Combined dielectron and dimuon Drell-Yan cross-sections scaled by M^3 in the 10-70 GeV/c ² range below the Z mass region.	140

List of Tables

3.1	Summary of the properties of the CDF calorimeter systems.	22
4.1	Offline Electron Identification Cuts	30
4.2	Electron Identification Efficiencies	33
4.3	Offline Muon Selection Cuts	38
4.4	Muon Identification Efficiencies	39
4.5	Dielectron isolation efficiencies for each mass bin.	45
6.1	Trigger efficiencies for each mass bin from the Monte Carlo.	80
6.2	Smearing/Radiation Matrices from Monte Carlo.	83
6.3	Normalized Smearing/Radiation Matrices from Monte Carlo.	84
6.4	Normalized and Inverted Smearing/Radiation Matrices from Monte Carlo.	85
6.5	Acceptance Data from Monte Carlo.	86
6.6	Scaling values for p_T scaling uncertainty estimate.	93
6.7	Systematic uncertainty of $A \times \varepsilon_{trig}$ from scaling the Monte Carlo lepton pair p_T	94
6.8	Systematic uncertainty of $A \times \varepsilon_{trig}$ from varying the Monte Carlo nucleon structure functions.	95
7.1	Estimate of $\tau\tau$ contribution to data samples.	121
7.2	Heavy Flavor Background from (os-ss) Isolation Distributions.	126
7.3	Table of estimated backgrounds to the Drell-Yan samples. The final column is the ratio of the total background to the same-sign subtracted number of events.	127
8.1	Values Used in the Cross-Section Calculation	130
8.2	Uncertainty Table for Dielectron Cross-Sections. The values represent the percent uncertainty for each contribution.	132
8.3	Uncertainty Table for Dimuon Cross-Sections. The values represent the percent uncertainty for each contribution.	133
8.4	Drell-Yan Differential Cross-Section Results.	134

ACKNOWLEDGEMENTS

I am indebted to both my advisor, Professor Jay Hauser, and Professor David Saltzberg for their help and support. Both have given me endless hours of instruction and assistance, and without them this work might never have been completed.

It has been my good fortune to collaborate with several outstanding researchers in the CDF collaboration. Professor Henry Frisch of the University of Chicago has offered a lot of assistance, and I am very grateful for his time. Thanks also to Todd Keaffaber for helping me *not* finish my thesis; meine deutschen Freunde Frank Hartmann, Andreas Heiss, Armin Köngeter, Dirk Neuberger, und Professor Thomas Müller; James Done for his SUSY dilepton sample and for help using it; Frank Chlebana, Rob Harris, Steve Nahn, Pierre Savard, and Steve Vejcik for help with my Run 2 computing responsibilities. Thanks to Yuri Bonushkin, Benn Tannenbaum, and Jane Nachtman and everyone else in the UCLA-CDF group at one time or another: Larry Dworkin, Allen Hui, David Goldstein, Matt Worcester. Thanks especially to Mike Lindgren without whom my time at Fermilab would not have been quite so fulfilling. Other people who have greatly enhanced my time at Fermilab include Max Chertok, Adam Hardman, and Arnold Pompos. And, of course, Roger Waters, David Gilmour, Nick Mason, and Richard Wright.

My wife, Jennifer, has been extremely supportive while I kept us in the poor house to finish graduate school. Jen, I could not have done this without you, and this is just another reason why I will always love you. Finally, I wish to thank my family, especially my mother, who has always believed that I could accomplish anything I dreamed *and more*.

VITA

March 12, 1973	Born in La Mesa, CA
1991-1995	Regents Scholar, University of California, Los Angeles
June 1995	Bachelor of Science, Physics, University of California, Los Angeles
1995-1996	Teaching Assistant, University of California, Los Angeles
December 1996	Master of Science, Physics, University of California, Los Angeles
1996-2000	Research Assistant, Department of Physics, University of California, Los Angeles

PUBLICATIONS AND PRESENTATIONS

- T. Armstrong, et al. "A Detector to Search for Anti-Proton Decay at the Fermilab Anti-Proton Accumulator", Nucl. Instrum. Meth., A411 (1998) pp. 210-222.
- Yu. Bonushkin, L. Dworkin, J. Hauser, C. Kim, M. Lindgren, A. Scott (UCLA), G. Appollinari (Rockefeller U.). "Tests of a third generation multianode phototube", Nucl. Instrum. Meth., A381 (1996) pp. 349-354.
- A. Scott, "A High Statistics Measurement of Low-Mass Drell-Yan Production at CDF". Paper presented at a meeting of the American Physical Society, Columbus, Ohio (April 1998).
- A. Scott, "A High Statistics Measurement of Low-Mass Drell-Yan Production at CDF". Paper presented at New Perspectives 1998 Conference, Fermi National Accelerator Laboratory (July 1998).

A. Scott, “A High Statistics Measurement of Low-Mass Drell-Yan Production at CDF”. Paper presented at the Centennial Meeting of the American Physical Society, Atlanta, Georgia (March 1999).

ABSTRACT OF THE DISSERTATION

**A Measurement of Low-Mass Drell-Yan Production at the Collider
Detector at Fermilab**

by

Andrew Ferrell Scott

Doctor of Philosophy in Physics

University of California, Los Angeles, 2000

Professor Jay Hauser, Chair

We present a measurement of low-mass lepton pair production in the central region of $p\bar{p}$ collisions with the Collider Detector at Fermilab at $\sqrt{s} = 1.8$ TeV. We study dileptons in the invariant mass range $11 < M_{ll} < 150$ GeV/ c^2 , within the rapidity range $|y| < 1$. The differential cross-sections, $M^3 d^2\sigma/dMdy$, are measured separately for electron and muon pairs, and the results are compared in order to investigate a possible difference between the electron and muon channels in the previous CDF result^[4]. This measurement has a much higher precision than the previous measurement due to increased luminosity: 85.37 pb⁻¹ (2651 events) in the electron channel and 83.68 pb⁻¹ (2062 events) in the muon channel.

Chapter 1

Introduction

1.1 The Drell-Yan Process

The lepton pair production mechanism known as “Drell-Yan” was first described by Sidney Drell and Tung-Mow Yan in 1970^[1]. The process had been experimentally observed in 1968 by a group at Brookhaven led by Leon Lederman, by colliding protons on a uranium target and observing the resulting muon pairs^[2]. It was confirmed in 1974 with electron pairs by Samuel C. C. Ting, also at Brookhaven.

A diagram of the leading-order Drell-Yan process is shown in Figure 1.1. In this leading-order process, a quark and an antiquark annihilate to produce a virtual photon, which then decays into two oppositely charged leptons. Since the final state is colorless (i.e. it does not interact strongly), the lepton pairs provide a unique view of the dynamics inside a proton. In higher-order models quark-quark and quark-gluon interactions produce the same final state. The initial state particles are collectively labelled “partons.” Measurements of Drell-Yan production have historically been good probes of the quark structure functions of the proton and

have played an important role in our understanding of Quantum Chromodynamics (QCD).

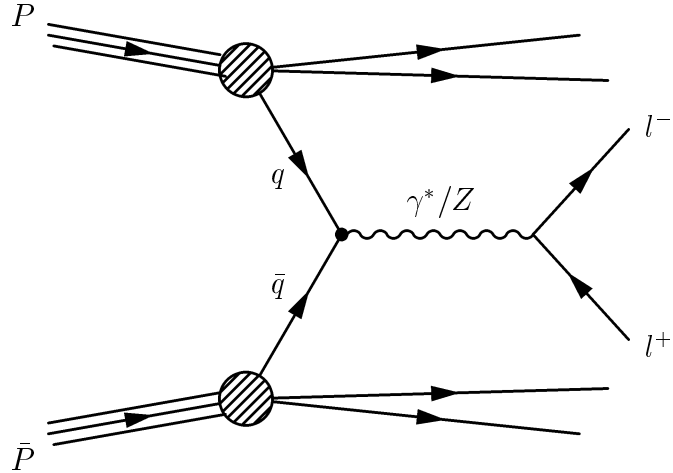


Figure 1.1: Feynman diagram for the Naive Parton Model.

1.2 Previous Measurements

A number of experiments have measured the Drell-Yan cross-section at various masses and with varying precision^[3]. However, most of these experiments have been limited by low interaction energies and low statistics, especially when compared to the high-energy/high-luminosity experiments at the Fermilab Tevatron. Figure 1.2 shows the results of three recent measurements of low mass Drell-Yan production cross-sections, $M^3 d^2\sigma/dM dy|_{|y|<1}$. The experimental results shown in Figure 1.2 include a 1992 result from UA2 with a center-of-mass energy of 630 GeV, and two results from Tevatron experiments (center-of-mass energy = 1800 GeV): a previous CDF result (Run 0) and a Run 1a dimuon result from D0.

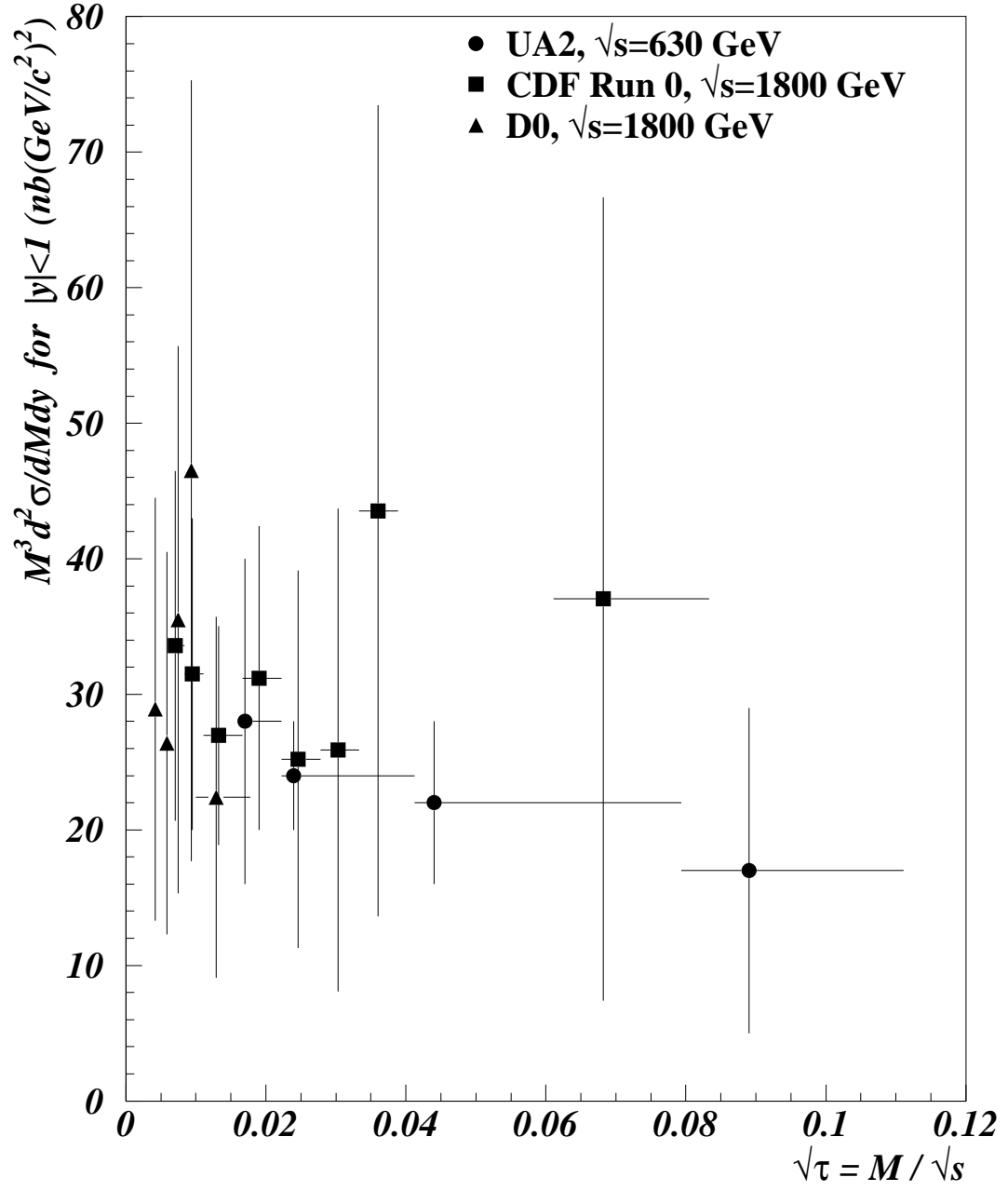


Figure 1.2: Previous measurements of the Drell-Yan differential cross-section. The scale invariant variable τ is explained in Chapter 2.

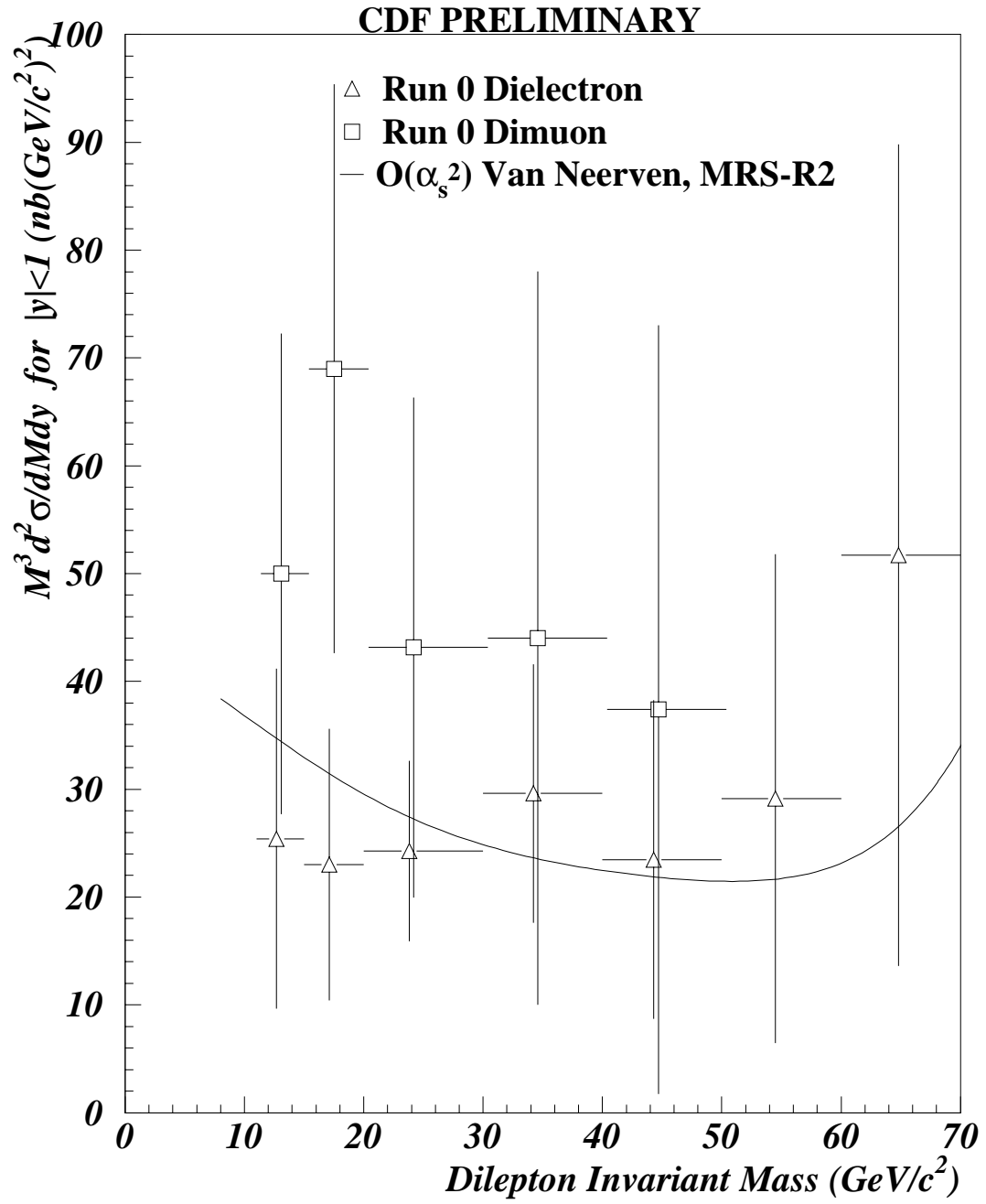


Figure 1.3: Drell-Yan differential cross-section results from Run 0.

The most recent CDF measurement of the low mass Drell-Yan differential cross-section has been from Run 0 (1988-1989)^[4]. The available dilepton data sets at that time were much smaller than what has been made available by Run 1B (1994-1995). For this reason, the published results were dominated by statistical uncertainties. The Run 0 CDF results were somewhat puzzling, because for every mass the dimuon cross-sections were consistently about a factor of two higher than the dielectron cross-sections (see Figure 1.3). However, the discrepancies were all within the published uncertainties, and no violation of Standard Model physics was claimed. The higher precision and increased detector acceptance in the larger Run 1B data set prompted us to investigate the possible discrepancy.

1.3 Analysis Strategy

This analysis focuses on improving upon the CDF Run 0 measurement with several strategies. First, this measurement has far greater statistical precision due to the fact that the Run 1b data set is more than 20 times larger than what was available in Run 0. Furthermore, less stringent and better understood cuts, such as the isolation cut described in Section 4.5.1, increase the sample size by another factor of two. Better muon coverage ($|\eta| < 1$ compared to $|\eta| < 0.6$ in Run 0) due to the inclusion of the CMX muon chambers further improves the dimuon statistics.

The heavy flavor background estimation is greatly improved by the increased statistics of Run 1b. The background contribution of $Z \rightarrow \tau^+\tau^-$ leptonic decays is also estimated, allowing us to understand a significant background that was not included in the Run 0 measurement.

Chapter 2

Theory

In this chapter I will discuss the theory of Drell-Yan production, including a derivation of the leading-order cross-section and some remarks about higher order corrections that result from quark-gluon interactions. In addition, some of the kinematic variables that are used in later chapters are defined.

2.1 The Naive Parton Model

The leading order contribution to Drell-Yan production is shown in Figure 1.1. This process consists of a quark-antiquark annihilation, producing a virtual photon, which then decays into a pair of oppositely-charged leptons.

The corresponding cross-section is

$$\hat{\sigma}[q\bar{q} \rightarrow l^+l^-] = \frac{4\pi\alpha^2}{9M^2}e_q^2 \quad (2.1)$$

where e_q is the charge of the quark and M is the invariant mass of the lepton pair.

The differential cross-section $d\hat{\sigma}$ is

$$d\hat{\sigma}[q\bar{q} \rightarrow l^+l^-] = G_q(x_a)dx_a G_{\bar{q}}(x_b)dx_b \hat{\sigma}[q\bar{q} \rightarrow l^+l^-] \quad (2.2)$$

where $G_q(x_a)$ is defined as the probability of finding a quark, q , with momentum $p_q = x_a P_p$, $G_{\bar{q}}(x_b)$ is defined as the probability of finding an antiquark, \bar{q} , with momentum $p_{\bar{q}} = x_b P_{\bar{p}}$, and P_p and $P_{\bar{p}}$ are the momenta of the proton and antiproton, respectively.

If we define

$$s = (P_p + P_{\bar{p}})^2 = (\text{center of mass energy})^2, \quad (2.3)$$

$$\hat{s} = (p_q + p_{\bar{q}})^2 = x_a x_b s, \quad (2.4)$$

$$\tau = M^2/s, \quad (2.5)$$

the virtual photon has $\hat{s} = M^2$, so $\tau = x_a x_b$. We can rewrite (2.2) as

$$\frac{d^2\sigma}{d\tau dx_L} = \frac{4\pi\alpha^2}{9M^2} \frac{1}{(x_a + x_b)} G_{q\bar{q}}(x_a, x_b) \quad (2.6)$$

where $x_L = x_a - x_b$ and

$$G_{q\bar{q}}(x_a, x_b) = \sum_{n_f} e_q^2 [G_q(x_a)G_{\bar{q}}(x_b) + G_{\bar{q}}(x_a)G_q(x_b)] \quad (2.7)$$

Then

$$\frac{d\sigma}{d\tau} = \int dx_L \frac{d^2\sigma}{d\tau dx_L} = \frac{4\pi\alpha^2}{9M^2} \int_{\tau}^1 \frac{dx_a}{x_a} G_{q\bar{q}}(x_a, \tau/x_a) \quad (2.8)$$

and finally

$$M^2 \frac{d\sigma}{d\tau} = F(\tau) \quad (2.9)$$

which can also be expressed

$$M^3 \frac{d\sigma}{dM} = F'(\tau) \quad (2.10)$$

The leading-order Drell-Yan differential cross-section depends only on $\tau = M^2/s$, not on M or \sqrt{s} individually. This *scaling* allows one to compare results from measurements at different interaction energies. (Note that the Z boson breaks this scaling.) Typically, differential cross-sections, $d\sigma/dM$, are presented scaled by M^3 , because all of the dynamics are in τ .

2.2 Higher-Order Contributions

Higher-order contributions to the Drell-Yan differential cross-section are the result of quark-gluon interactions which are not predicted by the Naive Parton Model. The most important higher-order processes are shown in Figure 2.1.

Contributions from higher-order processes are considerable, as revealed by Figure 2.2. The figure shows the theoretical predictions of the Naive Parton Model ($\mathcal{O}(\alpha_s^0)$) and higher-order corrections ($\mathcal{O}(\alpha_s^1)$ and $\mathcal{O}(\alpha_s^2)$) as calculated by Van Neerven *et al.*^[5] The scale by which the cross-section differs from the leading order calculation is referred to as the *k*-factor. As shown in Figure 2.3, the *k*-factor ranges from about 1.2 to 1.4 over the mass range ($8 < M_{ll} < 70$ GeV), indicating that the total correction to the leading-order cross-section is as high as 40%.

Figure 2.4 shows the theoretical Drell-Yan differential cross-section to $\mathcal{O}(\alpha_s^2)$ with the following QCD renormalization scales: $\mu_0^2 = m^2$, $m^2 + p_T^2$, $2m^2$, and $\frac{1}{2}m^2$.

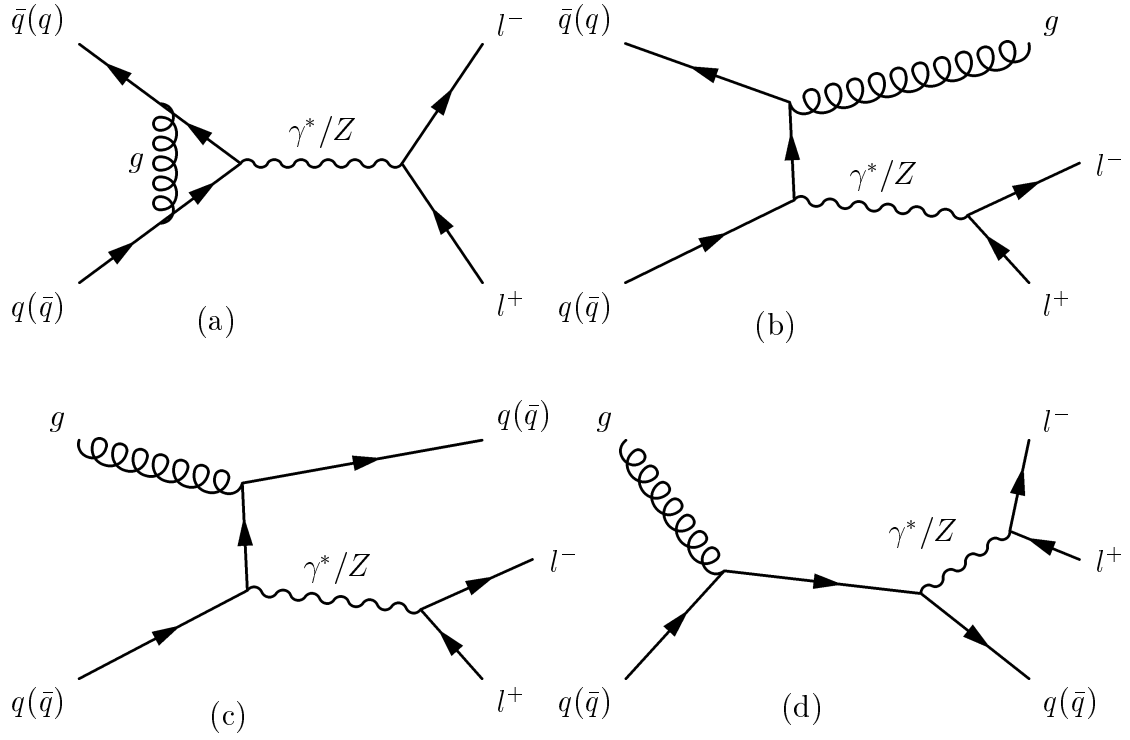


Figure 2.1: Feynman diagrams for corrections to the Naive Parton Model.

The predicted result is independent of the choice of renormalization scale except at the lowest masses. Figure 2.5 shows the predicted $\mathcal{O}(\alpha_s^2)$ cross section using the renormalization scale $\mu_0^2 = m^2 + p_T^2$ and the following structure function sets: GRV92, GRV98, MRSD0, MRS-R1, and MRS-R2.

2.3 Event Kinematics

Several kinematic variables are used in this analysis and are defined here:

Transverse momentum (p_T) is the component of the particle momentum which is transverse to the beamline. Forward scattered particles are generally propelled too close to the beamline to be observed in the CDF detector. Therefore, the total momentum of an event cannot be measured, and instead CDF measures the transverse momentum, $p_T = p \times \sin \theta$, of all interacting particles. p_T is measured in the Central Tracking Chamber (CTC).

Transverse energy (E_T) is analogous to the transverse momentum. Although energy is a scalar quantity, only the energy transverse to the beamline can be measured. E_T is the amount of energy measured in the CDF calorimeter, $E_T = E \times \sin \theta$.

Rapidity (y) is defined as

$$y \equiv \frac{1}{2} \ln \left(\frac{E + p_z}{E - p_z} \right)$$

where E is the energy of the particle and p_z is its momentum along the proton beam direction. Rapidity is generally used to represent the angular distribution of particles. The shape of the rapidity distribution is invariant under a

relativistic boost along the z -axis, so y is a better choice of variable than the polar angle θ .

Pseudorapidity (η) is approximately equal to rapidity in the limit where a particle's momentum is much greater than its mass. Pseudorapidity is defined as

$$\eta \equiv -\ln \tan\left(\frac{\theta}{2}\right)$$

where θ is the polar angle along the positive z -axis. The advantage of using pseudorapidity in place of rapidity is that the energy and momentum of the particle are not needed.

Track Isolation is the sum of the transverse momenta of tracks with $p_T > 0.4$ GeV (excluding the lepton) in a cone of radius $\Delta R = \sqrt{(\Delta\phi)^2 + (\Delta\eta)^2} = 0.4$ around a lepton track. Similarly, **Calorimeter Isolation** is the sum of calorimeter energy in a cone of radius $\Delta R = \sqrt{(\Delta\phi)^2 + (\Delta\eta)^2} = 0.4$ around the lepton energy cluster. Unless otherwise noted, when we refer to the isolation of a single lepton we mean the sum in quadrature of the calorimeter and track isolations of that lepton. When referring to the isolation of a pair of leptons we mean the maximum of the two lepton isolation variables.

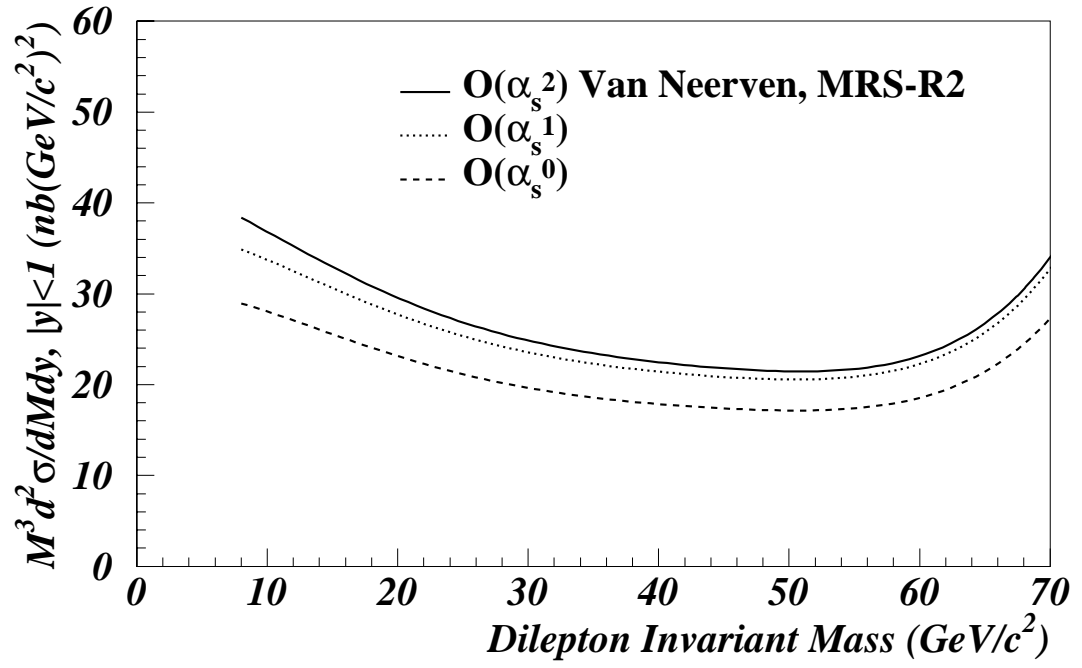


Figure 2.2: Theoretical Drell-Yan cross-sections including corrections of $\mathcal{O}(\alpha_s)$ and $\mathcal{O}(\alpha_s^2)$, using the MRS-R2 structure function set.

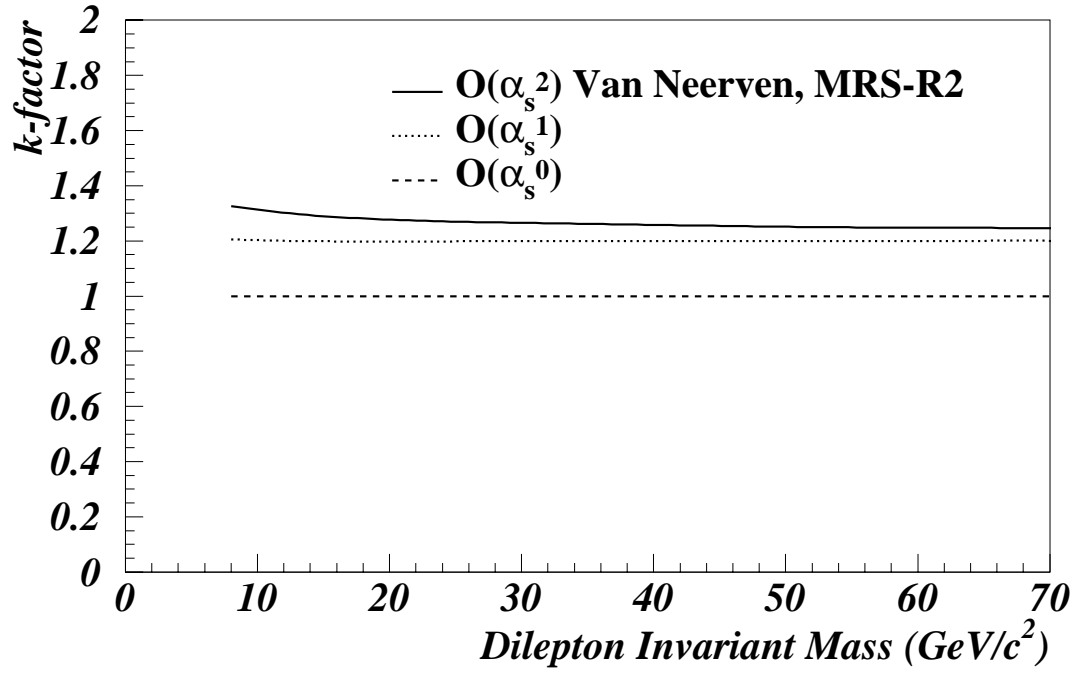


Figure 2.3: k -factors for $\mathcal{O}(\alpha_s)$ and $\mathcal{O}(\alpha_s^2)$ corrections to the theoretical Drell-Yan cross-section, using the MRS-R2 structure function set.

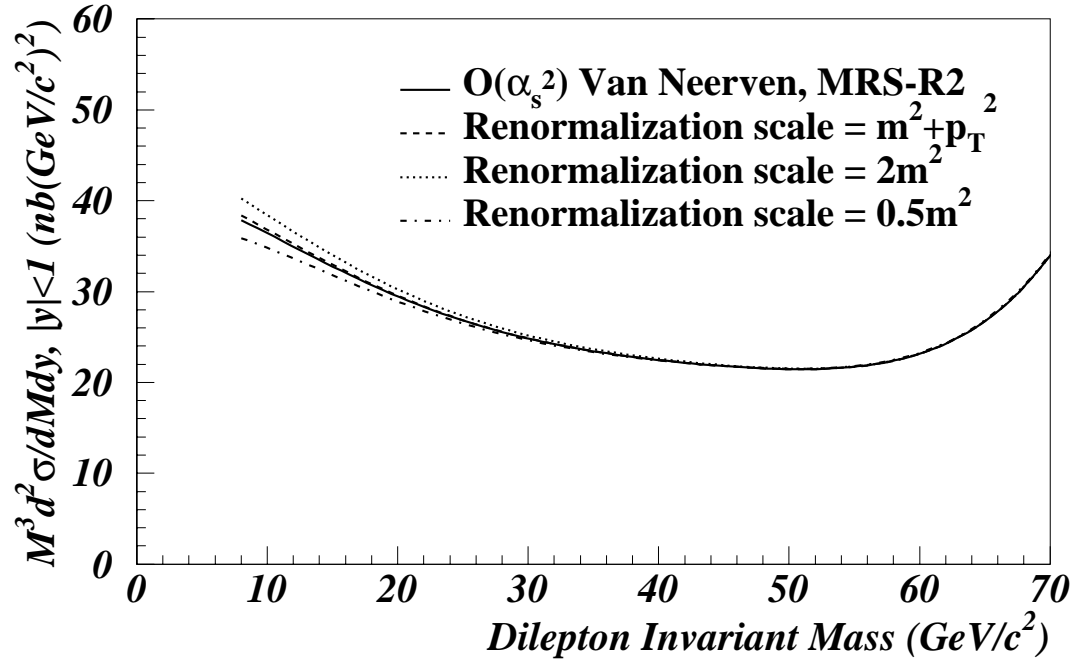


Figure 2.4: Theoretical Drell-Yan cross-sections with different renormalization scales, using the MRS-R2 structure function set. The solid curve represents the renormalization scale $\mu_0^2 = m^2$. Each curve includes $\mathcal{O}(\alpha_s^2)$ corrections.

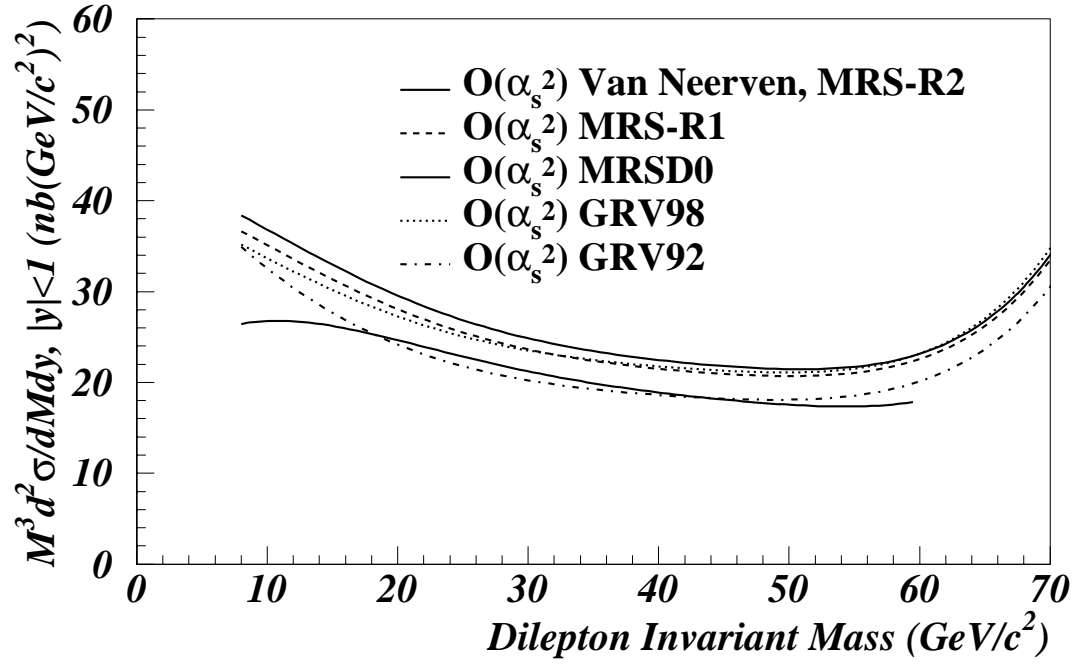


Figure 2.5: Theoretical Drell-Yan cross-sections with several different structure function sets. Each curve includes $\mathcal{O}(\alpha_s^2)$ corrections. The renormalization scale $\mu_0^2 = m^2 + p_T^2$ was used.

Chapter 3

Apparatus

The Fermilab Tevatron is used to accelerate protons and antiprotons to approximately $0.99944c$ and collide them at a center-of-mass energy of 1.8 trillion electron-volts (TeV). The collisions take place in the heart of the CDF detector, which consists of many components that are designed to identify particles and measure relevant quantities, such as energy and momentum. In this chapter I will discuss the apparatus involved in this analysis. A more detailed description can be found elsewhere^[6].

3.1 The Fermilab Tevatron

An overview of the particle acceleration process is shown in Figure 3.1. The process begins in a Cockcroft-Walton accelerator, which is essentially a large capacitor. Hydrogen gas is ionized by adding an electron to form H^- . The H^- ions are then accelerated by the Cockcroft-Walton in bunches of 1.4×10^{14} H^- ions, each with an energy of 750 keV.

The bunches of H^- ions enter the Linac, a linear accelerator which is 150 m

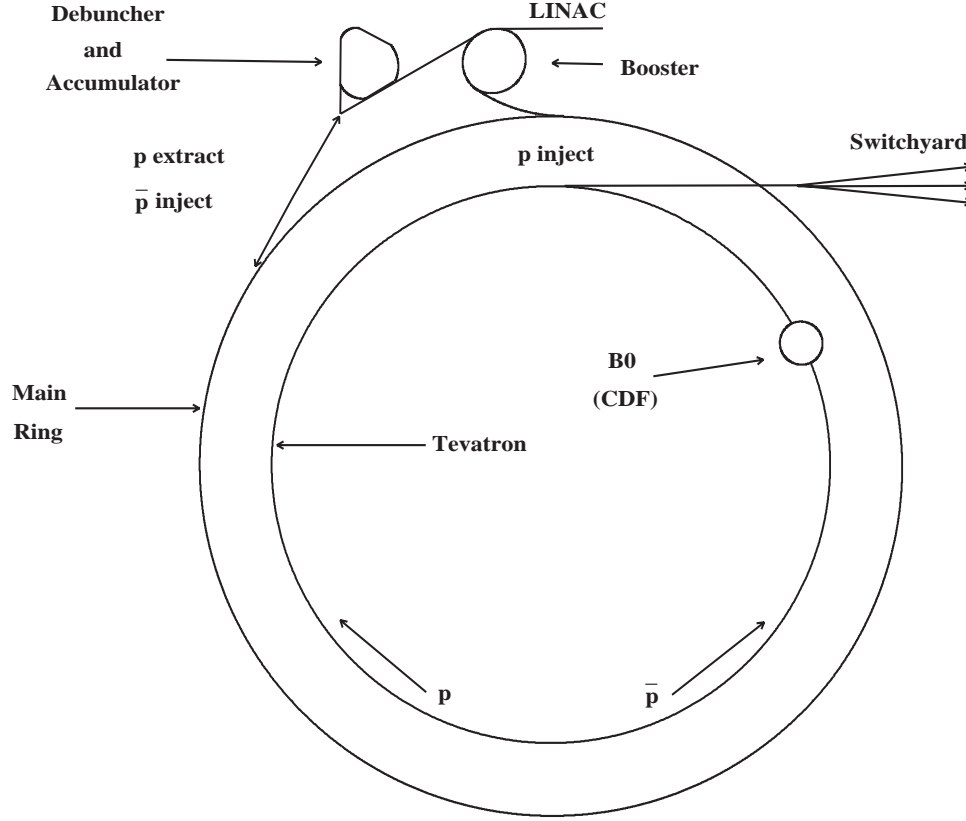


Figure 3.1: Overview of the accelerator complex at Fermilab.

long and consists of nine radio-frequency (RF) cavities of increasing length in the direction of acceleration. The Linac provides constant acceleration along its entire length, and at the end of the Linac the H^- ions exit with a kinetic energy of 400 MeV.

The H^- ions are stripped of both electrons by passing through a thin carbon foil before entering the Booster. The Booster is a rapid cycling synchrotron, which means that a single RF cavity is precisely controlled to provide continuous acceleration to the protons. The Booster is ring with radius 500 m, with conventional magnets to focus and steer the beam and the RF cavity that accelerates the protons.

Bunches of 10^{10} protons, each with 8 GeV of kinetic energy, are injected into the Main Ring.

The Main Ring is another rapid cycling synchrotron. It is a 1 km radius ring with 3.5 kGauss conventional dipole magnets for steering the beam, quadrupole magnets for focusing, and an RF cavity that accelerates the protons to 150 GeV before they are injected into the Tevatron. The Tevatron uses superconducting magnets with a very high magnitude magnetic field (4 Tesla), which allows the Tevatron to accelerate protons to 900 GeV.

Antiprotons are produced by colliding protons from the Main Ring on a tungsten target. About 20 antiprotons are produced per million protons collided. The antiprotons are selected using a magnetic field and are then sent to the Debuncher where stochastic cooling reduces the bunch size before the bunches are transferred to the Accumulator for storage. When enough antiprotons are collected they are re-injected into the Main Ring and then into the Tevatron where they reach an energy of 900 GeV, circulating in the direction opposite to that of the protons.

Bunches of protons and antiprotons are focused by quadrupole magnets so that they collide at an interaction point in the center of the CDF detector. A typical bunch of protons contains 2×10^{11} protons, while a typical bunch of antiprotons contains 6×10^{10} antiprotons. Bunch crossings occur every $3.5 \mu\text{s}$. The collision rate is measured by the luminosity, \mathcal{L} , of the Tevatron:

$$\mathcal{L} \equiv \frac{N_p N_{\bar{p}} N_B f_0}{4\pi\sigma^2}$$

where N_p is the number of protons per bunch, $N_{\bar{p}}$ is the number of antiprotons per bunch, N_B is the number of bunches, f_0 is the revolution frequency (~ 50 kHz), and

σ^2 is the transverse cross-sectional area of each bunch ($\sim 5 \times 10^{-5} \text{ cm}^2$). During Run 1B (August 1994 to December 1995) the typical instantaneous luminosity was $\mathcal{L} \approx 3 \times 10^{31} \text{ cm}^{-2}\text{s}^{-1}$, and the integrated luminosity was 87.7 pb^{-1} .

3.2 The Collider Detector at Fermilab

The Collider Detector at Fermilab (CDF) is 5000-ton multi-purpose detector, designed to identify many of the types of particles produced in high-energy $p\bar{p}$ collisions. It is cylindrical in shape with the axis of symmetry, the z -axis, pointing in the direction of the incoming proton beams. CDF uses a right-handed coordinate system, and the x and y axes point up and radially outward, respectively.

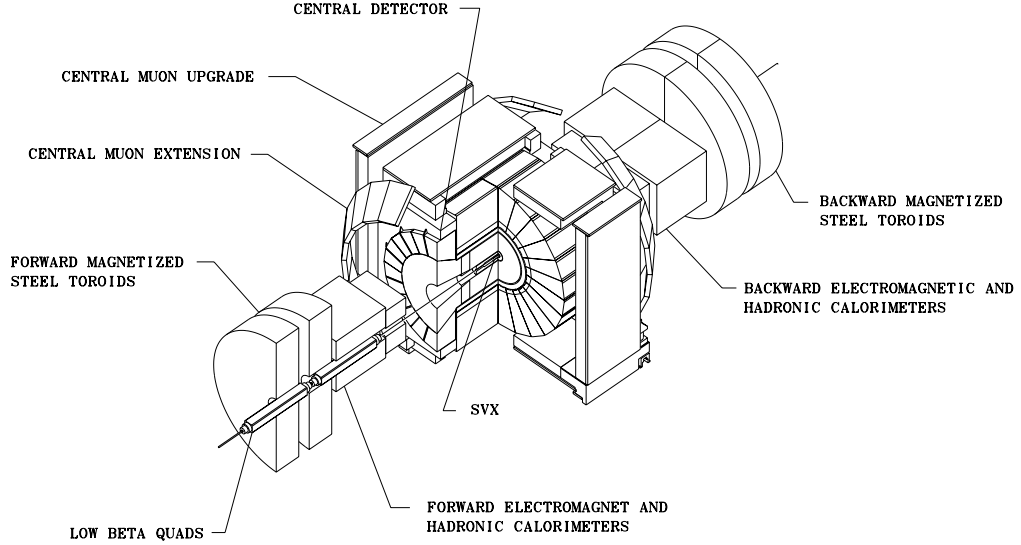


Figure 3.2: A perspective view of CDF. The entire detector is approximately 27 m long, 10 m high, and weighs 5000 tons.

Figure 3.2 shows a 3-dimensional perspective of the detector with one quadrant cut away to reveal the detector components inside. Figure 3.3 shows a side view of

one quadrant of the detector. From the interaction region outward, the electrons and muons in this analysis pass through the VTX chamber where the event vertex is measured, the CTC which measures the lepton trajectory to obtain its momentum, CEM and CHA calorimeters that measure deposited energies, and in the case of a muon, into the central muon chambers (CMU/CMP/CMX) which identify muons. These detectors are described in detail in the following sections.

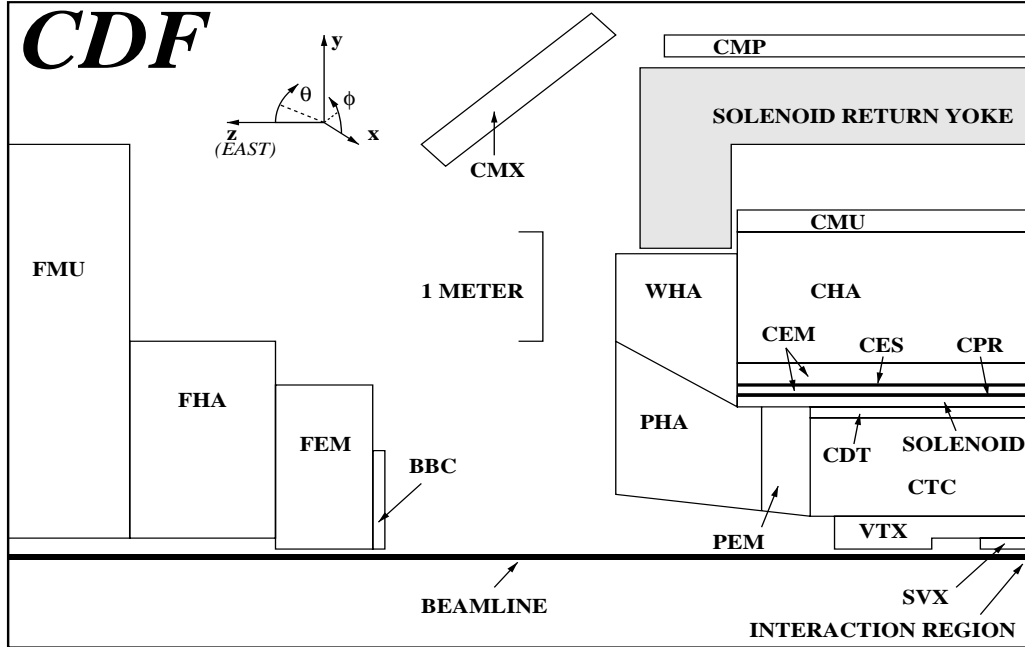


Figure 3.3: A one quarter view of CDF. The nominal interaction region is located in the bottom right-hand corner along the beamline. The coordinate system which CDF uses is shown inset in the upper left of the diagram.

3.2.1 Vertex Time Projection Chamber (VTX)

The Vertex Time Projection Chamber (VTX) is used to reconstruct the event vertex position. This is important for lepton track reconstruction and for measurements of the transverse energy (E_T). The VTX extends 1.4 m from either side of

the nominal interaction region. It surrounds the SVX detector and has an inner radius of 7 cm and an outer radius of 22 cm.

The VTX consists of 8 octagonal chambers placed along the beamline. The chambers use 50/50 argon-ethane gas and a high voltage grid with a 320 V/cm longitudinal electric field which divides the chamber into two oppositely directed drift regions. The drift direction is along the z -axis with a drift velocity of $46 \mu\text{m/ns}$ and a maximum drift distance of 15.25 cm. The maximum drift time is less than the $3.5 \mu\text{s}$ timing between $p\bar{p}$ bunch crossings. Ionization electrons drift to the endcaps of each chamber, where 24 sense wires in each octant measure the position of the hit. The resolution of the z vertex measurement is 2 mm.

3.2.2 Central Tracking Chamber (CTC)

The Central Tracking Chamber (CTC) lies just outside the VTX and inside the 1.4 Tesla solenoidal magnet. It is a cylindrically symmetric open-wire drift chamber that provides tracking out to $|\eta_{\text{detector}}| \sim 1$. The CTC is 3.2 m long and has radial coverage $28 < r < 138$ cm. Wires are strung along the z -direction between endplates at $z = \pm 1.6$ m.

There are 84 layers of sense wires in 9 “superlayers” - 5 axial and 4 stereo - in an argon-ethane-ethanol gas mixture (49.6/49.6/0.8%). The axial superlayers are composed of 12 radially separated layers of sense wires that run parallel to the z -axis and provide $r - \phi$ hit information. The stereo superlayers are composed of 6 sense wires per layer, rotated by 3 degrees from the z -axis. Axial and stereo hit information is combined to reconstruct 3-dimensional tracks.

Charged particles that pass through the 1.4 Tesla magnetic field of the solenoid follow a helical trajectory of which the curvature determines the momentum of the

Table 3.1: The properties of the CDF calorimeter systems.

System	η Coverage	Energy Resolution	Thickness
CEM	$ \eta < 1.1$	$13.7\%/\sqrt{E_T} \oplus 2\%$	$18 X_0$
CHA	$ \eta < 0.9$	$50\%/\sqrt{E_T} \oplus 3\%$	$4.5 \lambda_0$
WHA	$0.7 < \eta < 1.3$	$75\%/\sqrt{E_T} \oplus 4\%$	$4.5 \lambda_0$

particle. The momentum resolution of a beam constrained track in the CTC is $\delta p_T/p_T = 0.001 \times p_T/\text{GeV}$.

3.2.3 Calorimetry

CDF has four different calorimeter systems: central, wall, plug, and forward. The central, plug, and forward systems have both electromagnetic and hadronic calorimeters, and all systems use projective tower geometry with towers that cover specific constant ranges in η and point back to the nominal interaction region. All particles in this analysis are required to be within the central region of the CDF detector. Therefore, we are concerned only with the central electromagnetic (CEM) and central hadronic (CHA) and wall hadronic (WHA) calorimeters. Table 3.1 summarizes these detectors.

Central EM Calorimeter

The Central Electromagnetic calorimeter (CEM) covers the η region $|\eta| \leq 1.1$ and is split into two equal halves covering positive $\eta_{detector}$ (east) and negative $\eta_{detector}$ (west). Each half is divided into 24 wedges, and each wedge covers 15° in ϕ and 0.1 in η . Where the east and west calorimeters meet there is a dead area between them approximately 8 cm wide, which is known as the 90° crack.

Each CEM wedge consists of 31 layers of 5mm thick plastic scintillator inter-

leaved with 30 layers of $\frac{1}{8}$ inch lead absorber sheets. Light guides collect the light from the scintillator and direct it to photomultiplier tubes. There are two photomultipliers per tower. The pulse height is proportional to the amount of energy deposited by an electromagnetic shower.

The CEM is about 18 interaction lengths thick. A single radiation length is the distance in which a high energy electron loses all but $1/e$ of its energy. In each wedge, a proportional strip chamber, the CES, is inserted between the eighth layer of lead and the ninth scintillator layer. This corresponds to six radiation lengths, which is where the electromagnetic shower is expected to deposit its maximum energy. The CES gives position information about the shower: both z and $r - \phi$ positions with a resolution in each view of ± 2 mm.

Central and Wall Hadronic Calorimeters (CHA and WHA)

The Central and Wall Hadronic Calorimeters (CHA and WHA) are located outside the CEM and are very similar in structure to the CEM. The same tower structure is used, but steel is used as the absorber material in place of lead. The CHA covers the region $0.0 < |\eta| < 0.9$ and has 32 layers of 2.5 cm thick steel absorber sandwiched with layers of 1 cm thick plastic scintillator. It is about 4.7 interaction lengths thick. The WHA shares coverage with the CHA in the region $0.7 < |\eta| < 0.9$ and additionally covers $0.9 < |\eta| < 1.3$. It has 15 layers of 5.1 cm thick steel sandwiched with 1 cm thick plastic scintillator and totals about 4.5 interaction lengths.

Phototubes read out the scintillator light pulses from the hadronic calorimeters. The pulses are amplified which also triggers a discriminator pulse. The Hadron TDCs (HTDC) measure the time elapsed between this discriminator pulse and a

common stop signal. The TDCs have a range of 700 ns and resolution of 0.5 ns. The HTDCs are used to reject cosmic ray muons (see Section 7.1).

3.2.4 Central Muon Chambers

The CMU is outside the CHA and consists of 4 layers of drift chambers covering the region $|\eta| < 0.6$. Only muons and a small number of punch-throughs from energetic jets can survive the large number of interaction lengths between the nominal interaction region and the CMU. Muons must have $p_T > 1.4$ GeV to reach the CMU.

The Central Muon Upgrade (CMP) is another set of 4 drift chambers that are outside the CMU. Between the CMU and CMP is an additional 60 cm of steel absorber (8 interaction lengths), which helps reduce the rate of fake muons from punch-throughs.

The Central Muon Extension (CMX) consists of four-standing conical arches and covers the region $0.6 < |\eta| < 1.0$. The arches contain drift chambers, to detect muons, between scintillators that are used for triggering. The CMX has a 90° gap at the bottom of the detector where it intersects the floor and a 30° gap at the top of the detector where the Main Ring and solenoid refrigerator are located.

Figure 3.4 shows the $\eta - \phi$ coverage of the CMU, CMP, and CMX chambers.

3.2.5 Trigger

CDF uses a three level trigger system to determine whether an event should be written to tape. Each successive level of trigger is more sophisticated and requires more time to reach a decision. The CDF trigger system is described below. A more detailed discussion of triggers used in this analysis is given in Section 6.1.

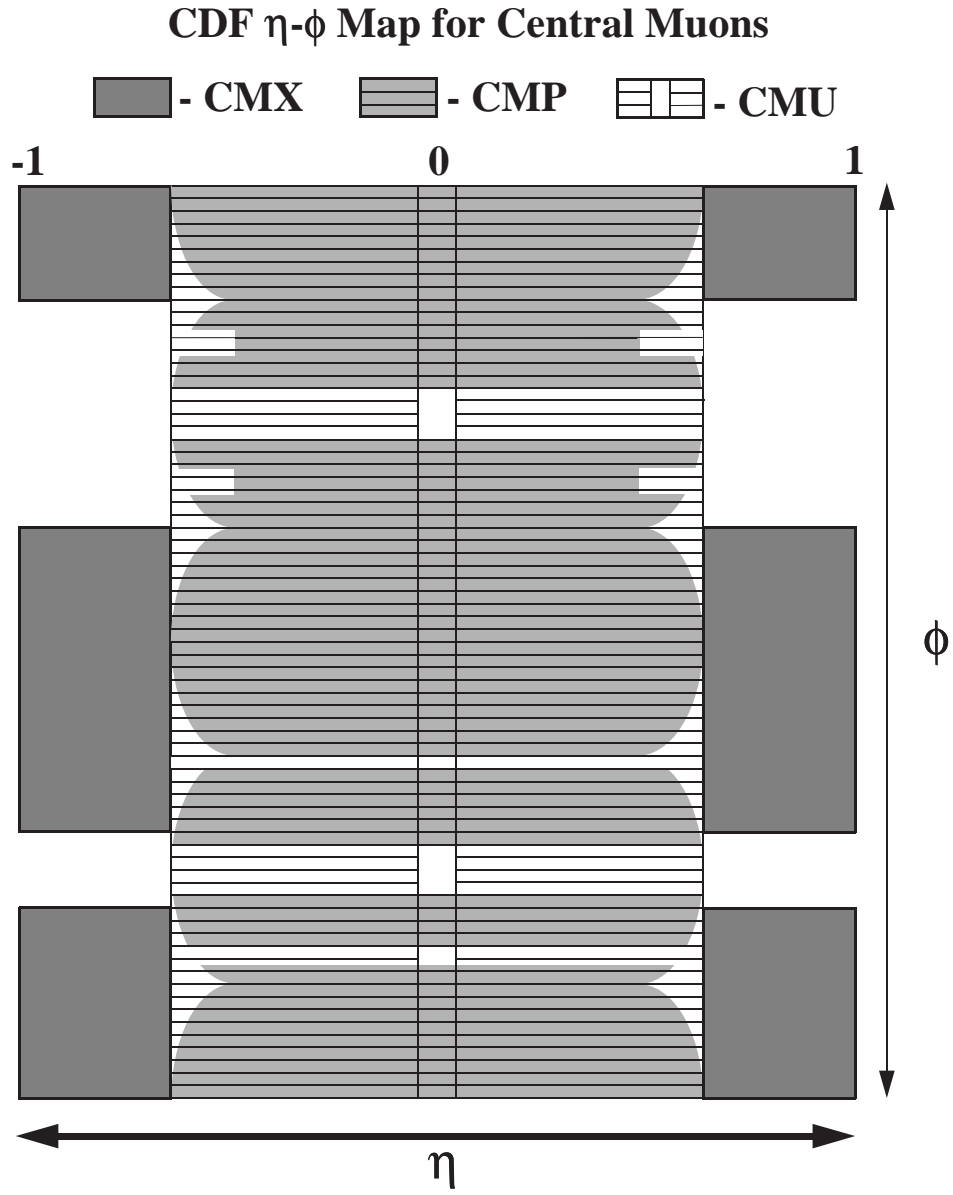


Figure 3.4: The $\eta - \phi$ muon coverage for the central region of the CDF detector.

The Level 1 trigger is composed of fast electronics that process the output of several individual subsystems to determine if some basic requirement is met (for instance, a certain amount of electromagnetic energy or hits in the muon chambers). The Level 1 trigger must decide whether to pass the event to the next trigger level before the next bunch crossing occurs (every $3.5 \mu\text{s}$). In Run 1B the Level 1 trigger rate was approximately 1 kHz.

The Level 2 trigger takes approximately $20 \mu\text{s}$ to make a decision. During this time ~ 6 bunch crossings are ignored by the detector. Level 2 is a hardware trigger like Level 1, but it combines requirements from different subsystems. Calorimeter data is used to find clusters, and fast timing signals from the CTC are used in conjunction with a hardware track processor – the Central Fast Tracker (CFT) – to find simple 2-dimensional tracks. A look-up table gives the particle momentum with a resolution of $\delta p_T \approx 0.035 \times p_T$. A typical electron Level 2 trigger might require both a CEM cluster with E_T above some threshold *and* a CFT track with some minimum p_T . Muon Level 2 triggers require CFT tracks that are matched to hits in the muon chambers.

Some types of events occur so often that a Level 2 trigger must be “prescaled” to accept one of every N events that would have normally passed that trigger. This allows events that occur less often, but that may be just as interesting, to be recorded to tape. Prescaling can be either static (fixed for an entire data taking run) or dynamic (changed during the course of the run depending on the instantaneous luminosity).

Events which pass the Level 2 trigger system are processed in more detail at Level 3. The Level 3 trigger is a software trigger that uses a farm of Silicon Graphics processors to reconstruct and examine the full event. The CFT and hardware

calorimeter cluster data are dropped in favor of the full CTC tracking code and of-line calorimeter clustering routines. Events passing the Level 3 trigger were written to tape at a rate of ~ 10 Hz.

Chapter 4

Event Selection

In order to obtain a sample of events consistent with Drell-Yan production, a number of cuts were applied to events in the Run 1B data sets. We required at least two leptons in each event, one which passed a tight set of cuts and another which passed a loose set of cuts. The identification efficiencies were measured using very low-background $Z \rightarrow l^+l^-$ events.

4.1 Electron Identification

Electrons were selected from the dilepton sample (see Section 4.3) using the following cuts, which are also summarized in Table 4.1.

Transverse energy and momentum are defined in Section 2.3. The tight cut electron must have $E_T > 8$ GeV and $p_T > 6$ GeV, and the loose cut electron must have $E_T > 5$ GeV and $p_T > 2.8$ GeV. The efficiency of these cuts is considered as part of the kinematic acceptance and will be discussed in Section 6.2.

E/p is the ratio of the energy of an electron to its momentum. Electrons for which E/p is greater than 2.0 are removed. This ensures that an electron track is correctly associated with the energy cluster in the calorimeter.

Had/EM is the ratio of energy deposited in the hadronic calorimeter to the energy deposited in the electromagnetic calorimeter. This cut reduces the amount of hadronic background. Tight electrons must have $\text{Had/EM} \leq 0.05$. Loose electrons must pass a sliding cut ($\text{Had/EM} \leq 0.055 + 0.045 \times \frac{E}{100}$), which includes an energy dependent term to correct for the electromagnetic energy leakage into the hadronic calorimeter.

LSHR is the lateral shower profile of the electron shower. It is defined as

$$LSHR \equiv 0.14 \sum_i \frac{E_i^{adj} - E_i^{prob}}{\sqrt{(0.14\sqrt{E})^2 + (\Delta E_i^{prob})^2}}$$

where E_i^{adj} is the energy measured in a tower adjacent to the seed tower of the electron, E_i^{prob} is the energy expected in the adjacent tower based on test beam data, and the errors on the measured and expected energies are $0.14\sqrt{E}$ and ΔE_i^{prob} respectively. LSHR must be less than 0.2.

$|\Delta x|$ and $|\Delta z|$ are track-shower matching cuts. The electron track is extrapolated to the position of the CES chamber, and the extrapolated position is compared to the shower position measured in the CES. Δx is the $r - \phi$ separation, and it is required to be less than 3 cm. $|\Delta z|$ is the separation in the z direction, and it is required to be less than 5 cm.

χ_{strip}^2 is the result of a comparison of the electron's CES pulse height to test beam data. The comparison is made for each of the 11 z-strips in the CES chamber.

The tight cut electron must have $\chi_{strip}^2 < 10$, while the loose cut electron is required to have $\chi_{strip}^2 < 15$.

Track quality cuts require 3 axial and 2 stereo superlayers in the CTC.

Figures 4.1 and 4.2 show distributions for each identification cut variable. The first figure shows the tight cut CEM electron distributions, while the latter shows the same for the loose CEM electron.

Table 4.1: Offline Electron Identification Cuts

Cut	Tight CEM	Loose CEM
P_T	$> 6 \text{ GeV}/c$	$> 2.8 \text{ GeV}/c$
E_T	$> 8 \text{ GeV}$	$> 5 \text{ GeV}$
E/P	< 2.0	< 2.0
HAD/EM	< 0.05	$< 0.055 + 0.045 \times E/100$
LSHR	< 0.2	< 0.2
$ \Delta x $	$< 3 \text{ cm}$	$< 3 \text{ cm}$
$ \Delta z $	$< 5 \text{ cm}$	$< 5 \text{ cm}$
χ_{strip}^2	< 10	< 15

4.1.1 Electron Identification Efficiency

Electron identification efficiencies were measured using unbiased electrons from a high E_T ($E_T > 20 \text{ GeV}$) inclusive electron sample. A smaller sample of Z events ($86 < M_{ee} < 96 \text{ GeV}$) was selected by requiring one electron with tighter cuts than those in Table 4.1 and a second ELES electron which was only required to be isolated (calorimeter Iso $< 4 \text{ GeV}$) and have a E_T greater than 20 GeV. The cuts on the tight electron were: $E/p < 1.5$, Had/EM < 0.04 , LSHR < 0.1 , $|\Delta x| < 1.5 \text{ cm}$, and $|\Delta z| < 2.0 \text{ cm}$.

Tight CEM Electron

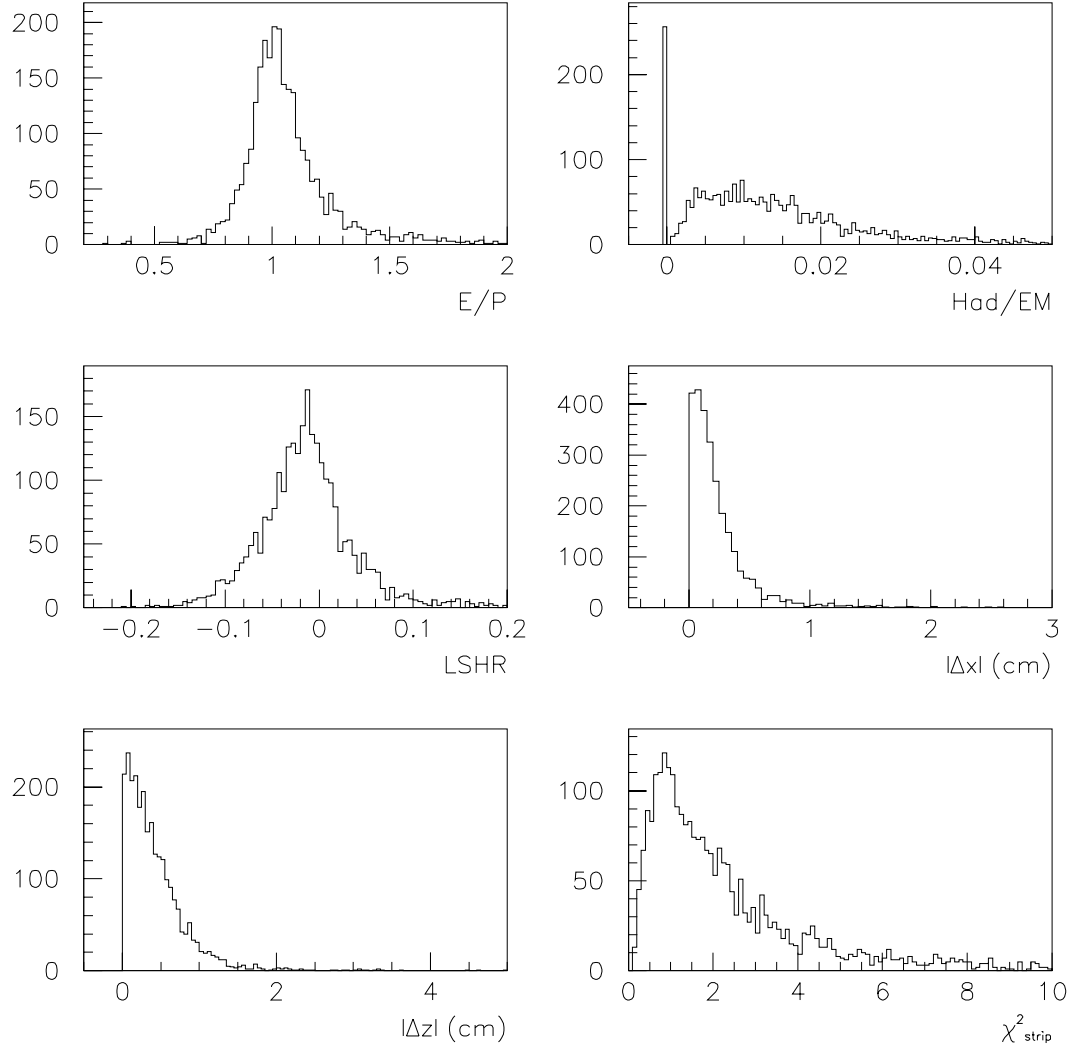


Figure 4.1: Distributions of identification cut variables for electrons passing the tight cuts.

Loose CEM Electron

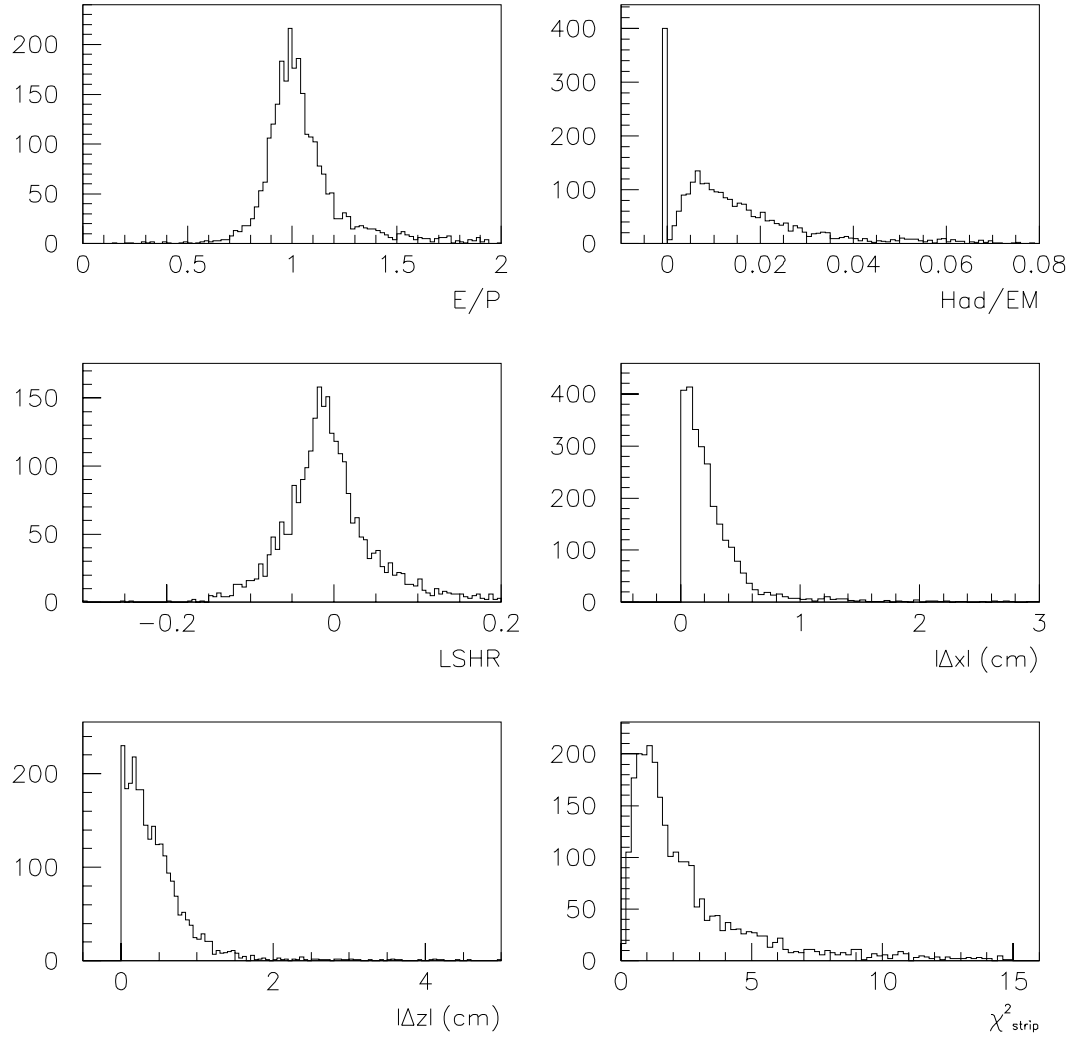


Figure 4.2: Distributions of identification cut variables for electrons passing the loose cuts.

Equation 4.1 was used to calculate the efficiency of each of the electron identification cuts.

$$\varepsilon_C = \frac{N_C + N_{TT}}{N_{tot} + N_{TT}} \pm \sqrt{\frac{(N_C + N_{TT})(N_{tot} - N_C)}{(N_{tot} + N_{TT})^3}} \quad (4.1)$$

where N_{tot} is the total number of Z events selected from the inclusive electron sample, N_{TT} is the subset of those for which both electrons passed the “tighter” cuts listed above, and N_C is the subset of N_{tot} for which the second leg passed the cut or set of cuts considered. A derivation of Equation 4.1 is provided in Appendix A.

The number of selected Z events, N_{tot} , was 1912, and the number of “tight-tight” events, N_{TT} , was 1193. The number of events passing a given cut, N_C , depended on the cut and varied from 1797 for the tight χ^2_{strip} cut (an efficiency of $96.3 \pm 0.3\%$) to 1912 for the track quality requirement (an efficiency of 100%). Table 4.2 lists all of the electron identification efficiencies for both tight and loose cuts. The table also lists the total electron identification efficiency (tight: $85.0 \pm 0.6\%$, loose: $88.7 \pm 0.6\%$), which was calculated using all of the cuts at once, where N_C was 1446 for the tight cuts and 1561 for the loose cuts.

Table 4.2: Electron Identification Efficiencies

Cut	Tight	Loose
E/P	$92.5 \pm 0.5\%$	$92.5 \pm 0.5\%$
HAD/EM	$96.3 \pm 0.3\%$	$99.0 \pm 0.2\%$
LSHR	$98.5 \pm 0.2\%$	$98.5 \pm 0.2\%$
$ \Delta x $	$97.9 \pm 0.3\%$	$97.9 \pm 0.3\%$
$ \Delta z $	$99.2 \pm 0.2\%$	$99.2 \pm 0.2\%$
$\chi^2(\text{strip})$	$96.3 \pm 0.3\%$	$97.8 \pm 0.3\%$
Track quality	$100.0 \pm 0.0\%$	$100.0 \pm 0.0\%$
All Cuts	$85.0 \pm 0.6\%$	$88.7 \pm 0.6\%$

The identification efficiencies are consistent with what has been measured for

$J/\psi \rightarrow e^+e^-$ events with similar electron identification cuts^[14]. There is therefore no evidence for an E_T dependence on the electron identification efficiencies.

The electron identification efficiencies were measured relative to the efficiency for an electron making an ELES bank. The ELES efficiency is known to be $99.56 \pm 0.12\%$ per electron^[13].

4.2 Muon Identification

Muons were selected from the dilepton sample (see Section 4.3) using the following cuts, which are also summarized in Table 4.3.

Transverse momentum is defined in Section 2.3. The tight cut muon must have

$p_T > 8$ GeV, and the loose cut muon must have $p_T > 4$ GeV. The efficiency of these cuts is considered as part of the kinematic acceptance and will be discussed in Section 6.2.

EM is the amount of energy the muon deposits in the electromagnetic calorimeter (CEM). High p_T muons should not stop in the EM calorimeter, so muons with $\text{EM} > 2.0$ GeV are cut.

Had is the amount of energy the muon deposits in the hadronic calorimeter. Muons with $\text{Had} > 6.0$ GeV are cut.

Had+EM is the sum of the energies measured in the electromagnetic and hadronic calorimeters. Muons are cut if Had+EM is not greater than 0.1 GeV.

d_0 raw is the uncorrected impact parameter of the muon. The tight cut CMU/CMP muon must have $d_0 \leq 0.5$ cm, while the loose cut CMU/CMP/CMX muon must have $d_0 \leq 0.8$ cm.

d_0 beam is the impact parameter corrected for the beam position. This number should be very small in comparison to the uncorrected impact parameter, and the cuts are placed at 0.2 cm (tight CMU/CMP), and 0.5 cm (loose CMU/CMP/CMX).

Matching refers to a number of cuts which ensure good matching between the muon track and its corresponding stub in the muon chamber. $|\Delta X|$ of the muon is the distance between the extrapolation of the muon track into the muon chamber and the muon stub position. χ_x^2 refers to the quality of the fit between the track and the stub. Any one of the following must be true for tight cut muons: CMU $|\Delta X| < 2.0$ cm OR CMU $\chi_x^2 < 9.0$ OR CMP $|\Delta X| < 5.0$ cm OR CMP $\chi_x^2 < 9.0$. For loose cut muons the CMU and CMP requirements are the same, and the CMX matching cuts are $|\Delta X| < 5.0$ cm OR $\chi_x^2 < 9.0$.

Track quality cuts require 3 axial and 2 stereo superlayers in the CTC.

Figures 4.3 and 4.4 show distributions for each identification cut variable. The first figure shows the tight cut muon distributions, while the latter shows the same for the loose muon.

4.2.1 Muon Identification Efficiency

The CMU/CMP muon identification efficiencies were measured using the same method that was described for the electrons in Section 4.1.1. The efficiencies were calculated using Equation 4.1. Muon pairs were selected if both muons had p_T greater than 20 GeV and if the invariant mass of the pair was in the Z mass window ($86 < M_{\mu\mu} < 96$ GeV). The “tighter” muon cuts were: EM < 1.5 GeV, Had $<$

Tight CMU/CMP Muon

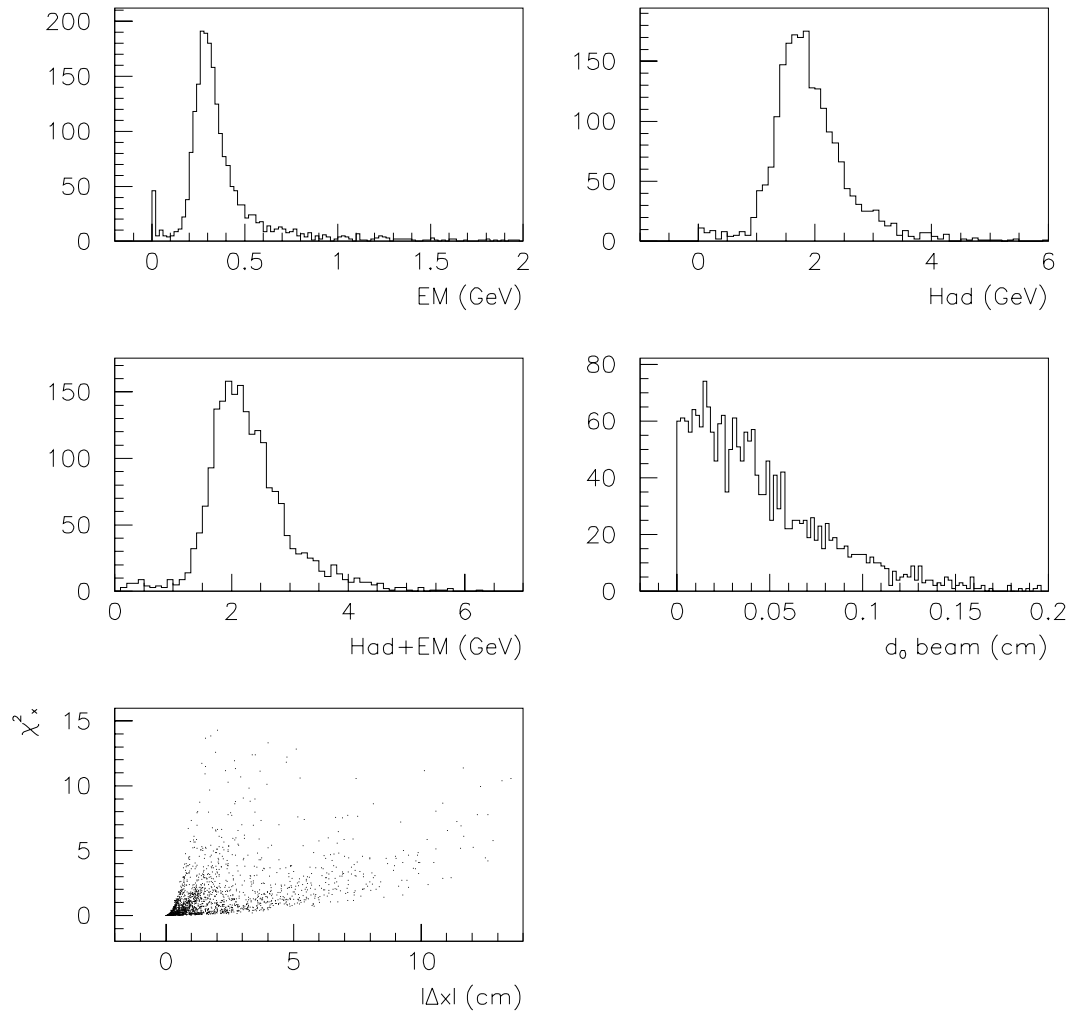


Figure 4.3: Distributions of identification cut variables for muons passing the tight cuts.

Loose CMU/CMP/CMX Muon

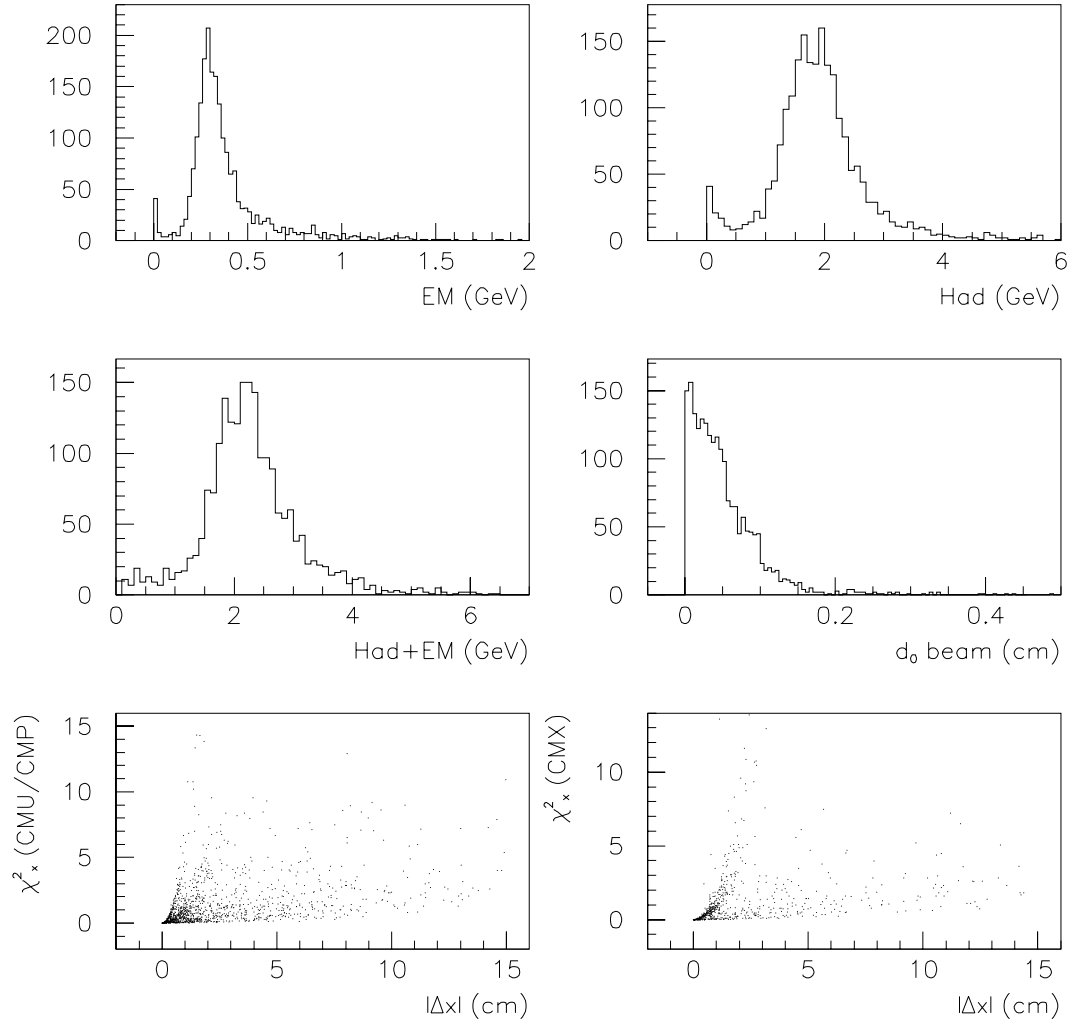


Figure 4.4: Distributions of identification cut variables for muons passing the loose cuts.

Table 4.3: Offline Muon Selection Cuts

Cut	Tight CMU/CMP	Loose CMU/CMP/CMX
P_T	$> 8 \text{ GeV}/c$	$> 4 \text{ GeV}/c$
$E(\text{EM Tower})$	$< 2 \text{ GeV}$	$< 2 \text{ GeV}$
$E(\text{HAD Tower})$	$< 6 \text{ GeV}$	$< 6 \text{ GeV}$
HAD+EM	$> 0.1 \text{ GeV}$	$> 0.1 \text{ GeV}$
$d_0 \text{ raw}$	$< 0.5 \text{ cm}$	$< 0.8 \text{ cm}$
$d_0 \text{ beam}$	$< 0.2 \text{ cm}$	$< 0.5 \text{ cm}$
CMU $ \Delta x $ or χ_x^2	$< 2 \text{ cm}$ or < 9	$< 2 \text{ cm}$ or < 9
CMP $ \Delta x $ or χ_x^2	$< 5 \text{ cm}$ or < 9	$< 5 \text{ cm}$ or < 9
CMX $ \Delta x $ or χ_x^2	N/A	$< 5 \text{ cm}$ or < 9

4 GeV, EM+Had $> 0.1 \text{ GeV}$, $d_0 \text{ raw} < 0.5 \text{ cm}$, $d_0 \text{ beam} < 0.2 \text{ cm}$, CMU (CMP) $|\Delta X| < 1.5(3.0) \text{ cm}$, and $\chi_x^2 < 6.0$. The second (unbiased) muon was required to be isolated (calorimeter Iso $< 4 \text{ GeV}$).

Of the 702 Z events that were selected (N_{tot}), 566 were “tight-tight” muon pairs (N_{TT}). The number of events which passed all of the tight muon identification cuts was 617 ($\varepsilon_{ID}^{tight} = 93.3 \pm 0.7\%$), and the number of events which passed all of the loose muon identification cuts was 629 ($\varepsilon_{ID}^{loose} = 94.2 \pm 0.7\%$).

The CMX muon identification efficiencies were determined by requiring a tight cut CMU/CMP muon which passed the tight cuts listed above, and a second muon which was required to have been reconstructed in the CMX chamber and to be isolated (calorimeter Iso $< 4 \text{ GeV}$). Because a CMX muon could not be mistaken as the tight cut CMU/CMP muon, Equation 4.2 was used to determine the identification efficiencies of CMX muons.

$$\varepsilon_C = \frac{N_C}{N_{tot}} \pm \sqrt{\frac{N_C(N_{tot} - N_C)}{(N_{tot})^3}} \quad (4.2)$$

There were 547 events found in the Z mass window. Of these, 504 events passed

the loose CMX cuts, so the overall loose CMX identification efficiency was found to be $92.1 \pm 1.2\%$.

Table 4.4 lists the efficiencies for each of the muon identification cuts for tight and loose CMU/CMP muons and for loose CMX muons. The table also lists the efficiency for all of the cuts applied at once.

Table 4.4: Muon Identification Efficiencies

Cut	Tight	Loose	
	CMU/CMP	CMU/CMP	CMX
E (EM Tower)	$97.4 \pm 0.4\%$	$97.4 \pm 0.4\%$	$96.7 \pm 0.8\%$
E (HAD Tower)	$99.1 \pm 0.3\%$	$99.1 \pm 0.3\%$	$97.1 \pm 0.7\%$
HAD+EM	$99.2 \pm 0.2\%$	$99.2 \pm 0.2\%$	$99.1 \pm 0.4\%$
d_0 raw	$99.8 \pm 0.1\%$	$100.0 \pm 0.0\%$	$100.0 \pm 0.0\%$
d_0 beam	$98.7 \pm 0.3\%$	$99.7 \pm 0.2\%$	$100.0 \pm 0.0\%$
Matching	$98.5 \pm 0.3\%$	$98.5 \pm 0.3\%$	$98.9 \pm 0.4\%$
Track quality	$100.0 \pm 0.0\%$	$100.0 \pm 0.0\%$	$100.0 \pm 0.0\%$
All Cuts	$93.3 \pm 0.7\%$	$94.2 \pm 0.7\%$	$92.1 \pm 1.2\%$

4.2.2 Muon Reconstruction Efficiency

The above identification efficiencies were measured by assuming that every muon is reconstructed and therefore makes a CMUO bank. That is not the case, and the identification efficiencies are actually measured relative to the muon reconstruction efficiency. The total muon reconstruction efficiency, including stub finding in the muon chambers and track-stub linking, was measured using unbiased tracks from an inclusive muon sample. Events were selected which contained a tightly cut reconstructed muon (see Section 4.2.1) and one $p_T > 20$ GeV track not corresponding to the tight muon. For each event which the CMUSWM routine predicted that the track pointed at a muon chamber, it was determined whether a CMUO bank

corresponding to that track existed.

As with the identification efficiencies, Equation 4.1 was used to determine the CMU/CMP reconstruction efficiency, and Equation 4.2 was used to determine the CMX reconstruction efficiency. In this case, N_{tot} refers to the number of muon-track pairs for which CMUSWM points the track at a muon chamber; N_C refers to the subset of N_{tot} in which the track hits a muon chamber and a CMUO bank is created; and N_{TT} is the number belonging to the subset in which the track is reconstructed, a CMUO bank is created, and the corresponding muon passes the set of tight cuts.

The CMU/CMP reconstruction efficiency was found to be $97.3 \pm 0.5\%$. This measurement agrees well with that of the CDF B Meson analysis ($97.8 \pm 1.0\%$)^[17]. The CMX reconstruction efficiency was found to be $98.6 \pm 0.5\%$, which is consistent with another CDF study that measured a $98.9 \pm 1.0\%$ efficiency^[18].

4.3 SUSY Dilepton Sample

CDF recorded a multitude of events over the course of the 1994-1995 data run. A smaller sample of events, consisting only of dileptons, was created for use by SUSY analysis groups at CDF^[7]. The similarity of desired event signal allowed us to conveniently use this sample as the precursor to our event selection.

The SUSY dilepton sample consists of 457,475 events from the Run 1B Exotic Dilepton (XDLB_5P) data set. Each event is required to have at least one lepton – electron or muon – in the CEM or CMU/CMP chambers, as well as a second lepton in the CEM, PEM, CMU/CMP, or CMX chambers. The leptons are required to pass identification cuts that were in all cases either equal to or more loose than those described for our event selection. The required trigger path for the sample is

also far broader than what was chosen for this analysis.

4.4 Drell-Yan Dilepton Sample

Events were selected for the Drell-Yan data samples if at least one electron or muon passed the tight set of identification cuts in Tables 4.1 and 4.3 *and* at least one other electron or muon passed the loose identification cuts in Tables 4.1 and 4.3. If more than one lepton met either the tight or loose requirements, the lepton with the highest E_T (electron) or p_T (muon) was chosen. To exclude J/ψ and Υ backgrounds the lepton pair invariant mass was required to be greater than 11 GeV. The upper limit on the lepton pair invariant mass was chosen to be very high (600 GeV) to allow us to cross-check with published high-mass Drell-Yan and Z production cross-sections.

Selected events were stored in three ntuples: ee , comprised of $\gamma^*/Z \rightarrow e^+e^-$ signal plus background (12016 events: 8876 opposite-sign, 3140 same-sign); $\mu\mu$, comprised of $\gamma^*/Z \rightarrow \mu^+\mu^-$ signal plus background (23321 events: 15215 opposite-sign, 8106 same-sign); and an $e\mu$ dataset (28417 events: 16368 opposite-sign, 12049 same-sign) that will be used to estimate the amount of heavy flavor background in Section 7.4. After the trigger requirement (see Section 6.1.1) there were 8334 ee events (6390 opposite-sign, 1944 same-sign), 10374 $\mu\mu$ events (7278 opposite-sign, 3096 same-sign), and 15961 $e\mu$ events (9281 opposite-sign, 6680 same-sign).

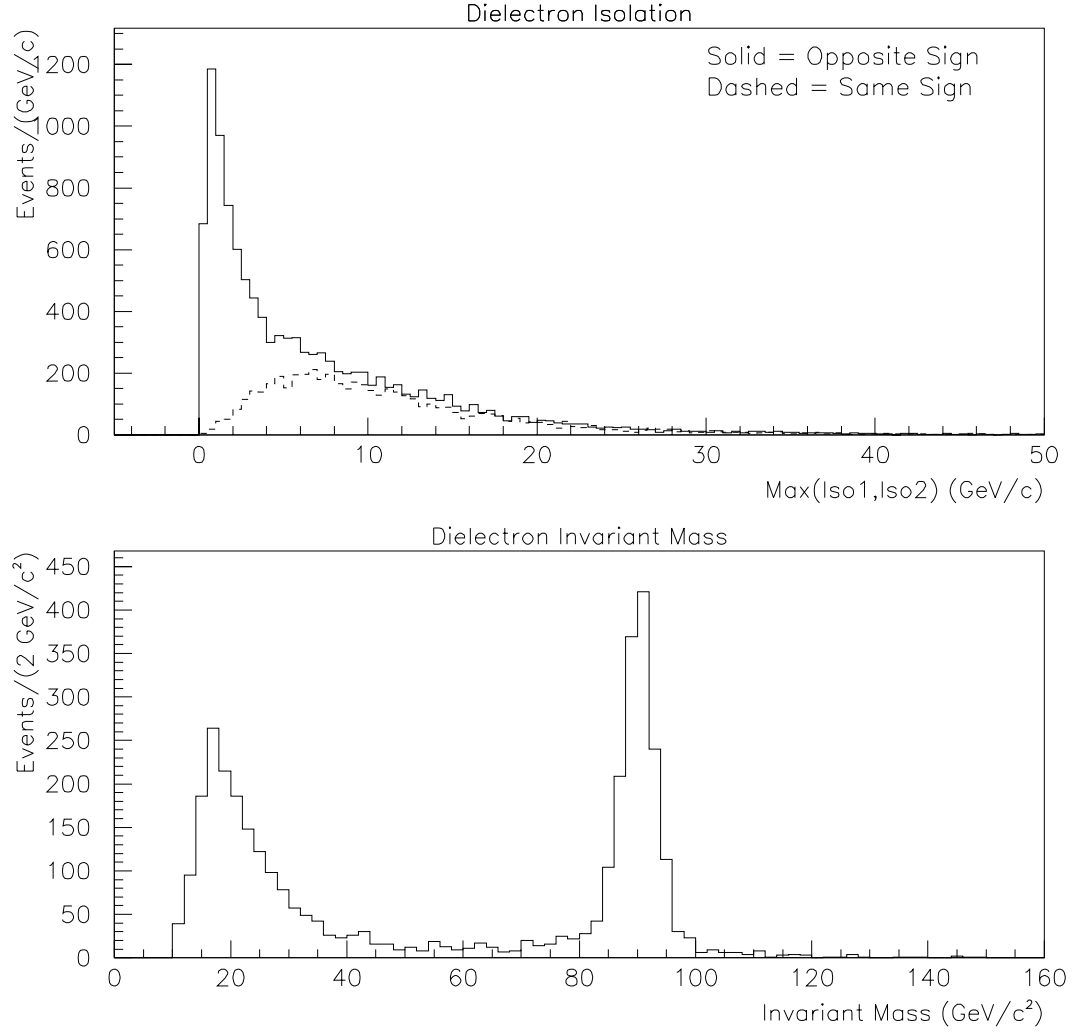


Figure 4.5: Isolation and Invariant Mass distributions for dielectrons in the Run 1B data sample. The top histogram shows the isolation distribution for opposite-sign and same-sign events. The bottom distribution shows the invariant mass distribution of opposite-sign events after the isolation cut.

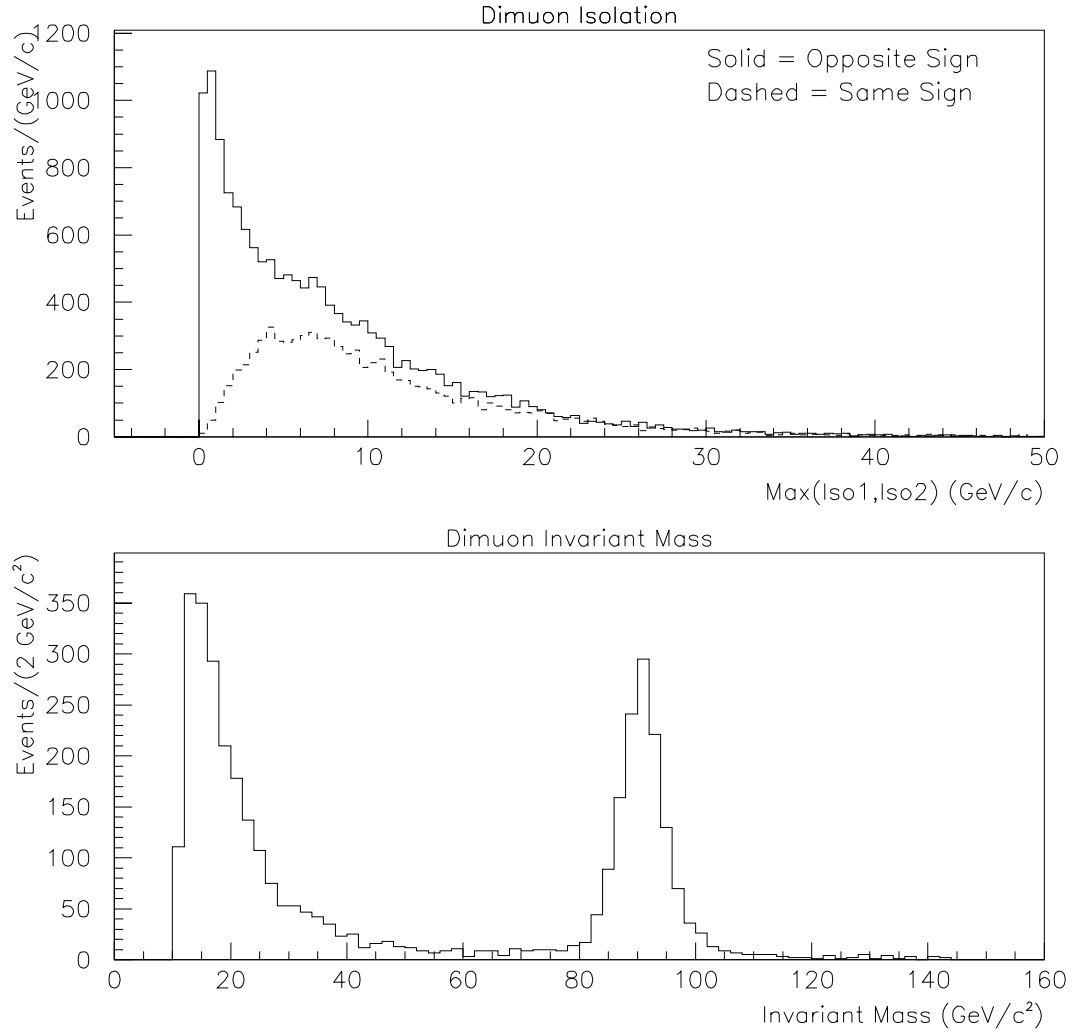


Figure 4.6: Isolation and Invariant Mass distributions for dimuons in the Run 1B data sample. The top histogram shows the isolation distribution for opposite-sign and same-sign events. The bottom distribution shows the invariant mass distribution of opposite-sign events after the isolation cut.

4.5 Other Efficiencies

4.5.1 Isolation Cut

An isolation cut is made to reduce backgrounds, and the isolation distributions are used to determine the heavy flavor background level. In this analysis, isolation of a single lepton is defined as the sum (in quadrature) of calorimeter isolation and track isolation in an $\eta - \phi$ cone of radius 0.4. For track isolation, only tracks with $p_T > 0.4$ GeV are included in the sum. For a lepton pair, isolation of the pair, I , is defined as the maximum of the isolation values for the two leptons. Figures 4.5 and 4.6 show the isolation and invariant mass distributions: for dielectron pairs, and dimuon pairs, respectively. In each figure, the top histogram shows the isolation distribution for opposite-sign and same-sign pairs before the isolation cut. No normalization factor has been applied to either distribution. From the top plots in Figures 4.5 and 4.6, it is clear that a cut of $I < 2$ GeV removes most of the opposite/same-sign symmetric misidentification background, while retaining a high fraction of the excess of opposite-sign events which is largely signal. In each figure, the bottom distribution shows the invariant mass distribution of opposite-sign events after the isolation $I < 2$ GeV cut.

The efficiency of the pair isolation cut $I < 2$ GeV was obtained by relaxing the isolation cut on Z events in this data sample and determining how many Z events were cut by the isolation requirement. For dielectrons, the isolation efficiency was measured as $68.1 \pm 1.3\%$, while for dimuons, the isolation efficiency was measured as $75.6 \pm 1.6\%$.

The mean isolation in the dielectron Z sample appears shifted by +0.5 GeV relative to the dimuon Z sample. This is consistent with other observations that the

lower isolation efficiency for dielectrons is due to electron leakage in the ϕ calorimeter towers^[8]. Since the muon isolation is not affected by leakage, we assume the following linear E_T dependence for the dielectron isolation efficiency by interpolating between dimuon (no leakage) and dielectron (full leakage) isolation efficiencies:

$$\varepsilon_{iso}^{ee}(E_T^1, E_T^2) = 0.756 - 0.074 \times \frac{(E_T^1 + E_T^2)}{(E_T^1 + E_T^2)_Z} \quad (4.3)$$

where E_T^1 and E_T^2 are the mean transverse energies of electrons 1 and 2, respectively, and $(E_T^1 + E_T^2)_Z = 83.61$ GeV is their sum in the Z mass window where the above isolation efficiencies were calculated. Table 4.5 lists the isolation efficiency for each dielectron mass bin.

After the isolation cut the following numbers of events remained in each sample: 2712 ee (2651 opposite-sign, 61 same-sign), 2182 $\mu\mu$ (2062 opposite-sign, 120 same-sign), and 697 $e\mu$ (465 opposite-sign, 232 same-sign).

Table 4.5: Dielectron isolation efficiencies for each mass bin.

Mass bin (GeV)	E_T^1 (GeV)	E_T^2 (GeV)	$\frac{(E_T^1 + E_T^2)}{(E_T^1 + E_T^2)_Z}$	ε_{iso}^{ee}
11-15	6.106	9.731	0.189	0.742 \pm 0.014
15-20	7.346	10.67	0.215	0.740 \pm 0.014
20-30	9.96	13.39	0.279	0.735 \pm 0.014
30-40	13.96	18.50	0.388	0.727 \pm 0.014
40-50	17.84	24.79	0.510	0.718 \pm 0.014
50-60	21.58	30.66	0.625	0.709 \pm 0.014
60-70	26.22	34.20	0.723	0.702 \pm 0.013
70-110	38.09	45.52	1.000	0.681 \pm 0.013
110-150	52.70	60.53	1.354	0.655 \pm 0.013

4.5.2 Z Vertex Cut Efficiency

An additional luminosity correction was made, because we removed events for which the z vertex position was not within 60 cm of the interaction point. This efficiency is known to be $93.7 \pm 1.1\%$ [9].

Chapter 5

Monte Carlo Simulation

Monte Carlo simulations were used to generate several samples of Drell-Yan events used in the acceptance and trigger efficiency calculations (Chapter 6) and in the $Z \rightarrow \tau^+\tau^-$ background estimation (Section 7.3). These simulations are described in detail below.

5.1 Event Generation

The Drell-Yan Monte Carlo event samples were generated using HERWIG version 5.8^[19]. In all cases, except to obtain a systematic uncertainty due to structure function selection, the MRS-R2 structure function set was used. During event generation, PHOTOS was used to simulate photon radiation in decays^[20]. We used standard PHOTOS parameter settings^[21].

For the acceptance and trigger efficiency calculations it was desirable to have equivalent statistical significance for each mass bin. Therefore, 100,000 Drell-Yan events were generated in each of the following boson mass ranges: 1-6, 6-11, 11-15, 15-20, 20-30, 30-40, 40-50, 50-60, 60-70, 70-110, 110-150, 150-200, and 200-600 GeV.

Events were also generated in wider mass ranges in order to make comparisons between the data and Monte Carlo transverse momentum distributions. The wider mass ranges were necessary, because photon radiation could cause the lepton pair mass to fall well below the generated (boson) mass, and therefore such events could effect the transverse momentum distributions of neighboring mass bins. The effects of photon radiation are discussed in greater detail in Section 6.2. The mass ranges generated (used to plot p_T in range) were: 9-50 (11-40), 30-150 (40-110), and 70-250 (110-200) GeV.

For all generated events, four-momenta, charge, and lepton type were kept for each lepton, and the data was stored in ntuple form along with the generated boson mass. Information from the photon decays simulated by PHOTOS was stored in the ntuple as well, so that the detector simulation could predict whether the radiated photons would effect the lepton isolation cones or the reconstructed energies.

5.2 Detector Simulation

This section describes how we simulated the response of the CDF detector to the generated electrons and muons. For each Monte Carlo lepton pair we applied the probability that the event would pass one of the trigger paths. This is described in more detail in Section 6.1.4.

5.2.1 Electron Detector Simulation

Monte Carlo electrons were required to be fiducial in the CEM. This was tested with a routine called FIDVOL which used the generated momenta of the electrons to “swim” them through the CDF detector and determine which, if any, calorime-

ter towers were hit. If PHOTOS generated any photons in the event, FIDVOL was called for each photon to determine if its energy was deposited in the same calorimeter tower as an electron. If so, the photonic energy was added to the electron energy to determine the invariant mass of the event. If a photon was not in the same tower as an electron but was within the isolation cone of the electron, the event was not considered if the photonic energy was greater than the isolation cut (2 GeV).

For electrons that were within the fiducial volume of the CEM, the energies were smeared according to the CEM energy resolution. This was done by adding to the E_T of the electron a random number from a Gaussian distribution with a mean of zero and a width corresponding to the transverse energy resolution:

$$\delta E_T = \sqrt{(.135 \times \sqrt{E_T})^2 + (.015 \times E_T)^2} \quad (5.1)$$

where E_T is measured in units of GeV.

Figures 5.1 through 5.3 show the transverse energy distributions of Monte Carlo generated electrons in each mass bin. The transverse energy distributions of accepted, triggered electrons are shown next to the generated distributions for comparison. Figures 6.11 and 6.12 show the comparison of data and Monte Carlo transverse energy distributions for accepted, triggered electron pairs.

Figure 5.5 shows the η and ϕ tower distributions of accepted, triggered Monte Carlo electrons compared to electrons that were selected for our data samples. The horizontal axes represent the integer calorimeter tower numbers. The points with errors represent the data, while the solid line represents the Monte Carlo distribution. Figure 5.6 shows the distribution of phi for electrons within the calorimeter towers. The figure reveals that the detector simulation is under-efficient at removing

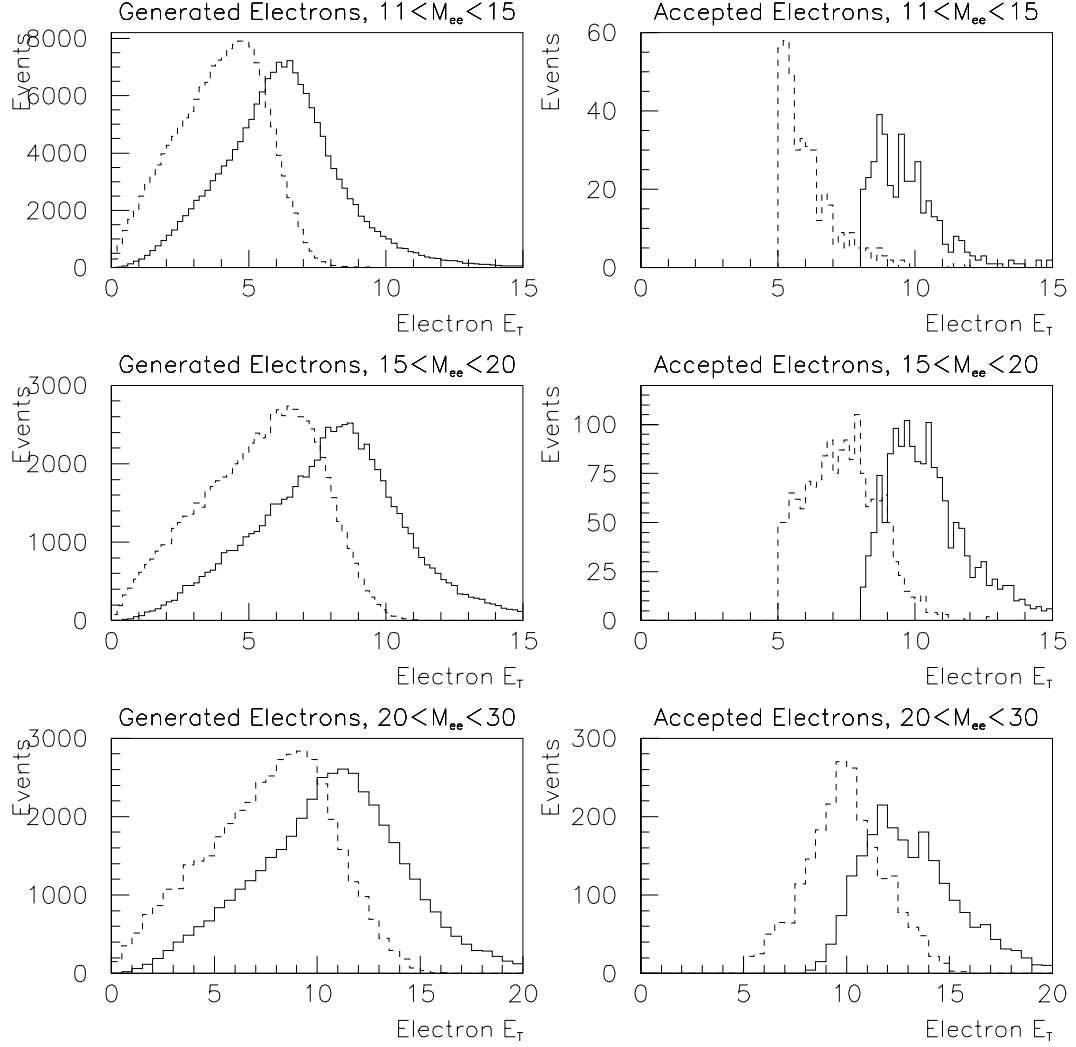


Figure 5.1: Generated and accepted Monte Carlo simulated electron E_T distributions. The E_T distributions are shown for generated high- E_T (solid line) and low- E_T (dashed line) electrons in each mass bin. To the right of the generated distributions are the E_T distributions of accepted, triggered Monte Carlo electrons.

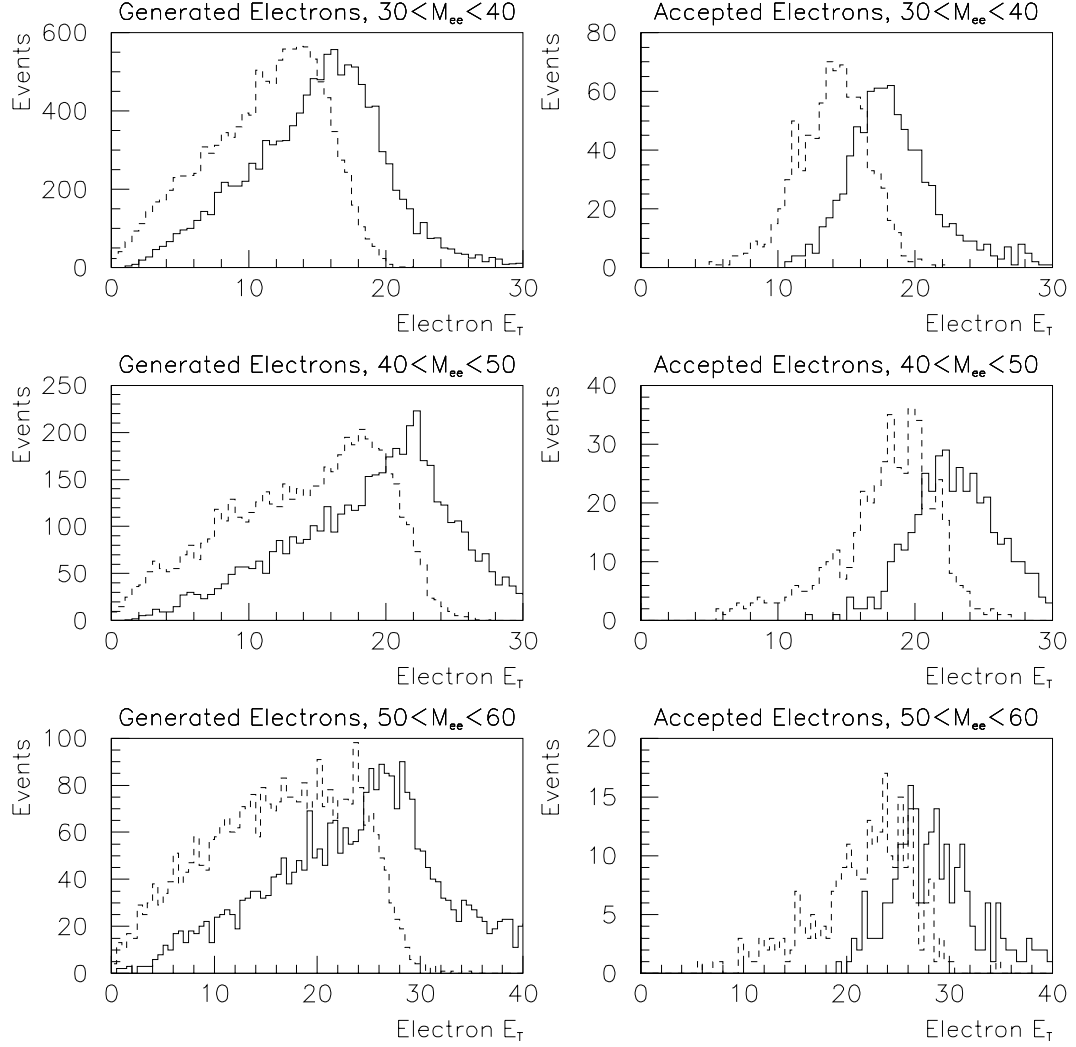


Figure 5.2: Generated and accepted Monte Carlo simulated electron E_T distributions. The E_T distributions are shown for generated high- E_T (solid line) and low- E_T (dashed line) electrons in each mass bin. To the right of the generated distributions are the E_T distributions of accepted, triggered Monte Carlo electrons.

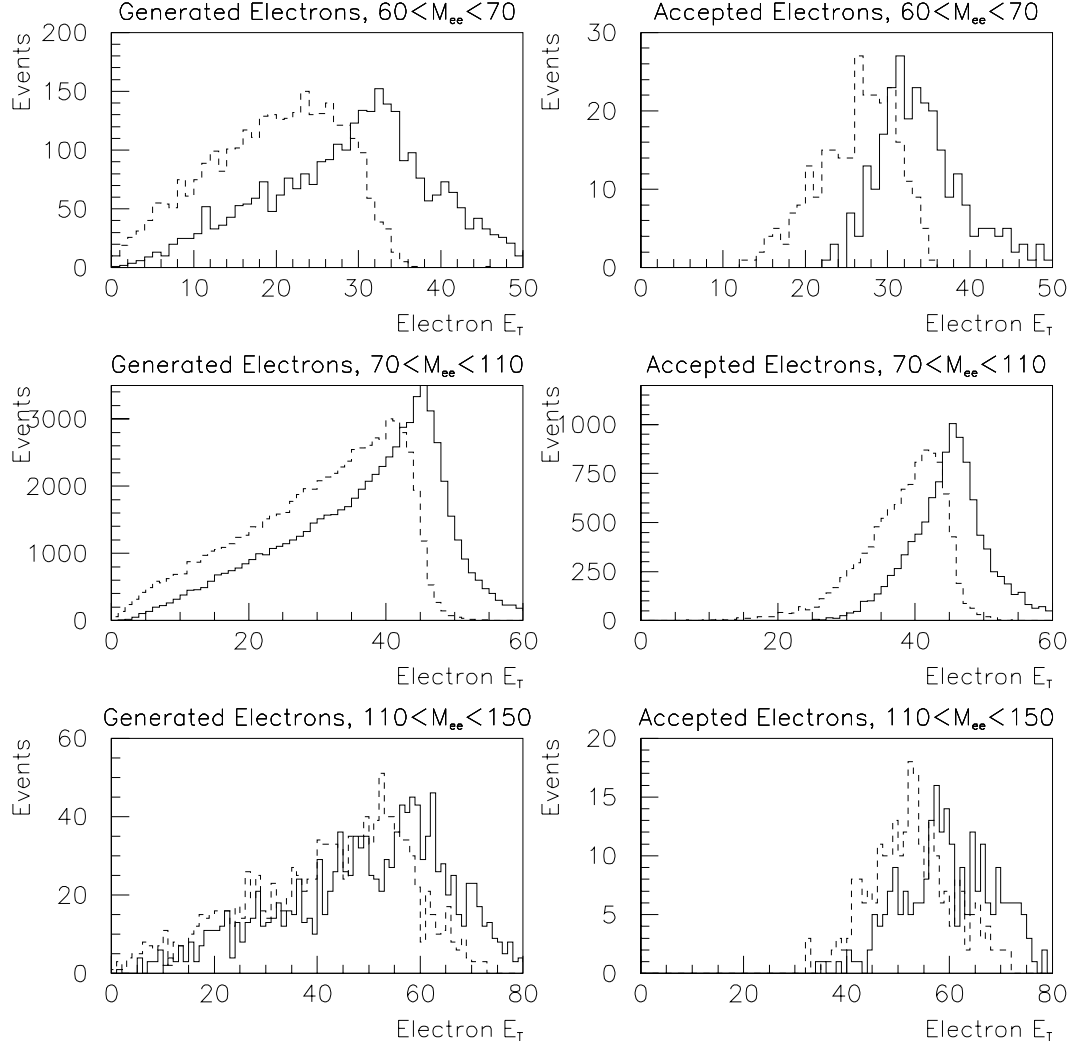


Figure 5.3: Generated and accepted Monte Carlo simulated electron E_T distributions. The E_T distributions are shown for generated high- E_T (solid line) and low- E_T (dashed line) electrons in each mass bin. To the right of the generated distributions are the E_T distributions of accepted, triggered Monte Carlo electrons.

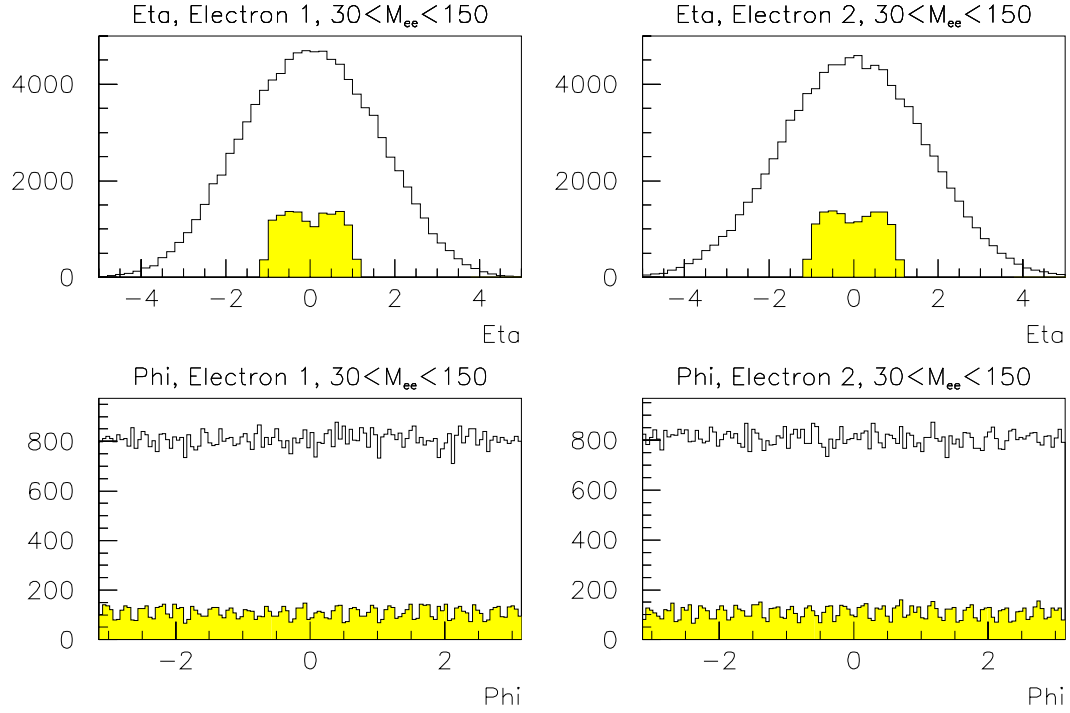


Figure 5.4: Generated and accepted Monte Carlo simulated electron η and ϕ distributions. The η and ϕ distributions are shown for generated (outer histogram) and accepted, triggered (inner histogram) electrons. The top two plots are the η distributions for the tight and loose electrons. The bottom two plots are the ϕ distributions for the tight and loose electrons.

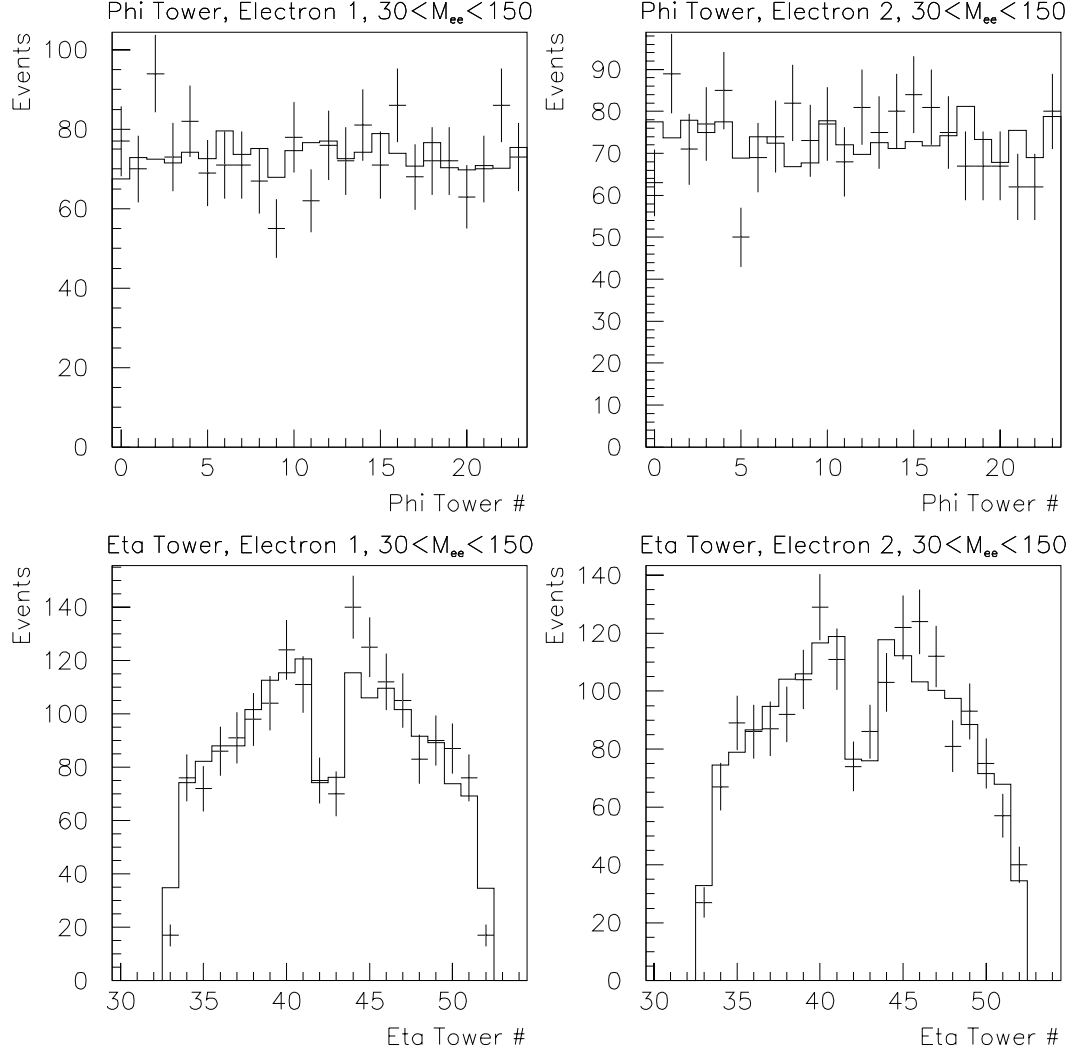


Figure 5.5: Comparison of data and Monte Carlo simulated electron η and ϕ distributions. The top two plots show the ϕ distributions of electron 1 and electron 2, where the ϕ binning is done according to the integer number representing the ϕ tower of the calorimeter. The bottom two plots show the calorimeter η tower for electron 1 and electron 2. The points with errors represent the data, while the solid line represents the Monte Carlo distribution.

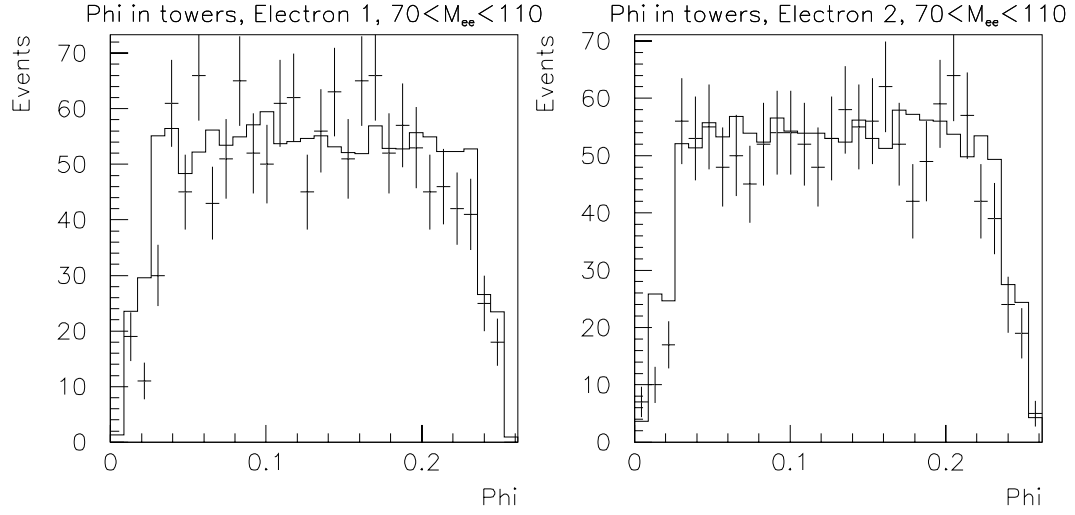


Figure 5.6: Comparison of data and Monte Carlo simulated electron ϕ distributions within calorimeter towers. The histograms for each of the 24 ϕ towers were summed to show the ϕ distribution of electrons within a calorimeter tower. The points with errors represent the data, while the solid line represents the Monte Carlo distribution.

electrons near the tower edge. The extent of this under-efficiency and its bearing on the systematic uncertainty of the acceptance is discussed in Section 5.2.3.

5.2.2 Muon Detector Simulation

Monte Carlo muons were required to be fiducial in the central muon chambers. This was tested with a standard CDF routine, CMUSWM, which used the generated momenta of the muons to “swim” them through the CDF detector and determine which, if any, muon chambers were hit. If PHOTOS generated any photons in the event, FIDVOL was called for each photon to determine if its energy was deposited in the same calorimeter tower as a muon. If so, the photonic energy was added to the simulated muon EM energy, and the event was cut if the total EM energy was greater than the muon EM energy cut (2 GeV). If a photon was not in the same

tower as a muon but was within the isolation cone of the muon, the event was not considered if the photonic energy was greater than the isolation cut (2 GeV).

For muons that were within the fiducial volume of the CMU, CMP, or CMX, the momenta were smeared according to the CTC tracking resolution. This was done by adding to the p_T of the muon a random number from a Gaussian distribution with a mean of zero and a width corresponding to the transverse momentum resolution $\delta p_T^{-1} = 0.001$.

Figures 5.7 through 5.9 show the transverse energy distributions of Monte Carlo generated muons in each mass bin. The transverse energy distributions of accepted, triggered muons are shown next to the generated distributions for comparison. Figures 6.11 and 6.12 show the comparison of data and Monte Carlo transverse momentum distributions for accepted, triggered muon pairs.

Figures 5.11 and 5.12 show the ϕ tower distribution of accepted, triggered Monte Carlo muons compared to muons that were selected for our data samples. The horizontal axis is the calorimeter ϕ tower number that the muon hit. The points with errors represent the data, while the solid line represents the Monte Carlo distribution. Since our muon triggers require a CMUP muon, the first muon in these plots was required to be CMUP in order to eliminate trigger effects. The ϕ tower distribution of the second muon is plotted with the following muon chamber requirements: any chamber (CMU/CMP/CMX, CMUP, CMX only, CMU only, and CMP only). The figures reveal that the detector simulation is under-efficient at removing muons where the chambers do not exist. The extent of this under-efficiency and its bearing on the systematic uncertainty of the acceptance is discussed in the next section.

Figure 5.13 shows the comparison of data and Monte Carlo muon η distributions. The horizontal axis is the calorimeter η tower number that muon hit. The

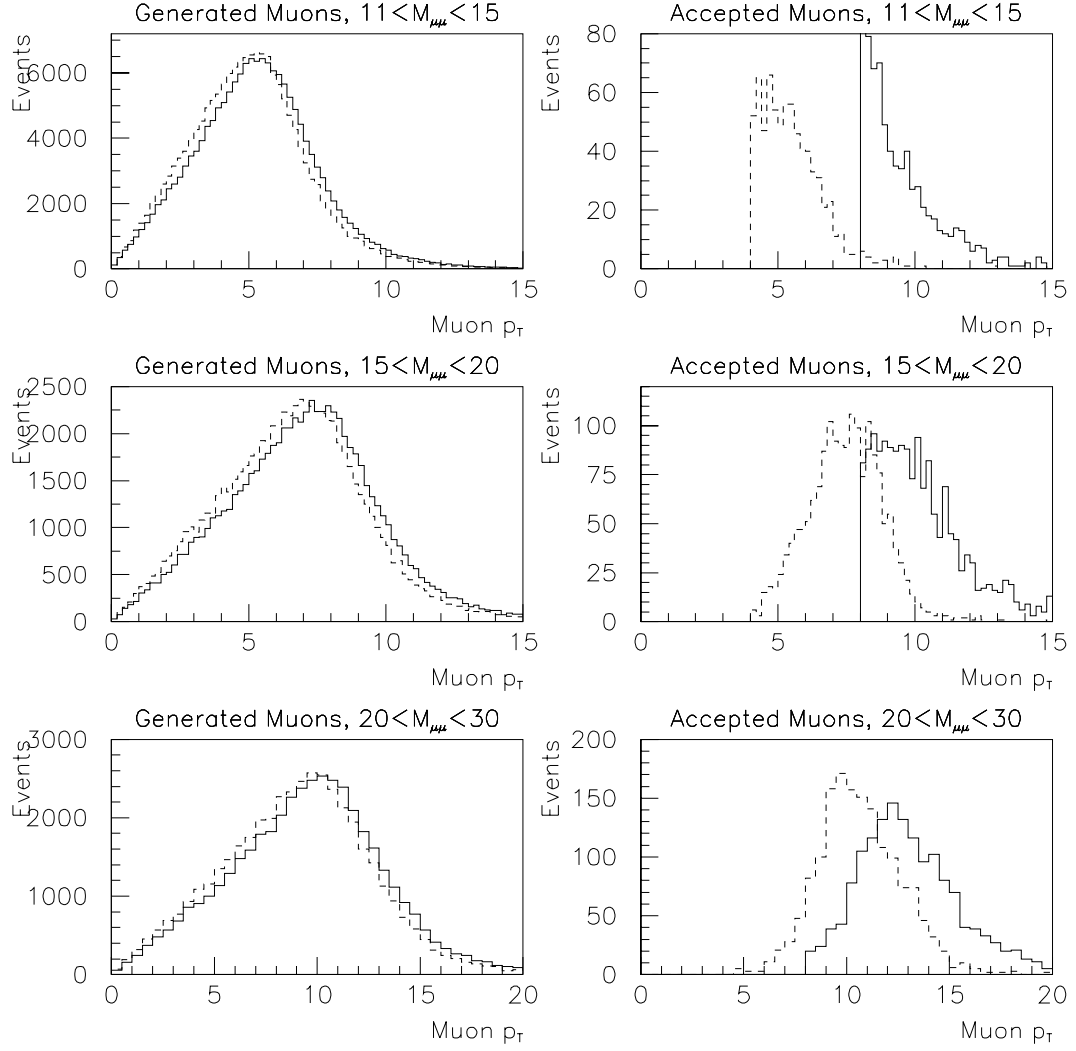


Figure 5.7: Generated and accepted Monte Carlo simulated muon p_T distributions. The p_T distributions are shown for generated high- p_T (solid line) and low- p_T (dashed line) muons in each mass bin. To the right of the generated distributions are the p_T distributions of accepted, triggered Monte Carlo muons.

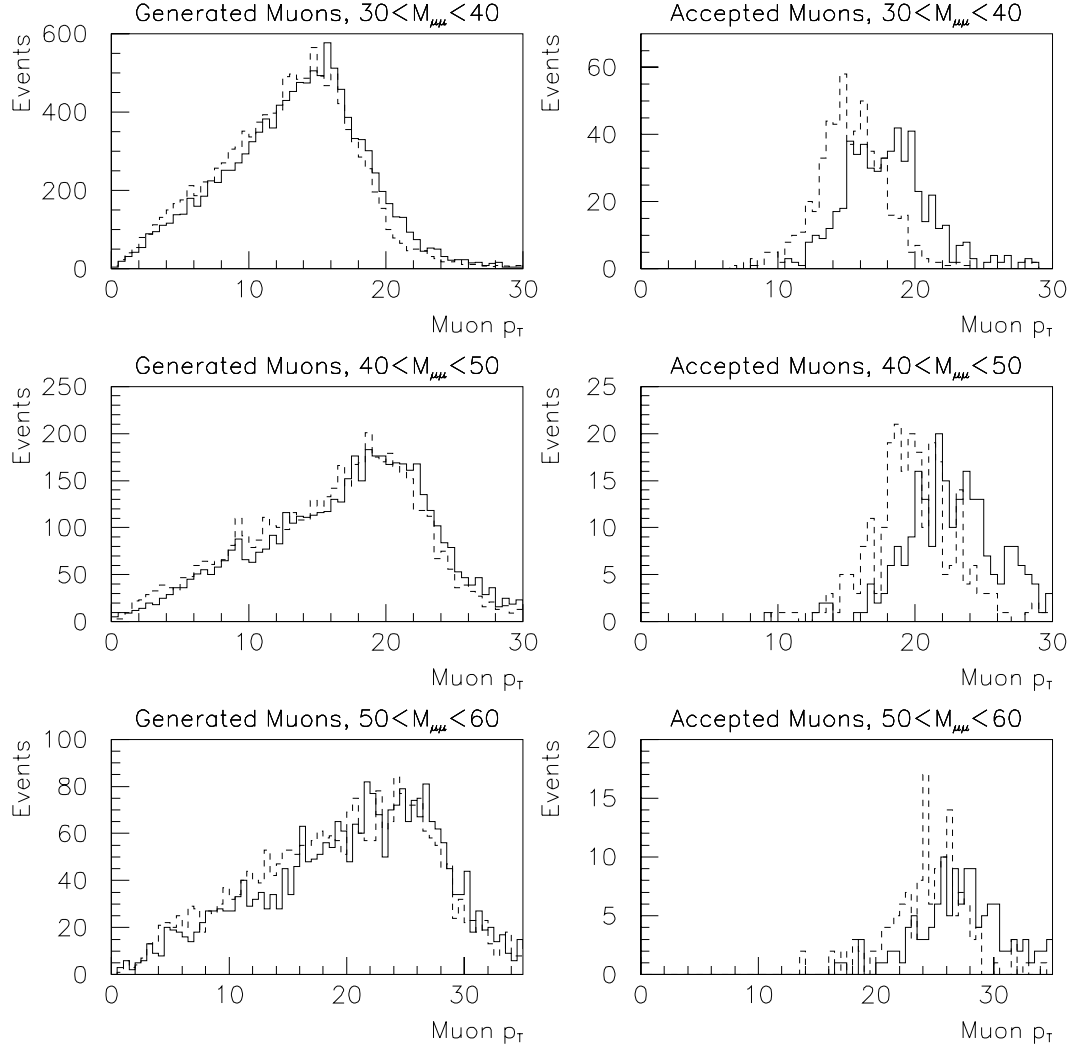


Figure 5.8: Generated and accepted Monte Carlo simulated muon p_T distributions. The p_T distributions are shown for generated high- p_T (solid line) and low- p_T (dashed line) muons in each mass bin. To the right of the generated distributions are the p_T distributions of accepted, triggered Monte Carlo muons.

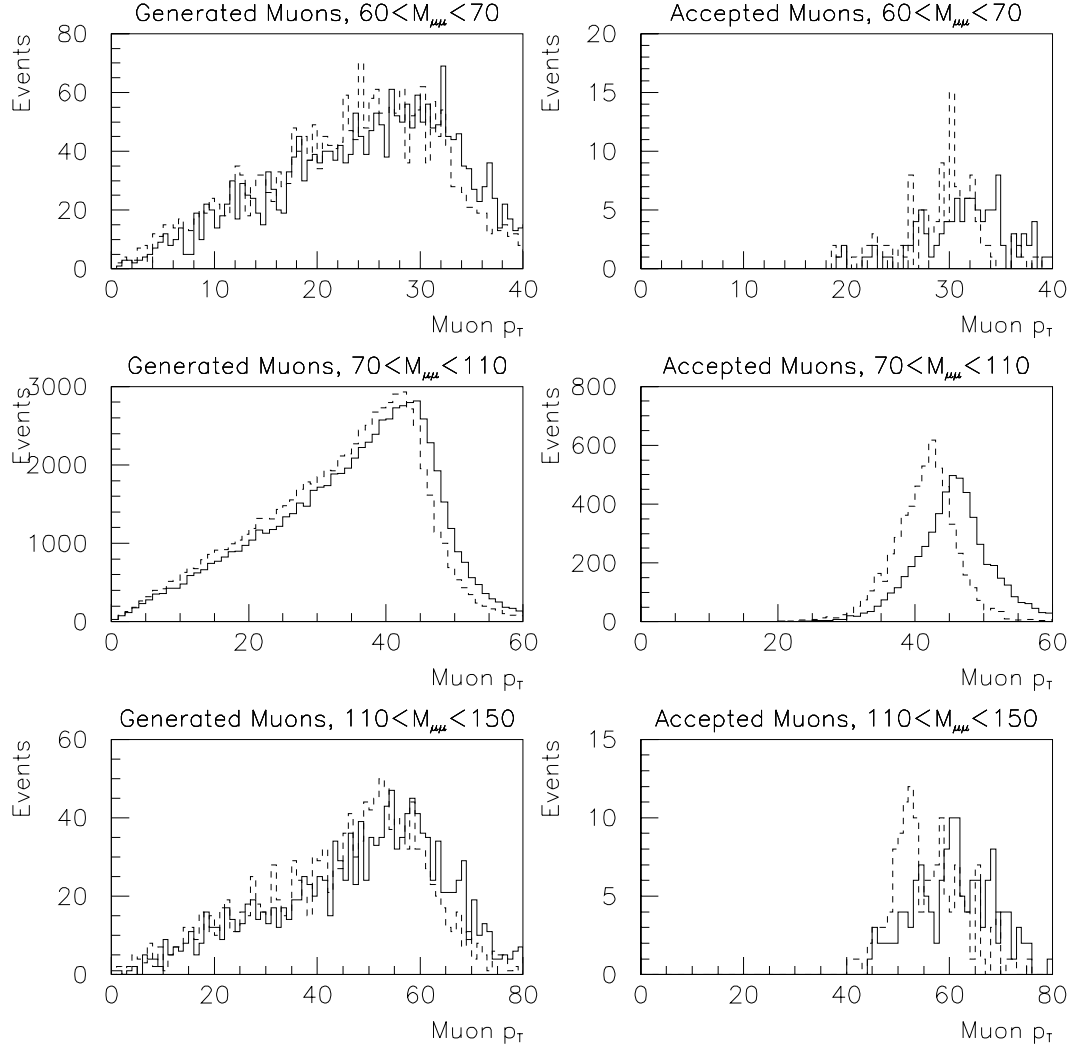


Figure 5.9: Generated and accepted Monte Carlo simulated muon p_T distributions. The p_T distributions are shown for generated high- p_T (solid line) and low- p_T (dashed line) muons in each mass bin. To the right of the generated distributions are the p_T distributions of accepted, triggered Monte Carlo muons.

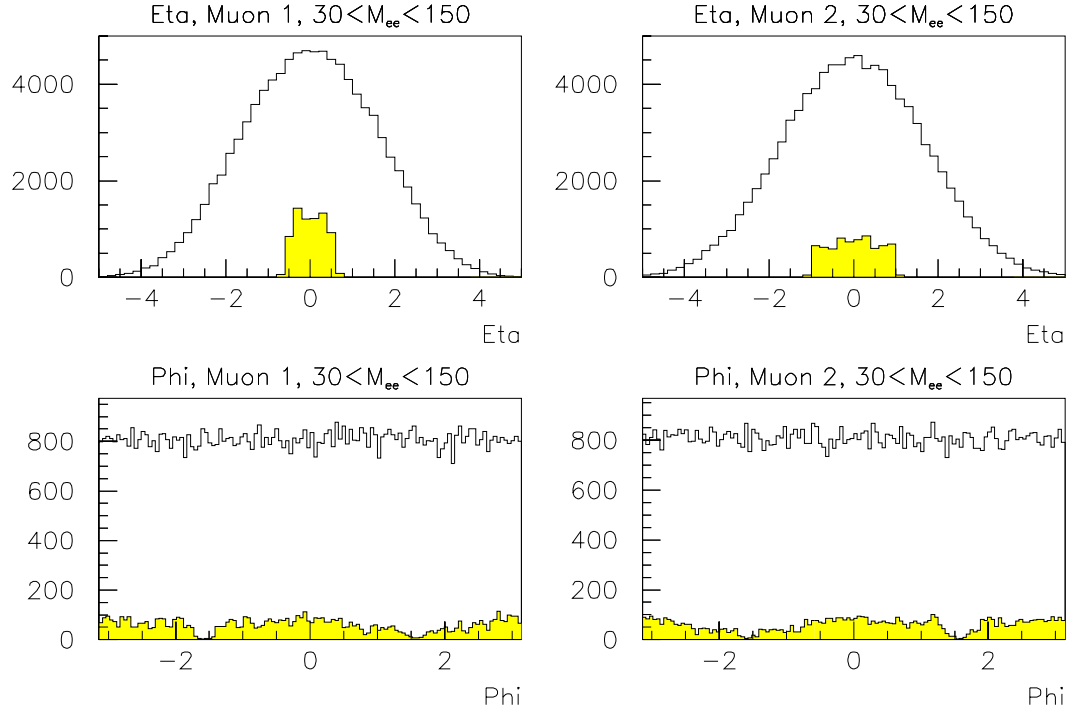


Figure 5.10: Generated and accepted Monte Carlo simulated muon η and ϕ distributions. The η and ϕ distributions are shown for generated (outer histogram) and accepted, triggered (inner histogram) muons. The top two plots are the η distributions for the tight and loose muons. The bottom two plots are the ϕ distributions for the tight and loose muons.

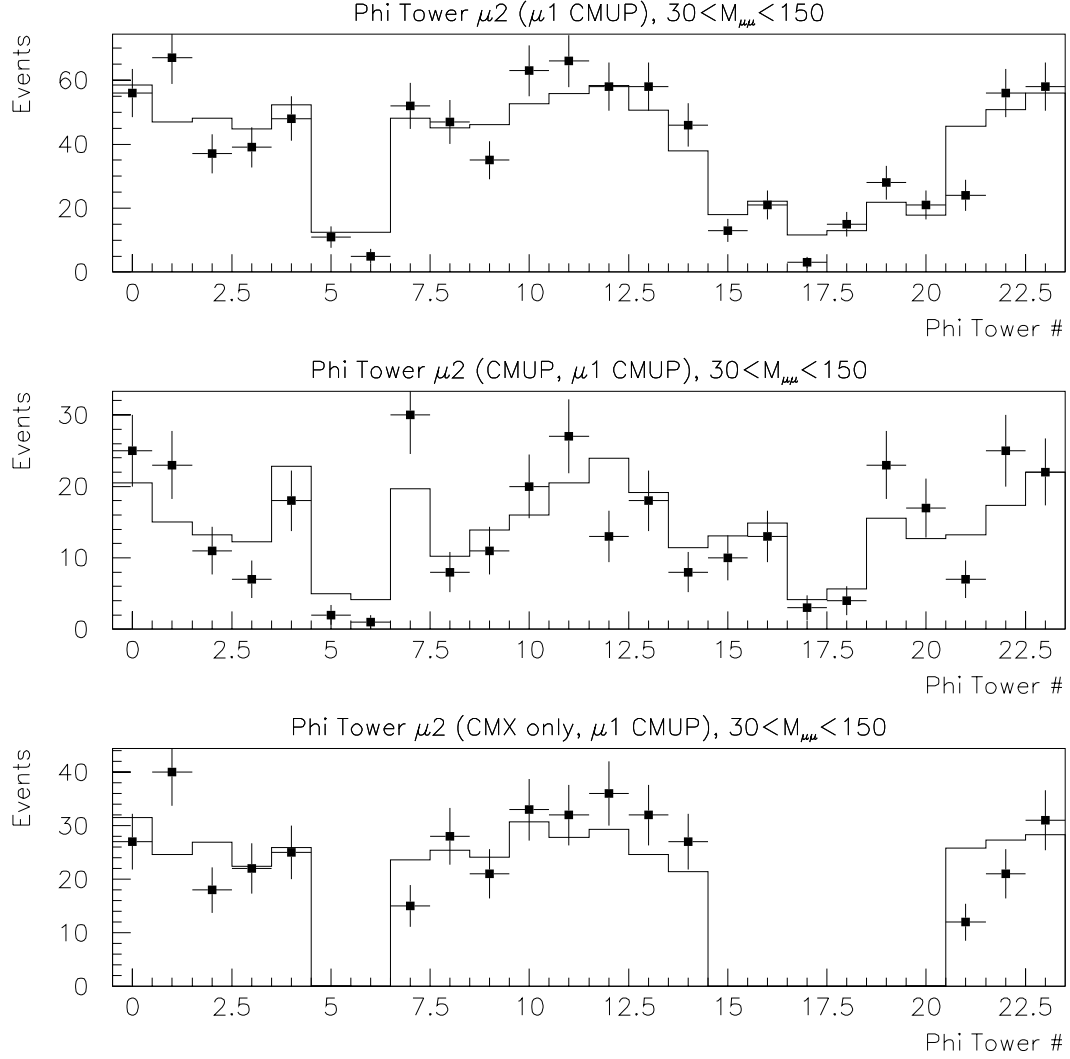


Figure 5.11: Comparison of data and Monte Carlo simulated muon ϕ distributions. The ϕ distribution of the second muon is shown for events in which the first, tight-cut muon hit both the CMU and CMP chambers (CMUP). This eliminates trigger effects on the distribution of the second muon. The middle plot shows the same distribution when the second muon was also required to be CMUP. The bottom plot shows the distribution for muons that hit the CMX chamber. The points with errors represent the data, while the solid line represents the Monte Carlo distribution.

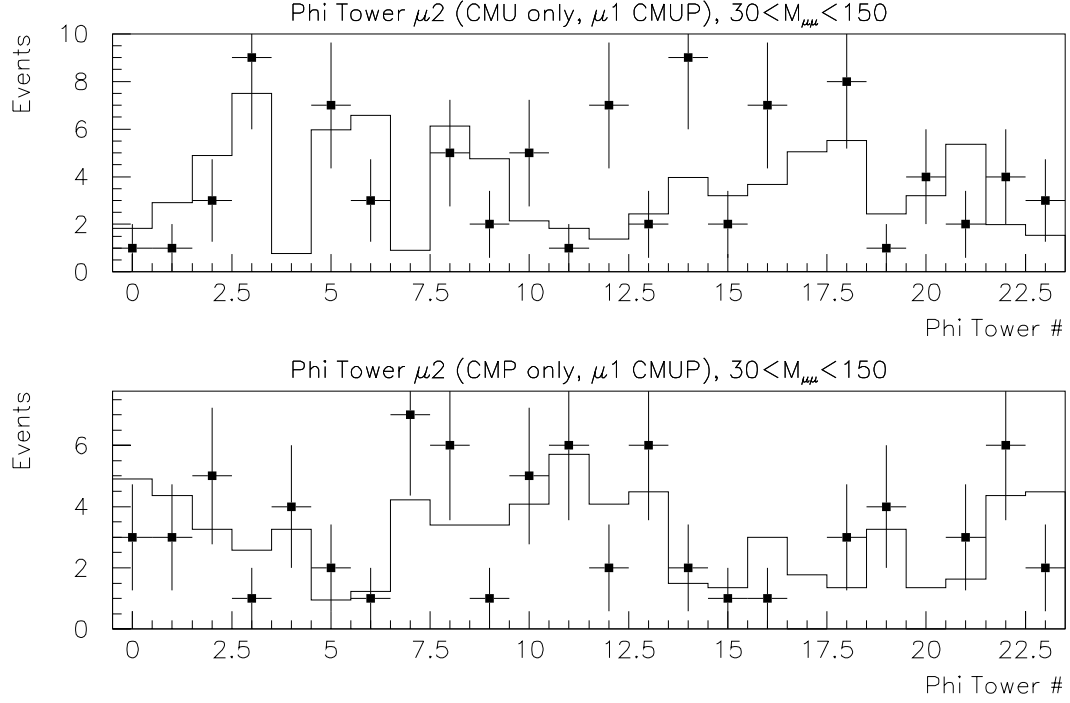


Figure 5.12: Comparison of data and Monte Carlo simulated muon ϕ distributions. The ϕ distribution of the second muon is shown for events in which the first, tight-cut muon hit both the CMU and CMP chambers (CMUP). This eliminates trigger effects on the distribution of the second muon. The top plot shows the ϕ distribution for muons that were CMU only. The bottom plot shows the ϕ distribution for muons that were CMP only. The points with errors represent the data, while the solid line represents the Monte Carlo distribution.

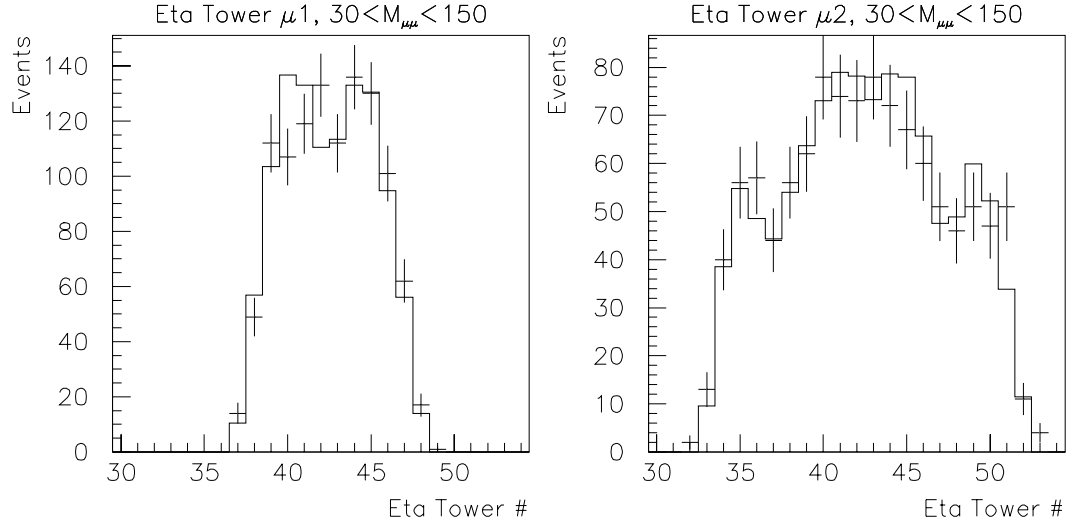


Figure 5.13: Comparison of data and Monte Carlo simulated muon η distributions. The plots show the η distributions of the tight and loose-cut muons. The binning is done according to the integer number representing the calorimeter tower that was hit.

wider distribution of the second muon shows the extent of the CMX chamber. Figure 5.14 shows the comparison of data and Monte Carlo muon ϕ distributions within calorimeter towers. The histograms for each of the 24 ϕ towers were summed to show the phi distribution of muons within a calorimeter tower.

5.2.3 Systematic Uncertainty from Detector Simulation

Figures 5.6 and 5.11 show that while our detector simulation effectively models the majority of the CDF detector, it is slightly inefficient at removing leptons that are close to detector edges and cracks. We estimate the magnitude of this inefficiency in order to determine a systematic uncertainty for our measurement.

The two plots in Figure 5.6 are used to estimate the uncertainty due to the electron detector simulation. In each plot we normalize the number of Monte Carlo electrons in the mid-tower region to the number in the data sample by excluding

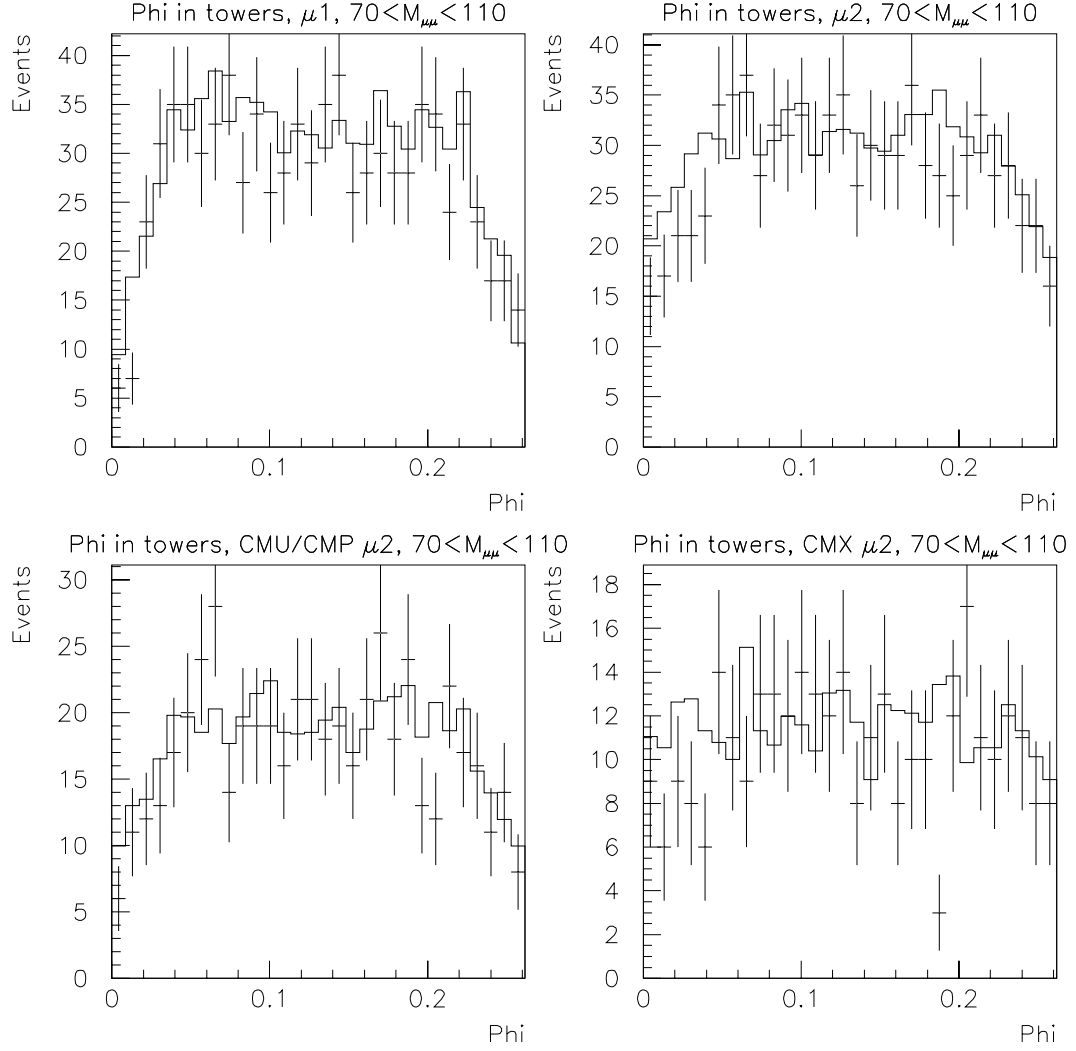


Figure 5.14: Comparison of data and Monte Carlo simulated muon ϕ distributions within calorimeter towers. The histograms for each of the 24 ϕ towers were summed to show the ϕ distribution of muons within a calorimeter tower. The points with errors represent the data, while the solid line represents the Monte Carlo distribution.

the four bins on each edge of the tower. The percent difference in the total number of events (including the edges) in the data and the normalized Monte Carlo is the estimated uncertainty. The uncertainties for the tight and loose electrons were 4.6% and 2.0%, respectively, and the total dielectron detector simulation uncertainty is 5.0%.

The top two plots in Figure 5.11 are used to estimate the uncertainty due to the muon detector simulation. From the discrepancy in the crack regions (towers 5-6 and 15-20) of the top plot we estimate the systematic uncertainty for a CMU/CMP/CMX muon as 1.5%. From the discrepancy in the crack regions (towers 5-6 and 17-18) of the middle plot we estimate the systematic uncertainty for a CMUP muon as 2.7%. The total dimuon detector simulation uncertainty is therefore 3.1%.

Chapter 6

Trigger Efficiencies and Detector Acceptance

This chapter describes how the efficiencies of the trigger path requirements were determined first as a function of transverse energy or momentum, as well as how the “turn-on” curves were applied to Monte Carlo events to find the trigger efficiency (ε_{trig}) for each mass range. This chapter also describes the detector acceptance (A) determination using Monte Carlo simulation and the effects of photon radiation on the Drell-Yan mass distribution. Two systematic uncertainties were studied for the product $A \times \varepsilon_{trig}$ by scaling the lepton pair p_T distributions and by varying the Monte Carlo structure function set.

6.1 Trigger Efficiency Determination

Electron and muon trigger paths were chosen, and the efficiencies were measured as functions of E_T for electrons and p_T for muons. Average trigger prescale factors are determined by the CDF routine SIGMON^[12]. For any given trigger, SIGMON

examines the online luminosity database to find the luminosity of the trigger for each run and compares that to the total luminosity for the run. The ratio gives the effective prescale of the trigger, which is then averaged over all runs.

6.1.1 Data Paths

The following electron and muon trigger paths were chosen (see Figure 6.1 and Figure 6.2):

Electron Path:

Level 1: trigger *L1_CALORIMETER_V3* or *L1_CALORIMETER_BBC_V3*, which triggered electrons with a CEM tower threshold energy > 8 GeV.

Level 2: trigger *CEM_16_CFT_12* (required CEM $E_T > 16$ GeV and track $p_T > 12$ GeV) or *CEM_8_CFT_7.5_XCES* (which was prescaled by an average factor of 1.15 and required CEM $E_T > 8$ GeV and track $p_T > 7.5$ GeV).

Level 3: trigger *ELEB_CEM_8_6* ($E_T > 7.5$ GeV and $p_T > 6$ GeV).

Muon Path:

Level 1: trigger *CMU_CMP_6PT0_HTDC* or *CMU_CMP_6PT0_HTDC_BBC*, which required hits in the CMU or CMP chambers as well as $p_T > 6$ GeV.

Level 2: trigger *CMUP_CFT_12_5DEG* (required $p_T > 12$ GeV and hits in the CMU and CMP) or *CMUP_CFT_7.5_5DEG* (which was prescaled by an average factor of 1.74 and required $p_T > 7.5$ GeV and hits in the CMU and CMP). The above Level 1 triggers were prerequisites for both of these Level 2 triggers.

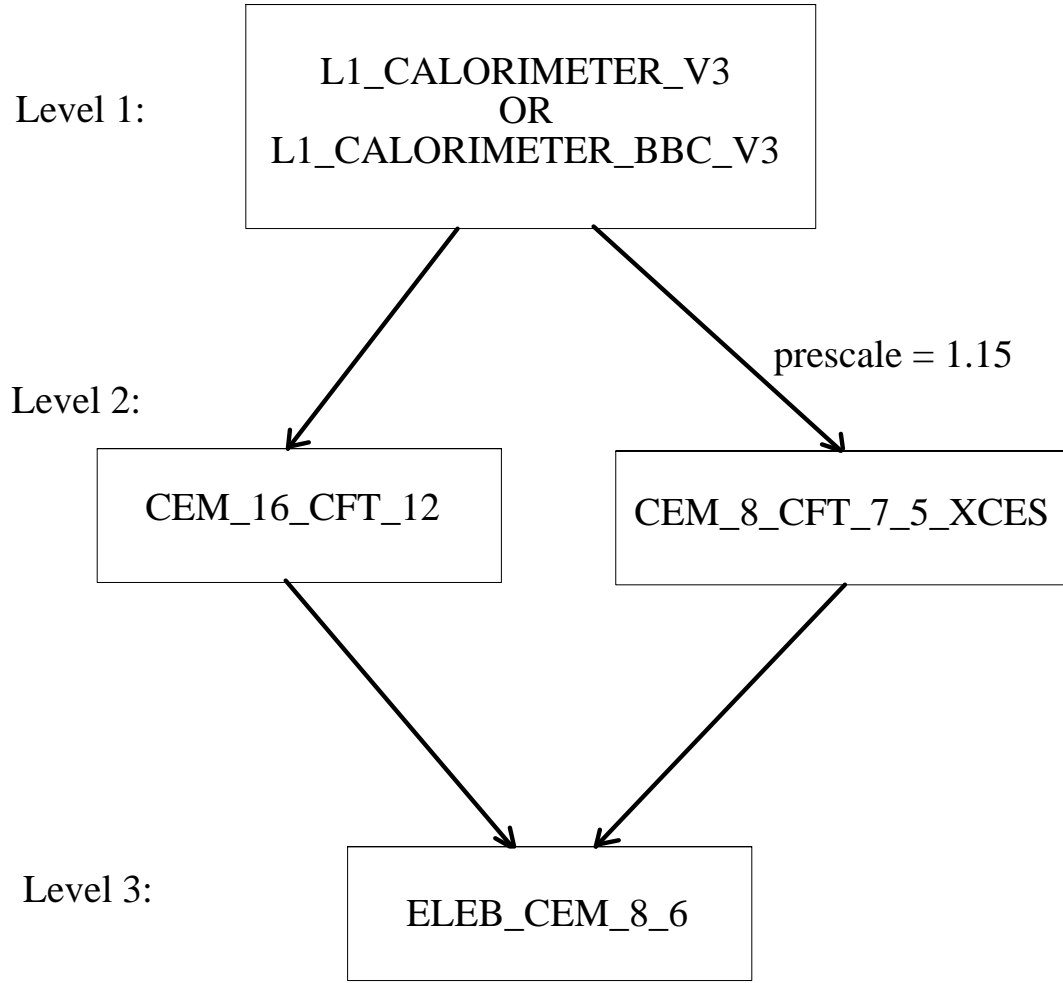


Figure 6.1: Electron trigger path.

Level 3: trigger *MUOB_CMU_CMP_8* or *MUOC_CMU_CMP_6PT0*, which had minimum p_T requirements of 8 GeV and 6 GeV, respectively.

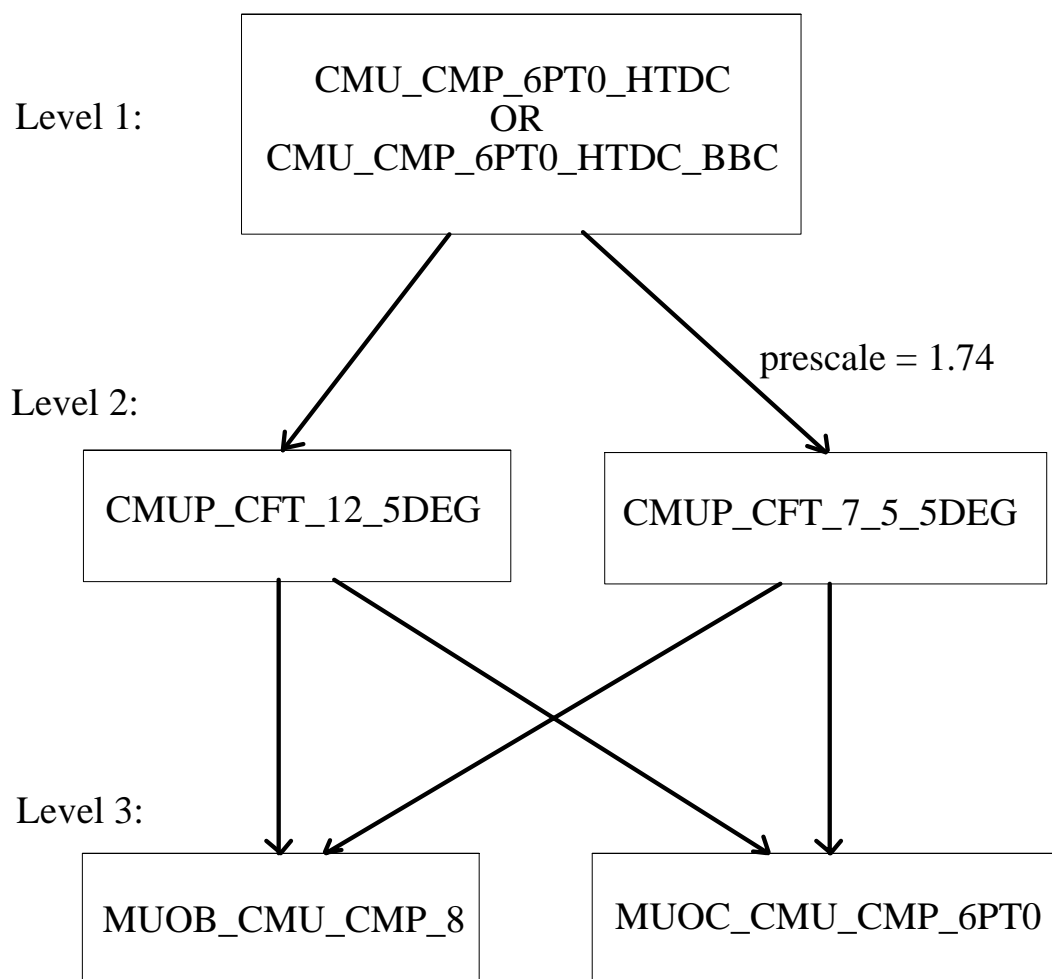


Figure 6.2: Muon trigger path.

6.1.2 Electron Trigger Efficiencies

Trigger efficiencies for the electron sample were determined by choosing an event sample for which the trigger is as independent as possible of the electron. Within the dilepton sample itself, such a sample was found by using events which passed any of a multitude of muon triggers at Levels 1, 2, and 3.¹

Within these muon-triggered events, we look for isolated electron candidates that pass our identification cuts (see Section 4.1). Within a particular E_T bin, the trigger efficiency is determined by dividing the number of electron candidates which satisfy the selected electron trigger path by the total number of electron candidates within the E_T bin. These trigger efficiencies can be determined for particular triggers in a trigger level, or for the entire trigger path. Only the fit for the L1·L2·L3 trigger path was used in this analysis.

Figure 6.3 shows the resulting Level 1 electron trigger efficiency turn-on curve. The points are the efficiencies determined, and the uncertainties are calculated using binomial statistics, while the “uncertainty” in E_T is simply the bin width with the point centered within the bin. The binning was done such that roughly equivalent statistics were in each bin. The curve is the result of a fit to a normal frequency function:

$$\varepsilon_{trig}(E_T) = \varepsilon_{trig}^{max} \frac{1}{\sqrt{2\pi}} \int_{-\infty}^{E_T} e^{-(E_T - E_T^0)^2 / 2\sigma^2} dE_T \quad (6.1)$$

¹The Level 1 muon triggers which were accepted for this purpose were *CMX_10PT0_HTDC*, *CMU_CMP_6PT0_HTDC_**, *TWO_CMU_CMX_3PT3*, *TWO_CMU_3PT3_HTDC_BBC*, *TWO_CMU_3PT3_HTDC*, and *TWO_CMU_CMX_3PT3_BBC*. The Level 2 muon triggers which were accepted for this purpose were *CMUP_CFT_12.5DEG*, *CMNP_CFT_12.5DEG*, *CMUP_CFT_12.5DEG_MIN_ION*, *CMX_CMU_TWO_CFT_2.2*, *CMUP_CFT_7.5.5DEG*, *CMNP_CFT_12.5DEG_MIN_ION*, *TWO_CMU_CMX_ONE_CFT_3.4*, and *TWO_CMU_TWO_CFT_2.2*. The Level 3 muon triggers which were accepted for this purpose were *PSIC_DIMUON*, *PSIB_DIMUON_HIGHMASS*, *MUOA_CMU_AND_CMP_18*, *MUOB_CMU_ONLY_15*, *MUOB_CMP_ONLY_15*, *MUOC_CMU_CMP_6PT0*, *MUOB_CMU_CMP_8*, and *MUOB_CMU_CMP_15*.

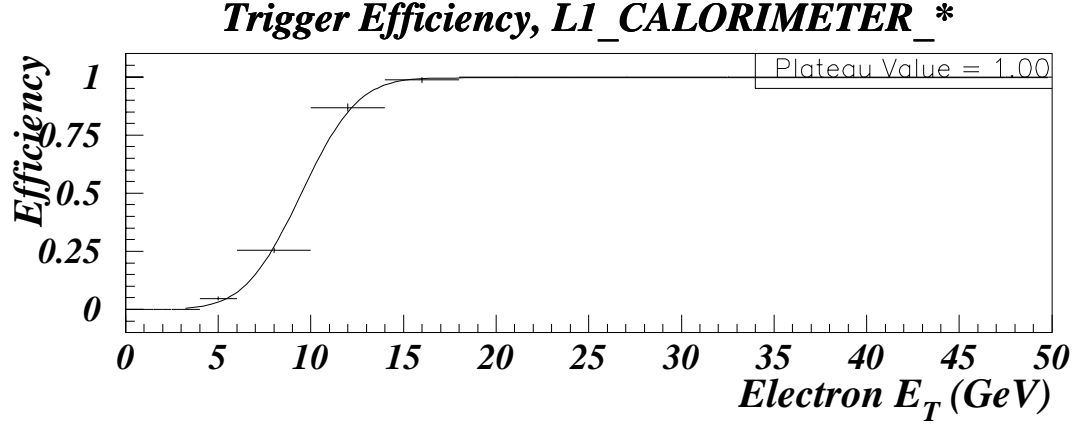


Figure 6.3: Electron Level 1 trigger efficiency turn-on curve. The points are the efficiencies determined, while the curve is the result of the normal frequency function fit.

where ε_{trig}^{max} is the plateau trigger efficiency, and E_T^0 is the E_T at which the curve reaches half-maximum.

Figure 6.4 (top) shows the trigger efficiency turn-on curve for the Level 2 electron trigger *CEM_8_CFT_7.5_XCES*. The dashed line shows the maximum possible efficiency due to the electron trigger prescale factor. The inefficiency can be ascribed to the average prescale factor of 1.15, as well as to inefficiencies in the CFT and XCES requirements. Figure 6.4 (bottom) shows the trigger efficiency turn-on curve for the Level 2 electron trigger *CEM_16_CFT_12*. The inefficiency can be ascribed to the inefficiency of the CFT requirement.

Figure 6.5 shows the trigger efficiency turn-on curve for the Level 3 electron trigger *ELEB_CEM_8_6*. The points could not be fit because of the abrupt threshold, which we attribute to poor statistics. At least part of the inefficiency at high E_T is due to the use of a wire- χ^2 cut at Level 3, which is not applied later during electron selection. This was verified by recalculating the trigger efficiency for electrons that passed the wire- χ^2 cut, for which we observed that the plateau efficiency increased

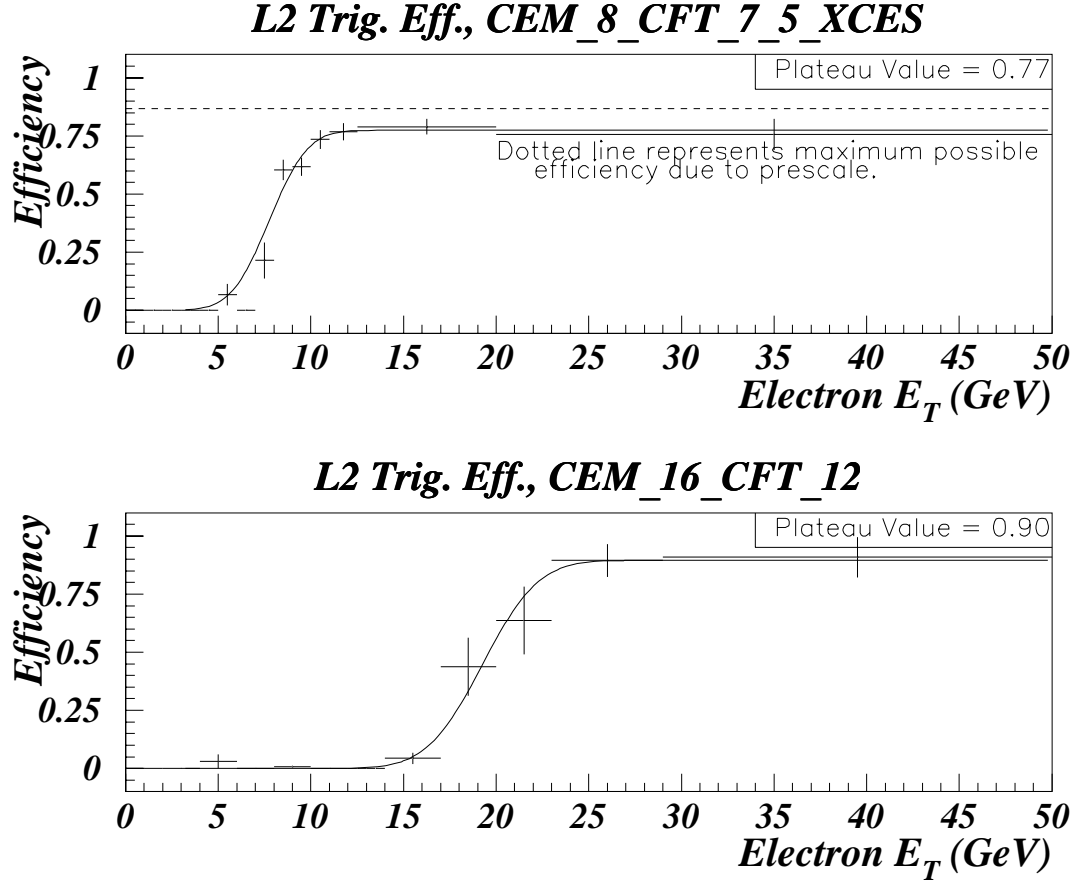


Figure 6.4: Electron Level 2 trigger efficiency turn-on curves. The top plot shows the L2 trigger efficiency for the prescaled trigger *CEM_8_CFT_7_5_XCES*. The bottom plot shows the L2 trigger efficiency of the *CEM_16_CFT_12* trigger. The efficiencies are measured for electrons which passed the Level 1 trigger. The points are the efficiencies determined, while the curve is the result of the normal frequency function fit.

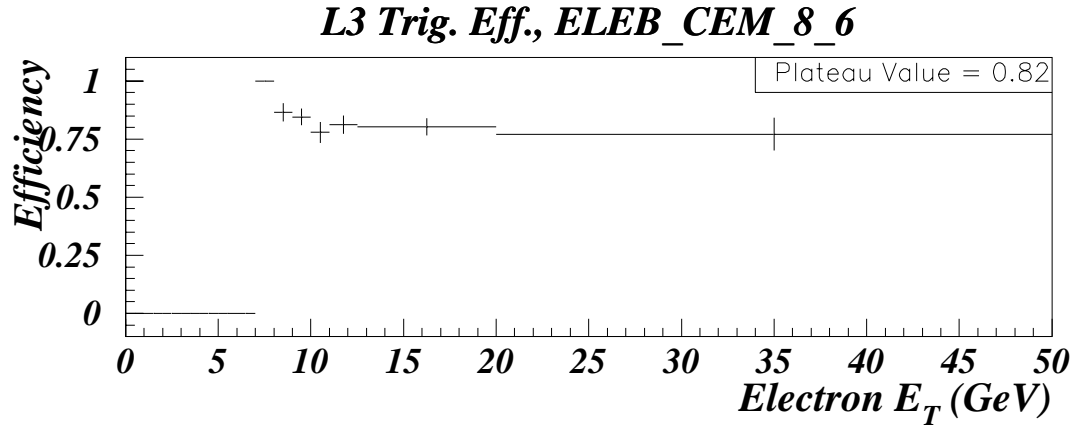


Figure 6.5: Electron Level 3 trigger efficiency plotted versus the electron E_T . The efficiency was determined for electrons which passed both Level 1 and Level 2 triggers.

by 12%.

Figure 6.6 shows the electron trigger efficiency turn-on curve for each combined L1·L2·L3 electron trigger path. The top plot is for the path including the prescaled trigger *CEM_8_CFT_7.5_XCES*, and the bottom plot is for the non-prescaled trigger path including *CEM_16_CFT_12*.

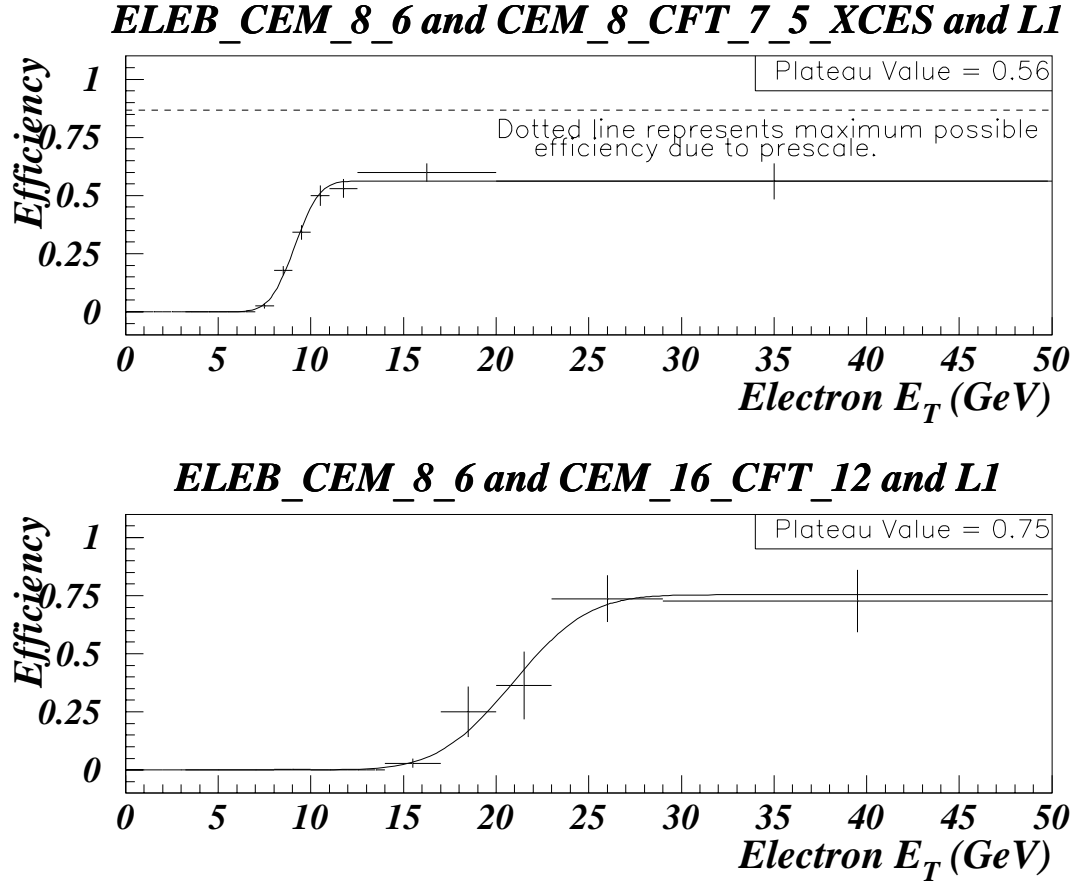


Figure 6.6: Electron combined L1.L2.L3 trigger efficiency turn-on curves. The top plot shows the efficiency for the trigger path which includes the prescaled Level 2 trigger *CEM_8_CFT_7_5_XCES*. The bottom plot shows the efficiency for the trigger path which includes the non-prescaled Level 2 trigger *CEM_16_CFT_12*.

6.1.3 Muon Trigger Efficiencies

Single muon trigger efficiencies were determined in the analogous way to electrons by choosing events from the SUSY dilepton sample^[7] which passed electron triggers at Levels 1, 2, and 3.²

Within these electron-triggered events, we look for isolated muon candidates that pass our identification cuts (see Section 4.2). Within a particular p_T bin, the trigger efficiency is determined by dividing the number of muon candidates which satisfy the selected muon trigger path by the total number of muon candidates within the p_T bin. These trigger efficiencies can be determined for particular triggers in a trigger level, or for the entire trigger path. Only the fits for the L1-L2 and L3 triggers were used in this analysis.

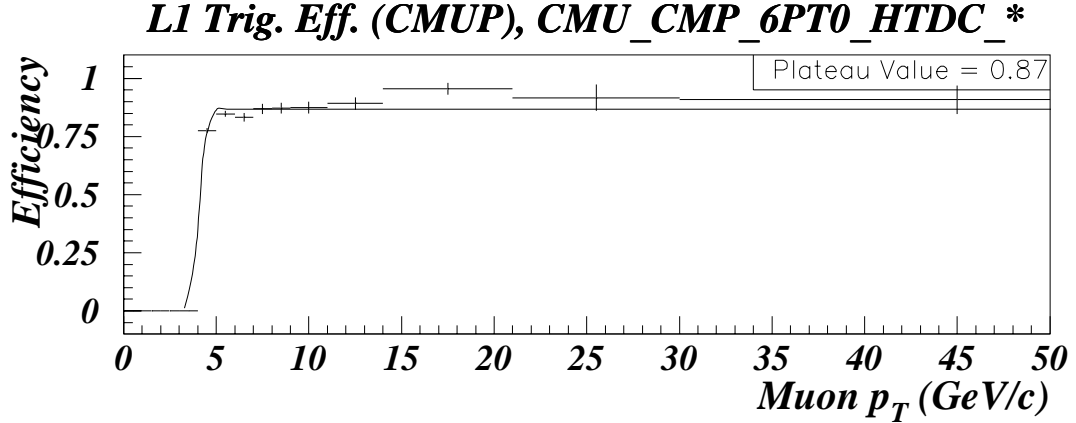


Figure 6.7: Level 1 muon trigger efficiency turn-on curve. The points are the efficiencies determined, while the curve is the result of the normal frequency function fit.

²The L1 electron triggers which were accepted for this purpose were *L1_DIELECTRON_4*, and *L1_CALORIMETER_**. The L2 electron triggers which were accepted for this purpose were *CEM_8_CFT_7.5*, *CEM_16_CFT_12*, *CEM_12_CFT_12_XCES*, *CEM_8_CFT_7.5_XCES*, *TWO_CEM_6_CFT_4.7*, *CEM_23_ISO_XCES*, *TWO_CEM_16_V1*, and *TWO_CEM_10_ISO*. The L3 electron triggers which were accepted for this purpose were *ELEB_CEM_18_LOOSE*, *ELEB_CEM_8_6*, *ELEB_NO_CFT*, and *ELEB_CEM_8*.

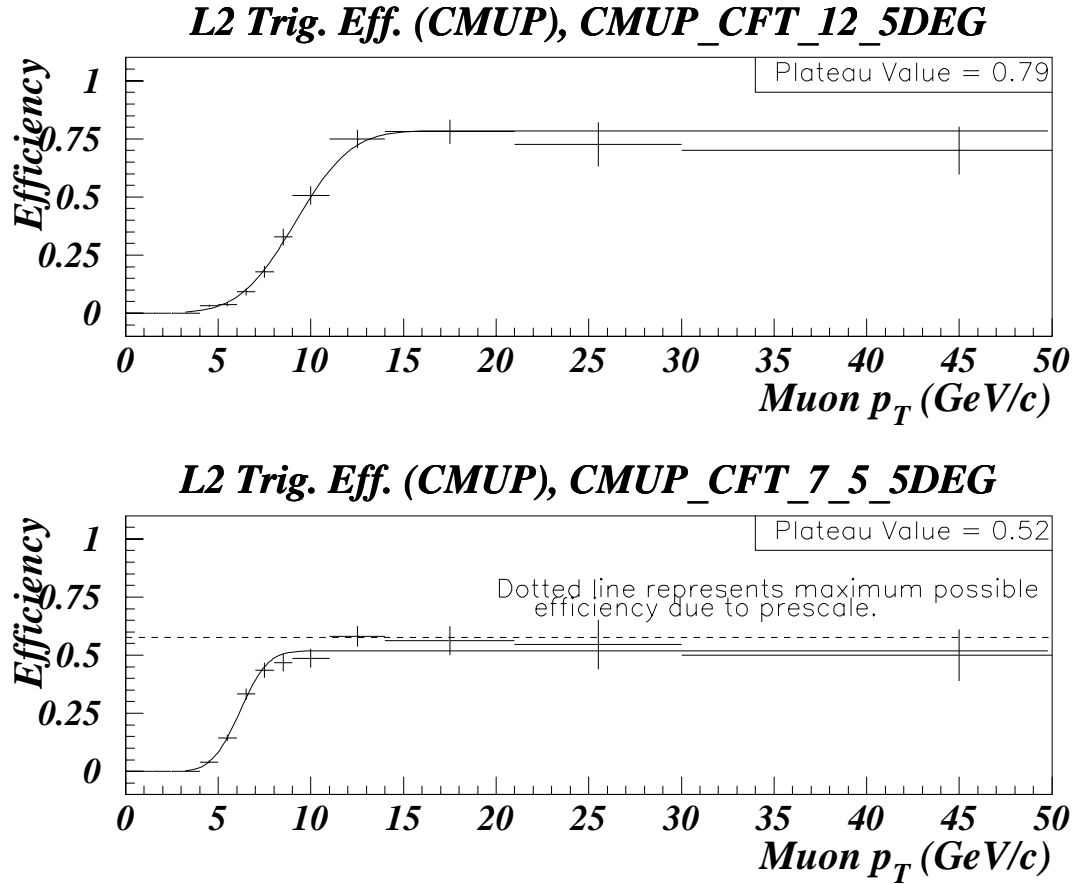


Figure 6.8: Level 2 muon trigger efficiency turn-on curves. The efficiency of each trigger was determined for muons that passed the Level 1 trigger.

Figure 6.7 shows the resulting Level 1 muon trigger efficiency turn-on curve. The points are the efficiencies determined, and the uncertainties are calculated using binomial statistics, while the “uncertainty” in E_T is simply the bin width with the point centered within the bin. The binning was done such that roughly equivalent statistics were in each bin. The curve is the result of a fit to a normal frequency function (Equation 6.1).

Figure 6.8 (top) shows the trigger efficiency turn-on curve for the Level 2 muon trigger *CMUP_CFT_12_5DEG*. Figure 6.8 (bottom) shows the trigger efficiency turn-on curve for the Level 2 muon trigger *CMUP_CFT_7_5_5DEG*. The dashed

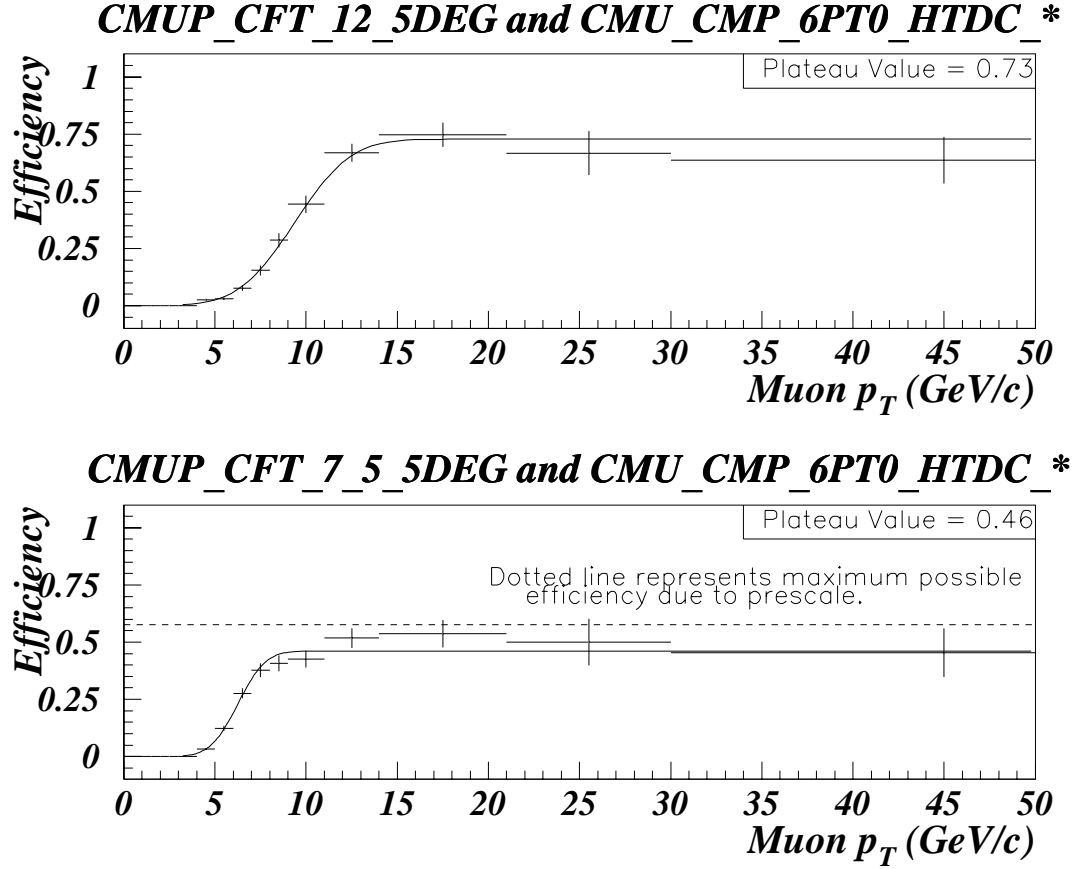


Figure 6.9: Level 2 muon trigger turn-on curves. The efficiency of each L1·L2 trigger path is measured for all isolated muons. The top plot shows the trigger efficiency for the path which includes the CMUP_CFT_12_5DEG L2 trigger. The bottom plot shows the same for the CMUP_CFT_7_5_5DEG L2 trigger. The dashed line shows the maximum possible efficiency due to the muon trigger prescale factor.

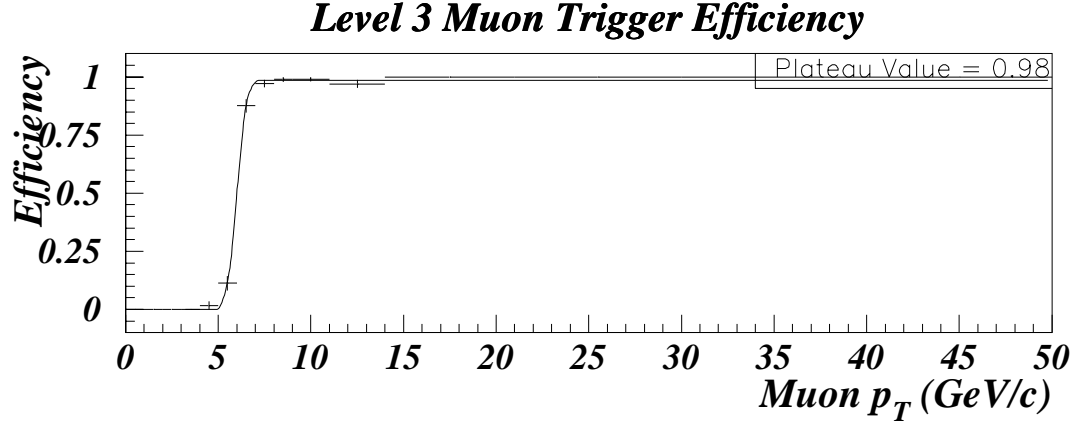


Figure 6.10: Level 3 muon trigger turn-on curve. The efficiency of the Level 3 trigger is measured for events which pass trigger Levels 1 and 2.

line shows the maximum possible efficiency due to the muon trigger prescale factor. The inefficiency of the *CMUP_CFT_7.5_5DEG* Level 2 trigger can be partially ascribed to the average prescale factor of 1.74, and the inefficiency of both Level 2 muon triggers can be ascribed to inefficiency in the CFT requirements.

Figure 6.9 shows the muon trigger efficiency turn-on curve for each combined L1-L2 muon trigger path. The top plot is for the path including the non-prescaled trigger *CMUP_CFT_12.5DEG*, and the bottom plot is for the prescaled trigger path including *CMUP_CFT_7.5_5DEG*.

Figure 6.10 shows the trigger efficiency turn-on curve for the Level 3 muon trigger (*MUOB_CMU_CMP_8*).

6.1.4 Trigger Efficiencies of Mass Bins

For electrons, the combined L1·L2·L3 trigger efficiency turn-on curve was fit to a normal frequency function. For muons, the combined L1·L2 trigger efficiency turn-on curve and the Level 3 trigger efficiency turn-on curve were fit separately. The uncertainties in the first parameter of the fit, i.e. the plateau efficiency level, were propagated into the statistical uncertainties in trigger acceptances.

Trigger efficiencies were determined for each Drell-Yan mass bin by simulating the trigger requirements on Monte Carlo events. The Monte Carlo events were required to pass acceptance cuts so that the trigger efficiencies were determined for the final event sample. The trigger simulation was done by generating a random number for each lepton and then testing it against the efficiency given by the turn-on curve at the p_T of the lepton. If the random number was less than the efficiency the lepton passed the trigger; otherwise, the lepton failed. Dielectron events were considered to be passed if one or both electrons passed either L1·L2·L3 electron trigger path. Dimuon events were considered to be passed if one or both muons passed either L1·L2 muon trigger path and the Level 3 muon trigger. The resulting trigger efficiencies can be found in Table 6.1.

6.2 Smearing and Detector Acceptance

Events which fall outside of the fiducial volume of the CDF detector, but which would otherwise have matched our selection criteria, are considered as part of an inefficiency to detect Drell-Yan events. Detector acceptance is the probability that a good Drell-Yan event is observed by our detector.

Detector acceptance was determined by “swimming” the Monte Carlo leptons

Table 6.1: Trigger efficiencies for each mass bin from the Monte Carlo.

Electrons					
Mass bin (GeV/c ²)	Accepted	Triggered	+1 σ	-1 σ	Trigger Eff.
11-15	660	187	199	180	0.28 ± 0.02
15-20	4518	1878	1955	1785	0.42 ± 0.02
20-30	6681	4426	4573	4262	0.66 ± 0.02
30-40	7940	6381	6544	6201	0.80 ± 0.02
40-50	9159	8141	8338	7936	0.89 ± 0.02
50-60	10357	9891	10067	9639	0.96 ± 0.02
60-70	11491	11192	11341	10973	0.97 ± 0.02
70-110	14655	14403	14560	14174	0.98 ± 0.01
110-150	17103	16861	17019	16562	0.99 ± 0.01
150-200	20143	19864	20058	19533	0.99 ± 0.01
200-600	24746	24379	24625	23986	0.99 ± 0.01
Muons					
Mass bin (GeV/c ²)	Accepted	Triggered	+1 σ	-1 σ	Trigger Eff.
11-15	966	382	392	371	0.40 ± 0.01
15-20	3766	1830	1901	1753	0.49 ± 0.02
20-30	5620	3164	3288	3064	0.56 ± 0.02
30-40	6659	4239	4353	4104	0.64 ± 0.02
40-50	7439	4764	4914	4611	0.64 ± 0.02
50-60	8419	5396	5574	5197	0.64 ± 0.02
60-70	9312	5981	6154	5796	0.64 ± 0.02
70-110	11635	7469	7687	7232	0.64 ± 0.02
110-150	13417	8556	8805	8268	0.64 ± 0.02
150-200	15597	10041	10308	9733	0.64 ± 0.02
200-600	18751	12055	12430	11673	0.64 ± 0.02

through the parameterized detector simulation described in Section 5.2. Transverse momenta and energy were smeared according to known tracking and calorimeter resolutions. In addition, the Monte Carlo leptons were allowed to radiate photons, some of which followed the lepton trajectory and were within the isolation cone and/or deposited energy in the calorimeter towers surrounding the lepton. Both of these effects, transverse momentum smearing and photon radiation, perturb the reconstructed dilepton in such a way that its observed invariant mass is in general

not equal to its generated mass.

6.2.1 Photon and Transverse Energy/Momentum Smearing

In order to correct for smearing between mass bins and the drop in invariant mass associated with photon radiation, a matrix of smeared/radiated bin versus generated bin was calculated. Table 6.2 shows the distribution of accepted events. Each column represents the mass bin in which an event was generated. Each row represents the mass bin in which the dilepton was observed after smearing and/or photon radiation caused a change in reconstructed mass. For instance, 660 dielectron events were generated in the 11-15 GeV mass range and accepted. Of these, 581 events remained in the same mass range, 2 events dropped to within 6-11 GeV, and 77 events were smeared into the 15-20 GeV mass bin. Typically more lepton pairs radiate down than smear up, but for events generated in the 11-15 GeV mass range, most of the events that would have been found in the 6-11 GeV mass range were lost due to kinematic acceptance.

Table 6.3 is identical to Table 6.2, but it has been normalized to the number of accepted lepton pairs in each *generated* mass range. Therefore, each complete column sums to unity, and the end result shows the percentage of events generated in a given mass bin that ended up in each smeared mass bin. The normalized matrix is shown in Table 6.3, and the inverted matrix is shown in Table 6.4. The corrected number of events with smearing removed is determined by reading across the inverted matrix. For example, the estimated number of dielectrons generated in the 11-15 GeV mass bin is:

$$N_{gen}^{11-15} = 1.147 \times N_{obs}^{11-15} - 0.080 \times N_{obs}^{15-20} + 0.004 \times N_{obs}^{20-30} - 0.001 \times N_{obs}^{40-50}$$

6.2.2 Detector Acceptance

Because the end result of the smearing correction is the number of generated dileptons in each mass bin, or for the purposes of this analysis, the number of dileptons that Drell-Yan production created in each mass bin, the correct acceptance is defined as the number of events that were generated in a given mass bin and were observed in any mass bin. The acceptance of dileptons in the rapidity range $|y| < 1$ is calculated for each mass bin using the following equation.

$$Acceptance \equiv \frac{\# \text{ of generated events passing fid, threshold and rapidity cuts}}{\# \text{ of generated events passing rapidity cut}} \quad (6.2)$$

As described in Chapter 5, 100,000 Monte Carlo events were generated in each Drell-Yan mass bin. The fraction of these events which fell within $|y| < 1$ varied with the dilepton mass. For example, of the 100,000 electron pairs generated in the 11-15 GeV mass range, only 20,272 were within the rapidity range $|y| < 1$ and therefore made up the denominator in the acceptance calculation. Table 6.5 summarizes the acceptance calculation.

6.3 Systematic Uncertainties of Detection Efficiency

We estimated two systematic uncertainties of the product $A \times \varepsilon_{trig}$. By scaling the Monte Carlo lepton pair p_T we were able to study what effect an intrinsically biased p_T would have on our trigger efficiency and acceptance. Although the Herwig Monte Carlo simulation was tuned to generate accurate p_T distributions versus vector boson mass, it may not have done so perfectly. In general, the Monte Carlo

Table 6.2: Smearing/Radiation Matrices from the Herwig Monte Carlo. Each column represents a mass bin that an event was generated in. Each row represents the mass bin that the event smeared or radiated into.

Electron Pair Mass Generated									
M_{obs}	11-15	15-20	20-30	30-40	40-50	50-60	60-70	70-110	110-150
6-11	2	1	2	1	0	1	5	1	0
11-15	581	281	8	1	4	7	1	1	0
15-20	77	4046	416	12	1	7	5	2	1
20-30	0	190	6148	541	33	26	13	8	4
30-40	0	0	107	7190	589	54	23	11	9
40-50	0	0	0	194	8265	741	65	20	16
50-60	0	0	0	0	266	9140	815	44	18
60-70	0	0	0	0	0	381	10014	76	19
70-110	0	0	0	0	0	0	550	14475	1183
110-150	0	0	0	0	0	0	0	17	15702
150-200	0	0	0	0	0	0	0	0	151
Muon Pair Mass Generated									
M_{obs}	11-15	15-20	20-30	30-40	40-50	50-60	60-70	70-110	110-150
6-11	3	0	2	4	1	1	2	0	0
11-15	954	75	8	2	1	2	0	0	1
15-20	9	3660	171	9	3	4	5	1	2
20-30	0	31	5412	311	20	23	11	7	3
30-40	0	0	27	6250	395	41	29	10	10
40-50	0	0	0	83	6861	483	41	20	15
50-60	0	0	0	0	158	7561	709	31	17
60-70	0	0	0	0	0	302	7960	59	20
70-110	0	0	0	0	0	0	554	11474	1547
110-150	0	0	0	0	0	0	0	32	11435
150-200	0	0	0	0	0	0	0	0	364

Table 6.3: Normalized Smearing/Radiation Matrices from the Herwig Monte Carlo. The matrices in Table 6.2 were normalized to the *generated* mass bin, so each column should sum to unity.

Electron Pair Mass Generated									
M_{obs}	11-15	15-20	20-30	30-40	40-50	50-60	60-70	70-110	110-150
11-15	.880	.062	.001	0	0	.001	0	0	0
15-20	.117	.896	.062	.002	0	.001	0	0	0
20-30	0	.042	.920	.068	.004	.003	.001	.001	0
30-40	0	0	.016	.906	.064	.005	.002	.001	.001
40-50	0	0	0	.024	.902	.072	.006	.001	.001
50-60	0	0	0	0	.029	.882	.071	.003	.001
60-70	0	0	0	0	0	.037	.871	.005	.001
70-110	0	0	0	0	0	0	.048	.988	.069
110-150	0	0	0	0	0	0	0	.001	.918
Muon Pair Mass Generated									
M_{obs}	11-15	15-20	20-30	30-40	40-50	50-60	60-70	70-110	110-150
11-15	.988	.020	.001	0	0	0	0	0	0
15-20	.009	.972	.030	.001	0	0	.001	0	0
20-30	0	.008	.963	.047	.003	.003	.001	.001	0
30-40	0	0	.005	.939	.053	.005	.003	.001	.001
40-50	0	0	0	.012	.922	.057	.004	.002	.001
50-60	0	0	0	0	.021	.898	.076	.003	.001
60-70	0	0	0	0	0	.036	.855	.005	.001
70-110	0	0	0	0	0	0	.059	.986	.115
110-150	0	0	0	0	0	0	0	.003	.852

Table 6.4: Normalized and Inverted Smearing/Radiation Matrices from the Herwig Monte Carlo. The matrices in Table 6.3 were inverted.

Electron Pair Mass Observed									
M_{gen}	11-15	15-20	20-30	30-40	40-50	50-60	60-70	70-110	110-150
11-15	1.147	-.080	.004	0	-.001	-.001	0	0	0
15-20	-.150	1.131	-.076	.004	0	-.001	0	0	0
20-30	.007	-.052	1.092	-.082	.002	-.003	-.001	-.001	0
30-40	0	.001	-.019	1.108	-.079	0	-.002	-.001	0
40-50	0	0	.001	-.030	1.113	-.090	0	-.001	-.001
50-60	0	0	0	.001	-.037	1.140	-.092	-.003	-.001
60-70	0	0	0	0	.002	-.048	1.152	-.006	-.001
70-110	0	0	0	0	0	.002	-.056	1.013	-.076
110-150	0	0	0	0	0	0	0	-.001	1.090
Muon Pair Mass Observed									
M_{gen}	11-15	15-20	20-30	30-40	40-50	50-60	60-70	70-110	110-150
11-15	1.013	-.021	-.001	0	0	0	0	0	0
15-20	-.010	1.029	-.033	0	0	0	-.001	0	0
20-30	0	-.009	1.039	-.052	0	-.003	-.001	-.001	0
30-40	0	0	-.005	1.067	-.061	-.002	-.003	-.001	-.001
40-50	0	0	0	-.014	1.087	-.069	.001	-.002	-.001
50-60	0	0	0	0	-.026	1.119	-.099	-.002	-.001
60-70	0	0	0	0	.001	-.047	1.174	-.006	-.001
70-110	0	0	0	0	0	.003	-.071	1.015	-.138
110-150	0	0	0	0	0	0	0	-.003	1.179

Table 6.5: Acceptance Data from the Herwig Monte Carlo. Only statistical errors are shown.

Electrons, 100,000 MC events each bin			
Mass bin (GeV/c ²)	Total, $ y < 1$	Passed cuts	Acceptance
11-15	20272	660	0.033 ± 0.001
15-20	22777	4518	0.198 ± 0.003
20-30	26203	6681	0.255 ± 0.003
30-40	30208	7940	0.263 ± 0.003
40-50	34619	9159	0.265 ± 0.002
50-60	38255	10357	0.271 ± 0.002
60-70	42370	11491	0.271 ± 0.002
70-110	52390	14655	0.280 ± 0.002
110-150	59711	17103	0.286 ± 0.002
150-200	68909	20143	0.292 ± 0.002
200-600	79732	24753	0.310 ± 0.002
Muons, 100,000 MC events each bin			
Mass bin (GeV/c ²)	Total, $ y < 1$	Passed cuts	Acceptance
11-15	20483	966	0.047 ± 0.001
15-20	23099	3766	0.163 ± 0.002
20-30	26398	5620	0.213 ± 0.003
30-40	30395	6659	0.219 ± 0.002
40-50	34457	7439	0.216 ± 0.002
50-60	37904	8419	0.222 ± 0.002
60-70	41693	9312	0.223 ± 0.002
70-110	51015	11635	0.228 ± 0.002
110-150	57330	13417	0.234 ± 0.002
150-200	65202	15597	0.239 ± 0.002
200-600	73988	18850	0.255 ± 0.002

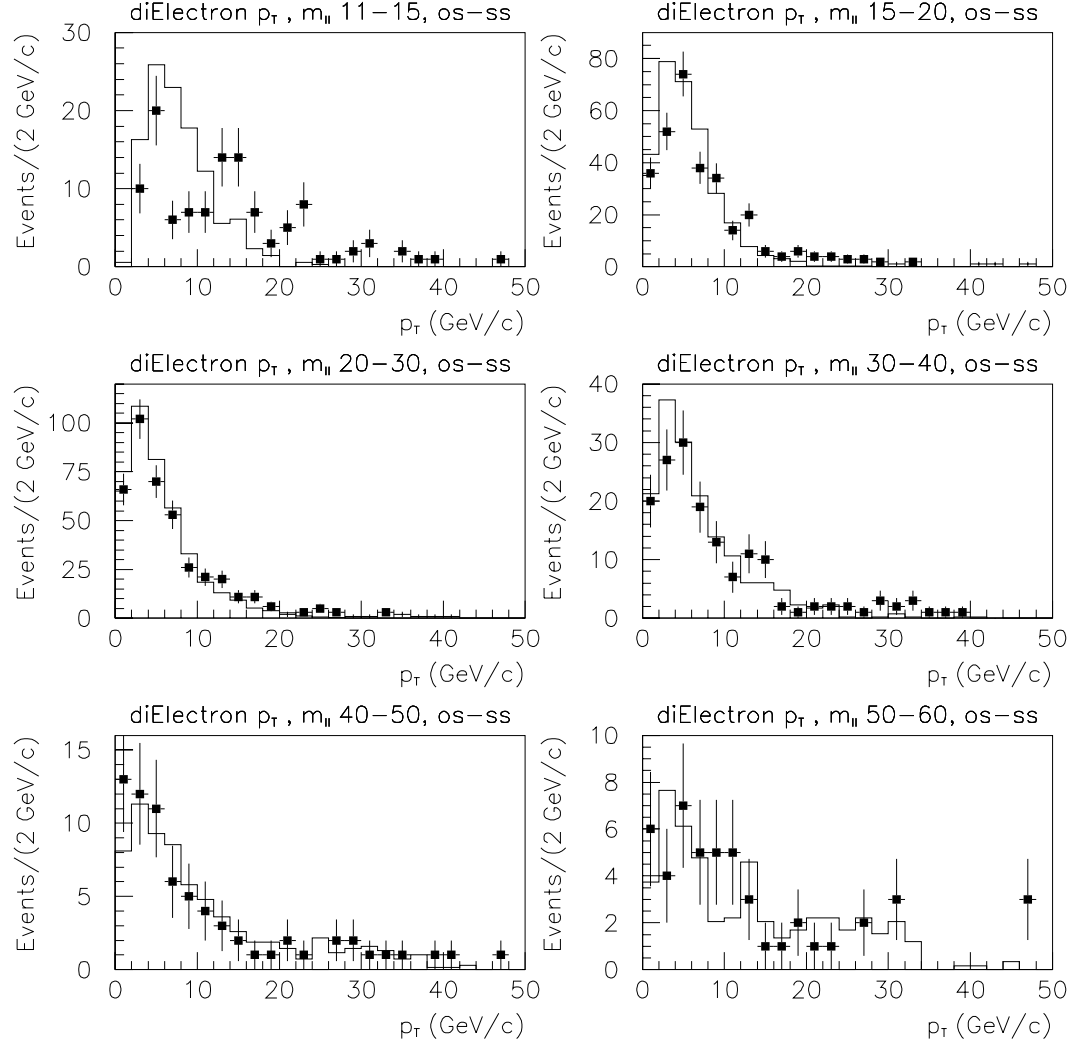


Figure 6.11: Monte Carlo simulated transverse momentum distributions for dielectrons. The points represent the CDF Run 1B dielectron data, while the solid histograms represent the Herwig Monte Carlo simulation. The distributions are shown for the following mass bins: 11-15, 15-20, 20-30, 30-40, 40-50, and 50-60 GeV/c^2 .

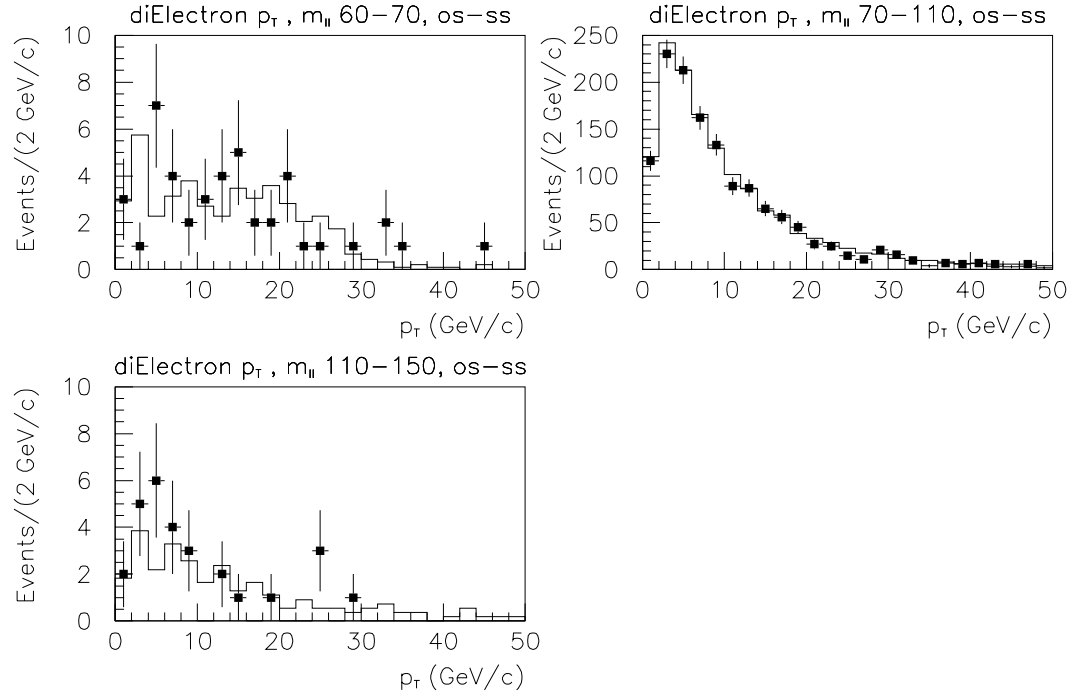


Figure 6.12: Monte Carlo simulated transverse momentum distributions for dielectrons. The points represent the CDF Run 1B dielectron data, while the solid histograms represent the Herwig Monte Carlo simulation. The distributions are shown for the following mass bins: 60-70, 70-110, 110-150, 150-200, and 200-600 GeV/c^2 .

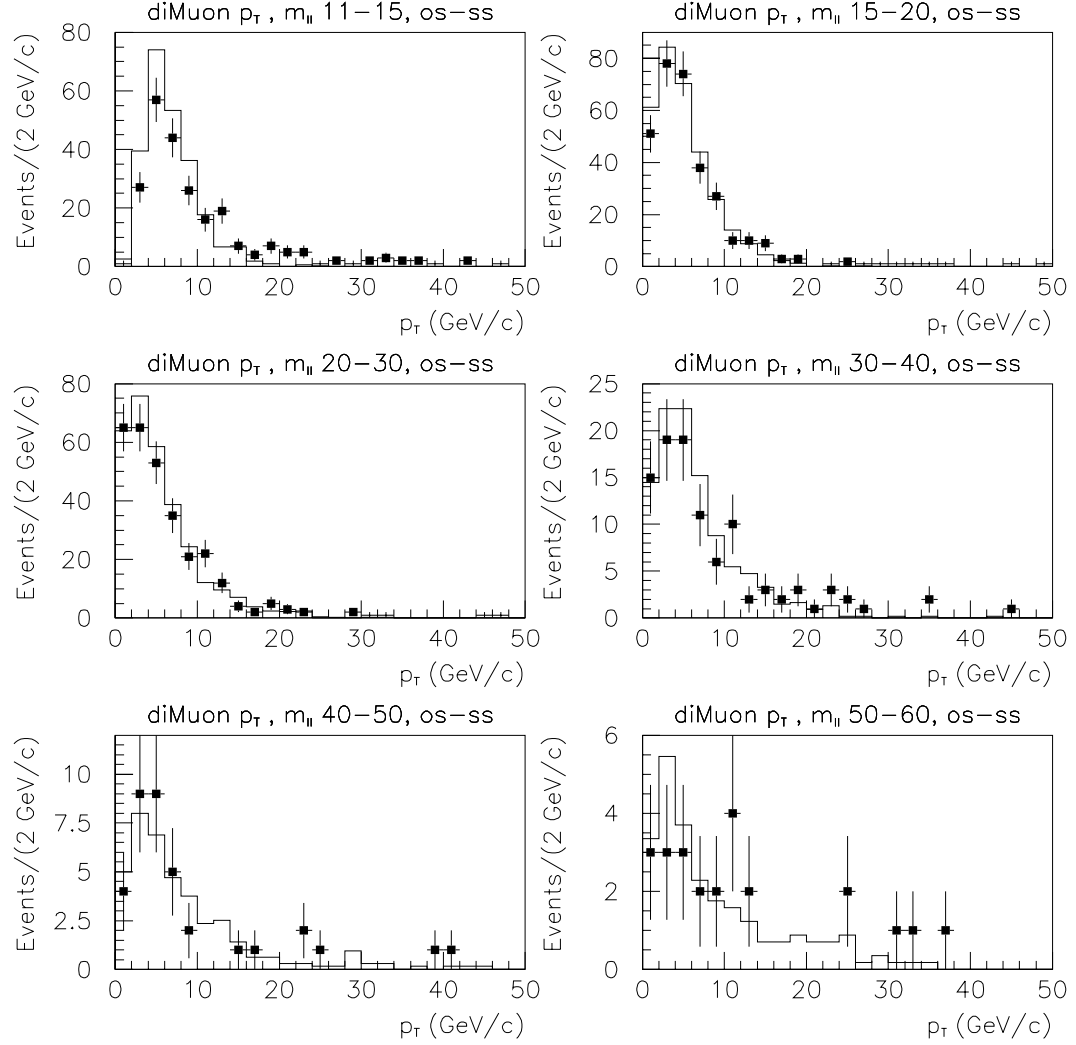


Figure 6.13: Monte Carlo simulated transverse momentum distributions for dimuons. The points represent the CDF Run 1B dimuon data, while the solid histograms represent the Herwig Monte Carlo simulation. The distributions are shown for the following mass bins: 11-15, 15-20, 20-30, 30-40, 40-50, and 50-60 GeV/c^2 .

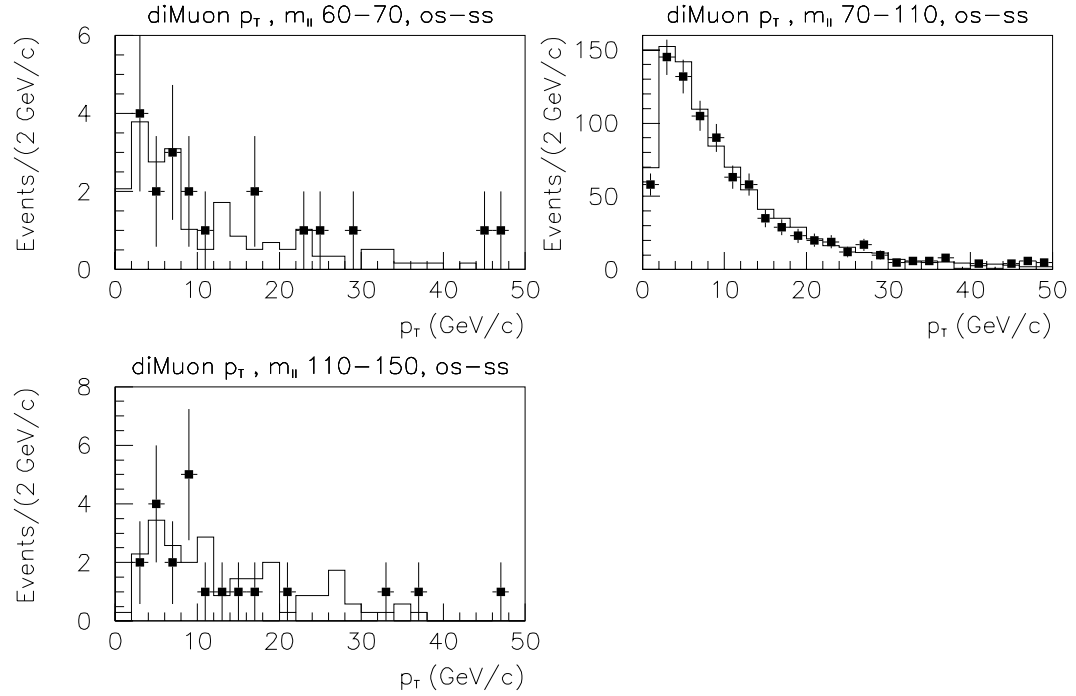


Figure 6.14: Monte Carlo simulated transverse momentum distributions for dimuons. The points represent the CDF Run 1B dimuon data, while the solid histograms represent the Herwig Monte Carlo simulation. The distributions are shown for the following mass bins: 60-70, 70-110, 110-150, 150-200, and 200-600 GeV/c^2 .

and data p_T distributions matched well without any scaling (see Figures 6.11, 6.12, 6.13, and 6.14), and we assigned an uncertainty based on a reasonable amount of scaling above and below some optimum value.

We also allowed for the possibility that our choice of structure function (MRS-R2) for the Monte Carlo was not perfect. Different structure functions can in some cases yield very different lepton pair rapidity distributions. As a result, the CDF detector geometry with separate – sometimes inactive or inefficient – chambers covering different ranges in η , may produce a significantly different detector acceptance.

6.3.1 Scaling of the Monte Carlo Lepton Pair p_T

Both the trigger efficiencies and acceptance calculations are heavily dependent on the p_T distributions of the Monte Carlo samples at the lowest masses. We therefore must account for the uncertainty in our measurement due to imprecise Monte Carlo boson transverse momenta distributions. We assume that differences between the data and Monte Carlo distributions can be accounted for with an overall scaling of the Monte Carlo lepton pair p_T .

The HERWIG Monte Carlo samples discussed in Chapter 5 were stored in ntuple form before any detector simulation was performed. The same ntuples were used for this calculation, and a step was added to our Monte Carlo routine between event generation and the detector and trigger simulations. The lepton pair p_T was relativistically boosted to zero, thereby shifting the frame of reference to the rest frame of the boson while insuring that the mass of the lepton pair remained invariant. The p_T was then scaled by some value (e.g. 110%) and boosted back along with the original p_z of the lepton pair. After this, the detector and trigger simulations were run on the events so that the acceptance and trigger efficiencies

could be determined.

This was done for several scaling values, from about 70% to 170%. For each scaling value the Monte Carlo p_T distributions were compared to the unchanged data p_T distributions, and a χ^2 was calculated. At low invariant mass the individual lepton p_T distributions are especially important to the trigger efficiency calculation. Therefore, our χ^2 was defined as the sum of the χ^2 s for three data-Monte Carlo comparisons: lepton 1 p_T , lepton 2 p_T , and lepton pair p_T .

For different invariant masses, the scale at which the minimum χ^2 occurred was identified. For the lowest masses ($11 < M_{ll} < 15$ GeV) the scale was rather high: 132% for electrons, and 114% for muons. We attribute the high scaling value partially to the high amount of heavy flavor background in this mass range (approximately 15% as seen in Chapter 7), to the lack of precision in the turn-on region of the trigger efficiencies, and to low statistics, especially for the electrons. In other mass ranges, the minimum χ^2 was usually found at a scaling value that was only a few percent higher than 100% (i.e. not scaled). Backgrounds, which are largely sequential lepton decays are generally reconstructed as a boson with high p_T and low mass.

The commonly used method of determining an uncertainty is to change the χ^2 by one unit and observe the change in the relevant quantity. In this case however, the three distributions that make the χ^2 are highly correlated, and the correct method is not obvious. We conservatively used the scaling values at which the difference between the data and Monte Carlo p_T distributions was about 4σ . Figures 6.15 through 6.24 justify this approach by showing that the p_T distributions are significantly changed at the 4σ scaling values. Also important is the fact that, except at low masses where there is significant unsubtracted background in the data

distributions, the change in χ^2 from the minimum point overlaps with the 100% (non-scaled) point. The scaling values are given in Table 6.6. We use the result of the 4σ difference between the Monte Carlo and data p_T distributions to determine the 1σ uncertainty on the cross-sections.

The trigger efficiency and acceptance were calculated for the minimum χ^2 and plus/minus 4σ scaling values, and the percent difference was taken to be the systematic uncertainty due to p_T scaling. Table 6.7 summarizes the calculation and the results for each mass bin.

Table 6.6: Scaling values for p_T scaling uncertainty estimate.

Electrons			
Mass bin	Min. χ^2	-4σ	$+4\sigma$
11-15	1.32	1.17	1.47
15-20	1.16	1.07	1.37
20-30	1.06	0.97	1.30
> 30	1.00	0.85	1.15
Muons			
Mass bin	Min. χ^2	-4σ	$+4\sigma$
11-15	1.14	1.05	1.28
15-20	1.13	0.96	1.30
20-30	1.10	0.90	1.32
> 30	1.06	0.85	1.32

Table 6.7: Systematic uncertainty of $A \times \varepsilon_{trig}$ from scaling the Monte Carlo lepton pair p_T . The second column lists the value of $A \times \varepsilon_{trig}$ when the p_T scaling minimizes the χ^2 of the comparison between data and the Monte Carlo. The columns labelled ' -1σ ' and ' $+1\sigma$ ' list $A \times \varepsilon_{trig}$ when the p_T scaling changed the distributions by $\pm 4\sigma$. The maximum difference is the systematic uncertainty.

Electrons						
Mass bin	$(A \times \varepsilon_{trig}) _{\text{Min}\chi^2}$	-1σ	% Diff.	$+1\sigma$	% Diff.	Max. % Diff.
11-15	0.015	0.012	-20.1	0.019	21.7	21.7
15-20	0.089	0.086	-2.5	0.097	8.8	8.8
20-30	0.174	0.177	1.4	0.178	2.4	2.4
30-40	0.215	0.210	-2.6	0.214	-0.7	2.6
>40	0.274	0.273	-0.1	0.274	0.2	0.2
Muons						
Mass bin	$(A \times \varepsilon_{trig}) _{\text{Min}\chi^2}$	-1σ	% Diff.	$+1\sigma$	% Diff.	Ave. % Diff.
11-15	0.021	0.019	-8.2	0.025	19.1	19.1
15-20	0.086	0.084	-2.1	0.087	1.1	2.1
20-30	0.120	0.124	3.5	0.125	4.4	4.4
30-40	0.143	0.143	-0.3	0.138	-3.6	3.6
>40	0.147	0.147	-0.3	0.147	-0.1	0.3

6.3.2 Varying the Monte Carlo Structure Function

After an initial test of several Monte Carlo structure functions, it was found that Monte Carlo generated with the MRSA structure function set produced the most significant difference in $A \times \varepsilon_{trig}$ from what was presented above using the MRS-R2 structure function set. The HERWIG Monte Carlo samples described in Section 5.1 were generated again using MRSA in place of MRS-R2 for the nucleon structure function sets, with no other changes. The acceptance and trigger efficiencies were then calculated with the new samples using the methods described in Sections 6.1 and 6.2, and the percent difference was taken as the systematic uncertainty of $A \times \varepsilon_{trig}$.

Table 6.8 lists the value of $A \times \varepsilon_{trig}$ for the MRS-R2 structure function set (same

as above) along with the value of $A \times \varepsilon_{trig}$ for the MRSA structure function set and the uncertainty.

Table 6.8: Systematic uncertainty of $A \times \varepsilon_{trig}$ from varying the Monte Carlo nucleon structure functions. There were 100,000 Monte Carlo events generated in each mass bin, so the statistical uncertainties of the results for each structure function set are small enough to be ignored.

Electrons			
Mass bin	MRS-R2 $A \times \varepsilon_{trig}$	MRSA $A \times \varepsilon_{trig}$	% Diff
11-15	0.0092	0.0086	-7.1
15-20	0.082	0.075	-8.9
20-30	0.169	0.172	1.9
30-40	0.211	0.213	0.7
40-50	0.235	0.245	4.1
50-60	0.259	0.255	-1.5
60-70	0.264	0.264	0.1
70-110	0.275	0.271	-1.6
110-150	0.282	0.278	-1.5
Muons			
Mass bin	MRS-R2 $A \times \varepsilon_{trig}$	MRSA $A \times \varepsilon_{trig}$	% Diff
11-15	0.019	0.018	-4.8
15-20	0.079	0.077	-3.0
20-30	0.120	0.121	1.3
30-40	0.139	0.139	-0.1
40-50	0.138	0.140	1.5
50-60	0.142	0.140	-1.4
60-70	0.143	0.140	-2.5
70-110	0.146	0.143	-2.1
110-150	0.149	0.148	-1.0

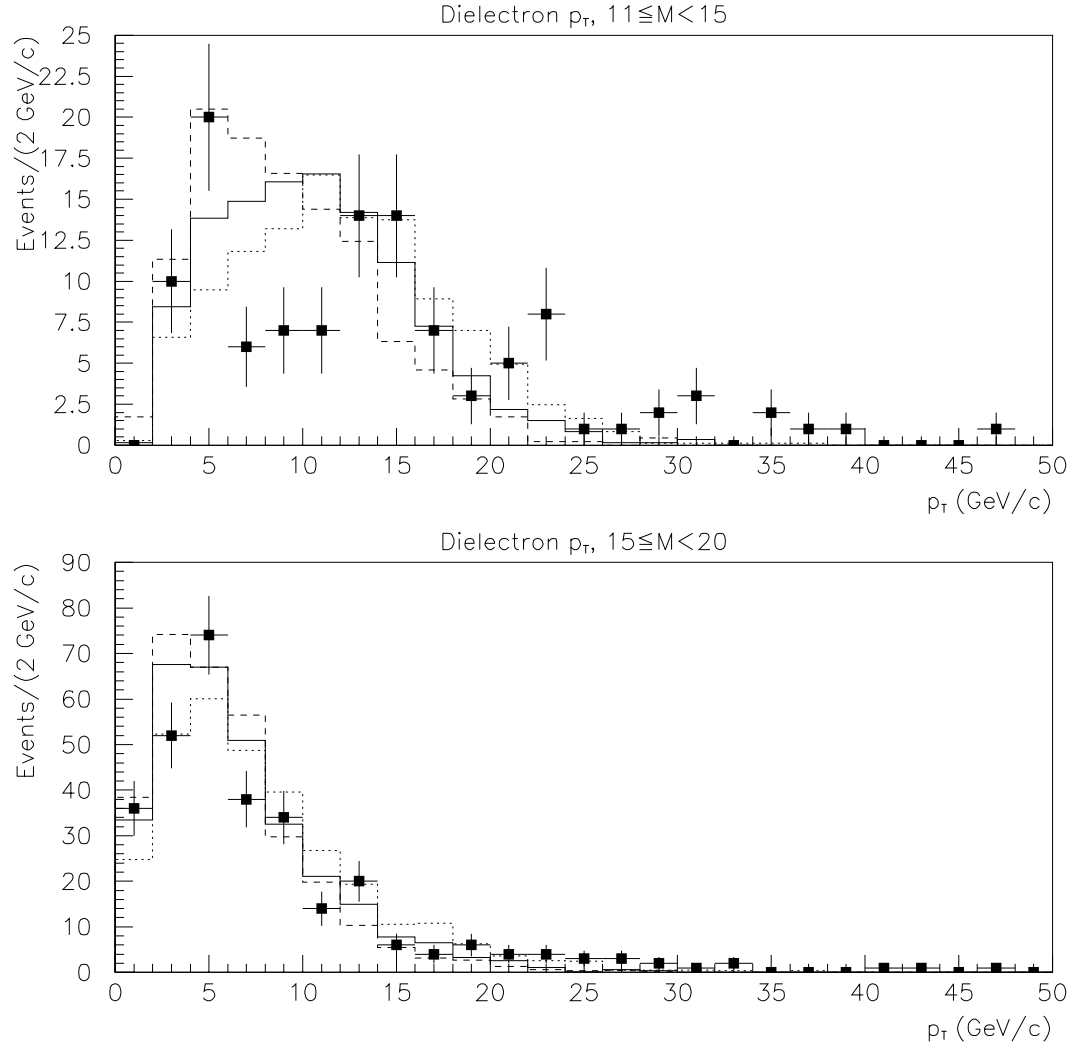


Figure 6.15: p_T distributions for data (points) and Monte Carlo with minimized χ^2 (solid line) and $\pm 4\sigma$ (dashed lines) scaling values on the Monte Carlo p_T .

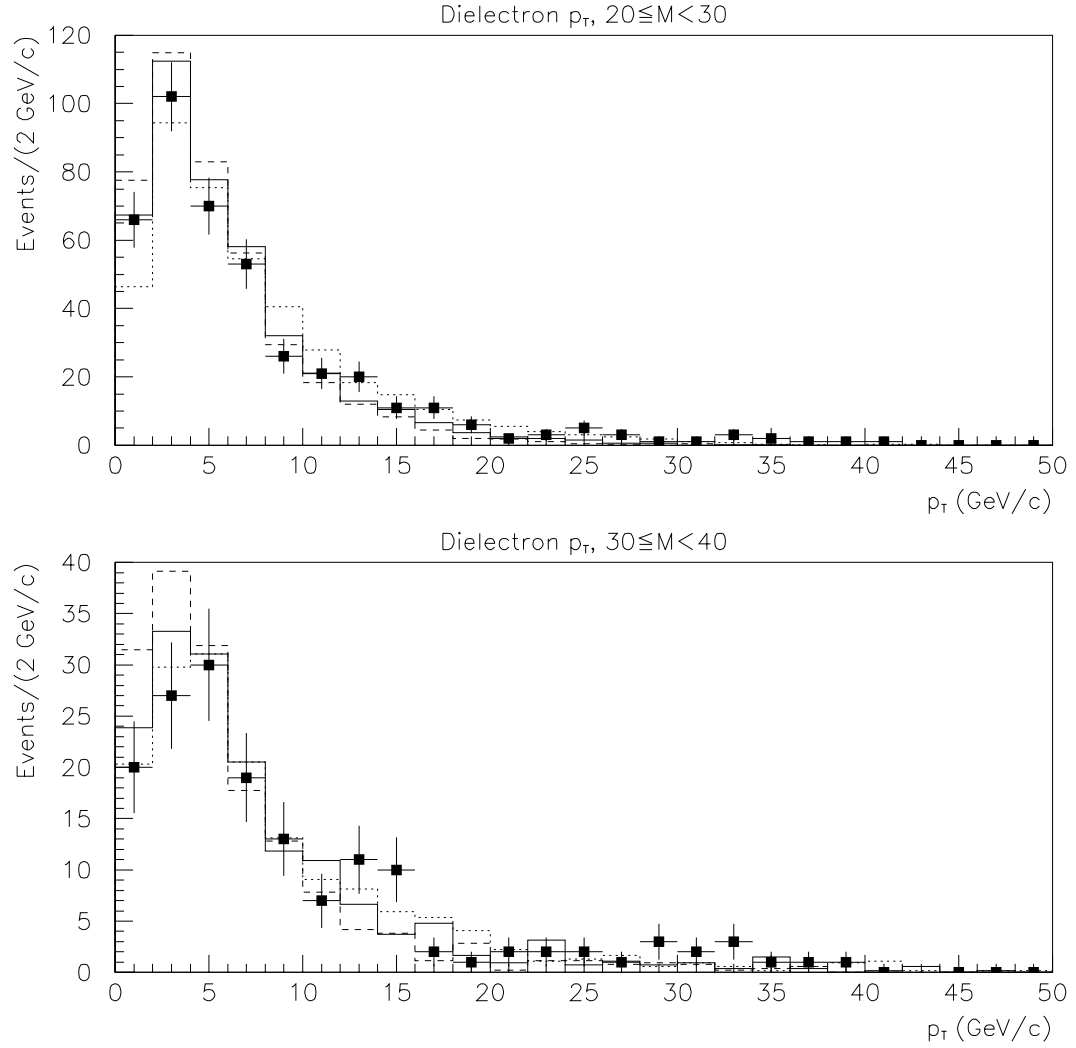


Figure 6.16: p_T distributions for data (points) and Monte Carlo with minimized χ^2 (solid line) and $\pm 4\sigma$ (dashed lines) scaling values on the Monte Carlo p_T .

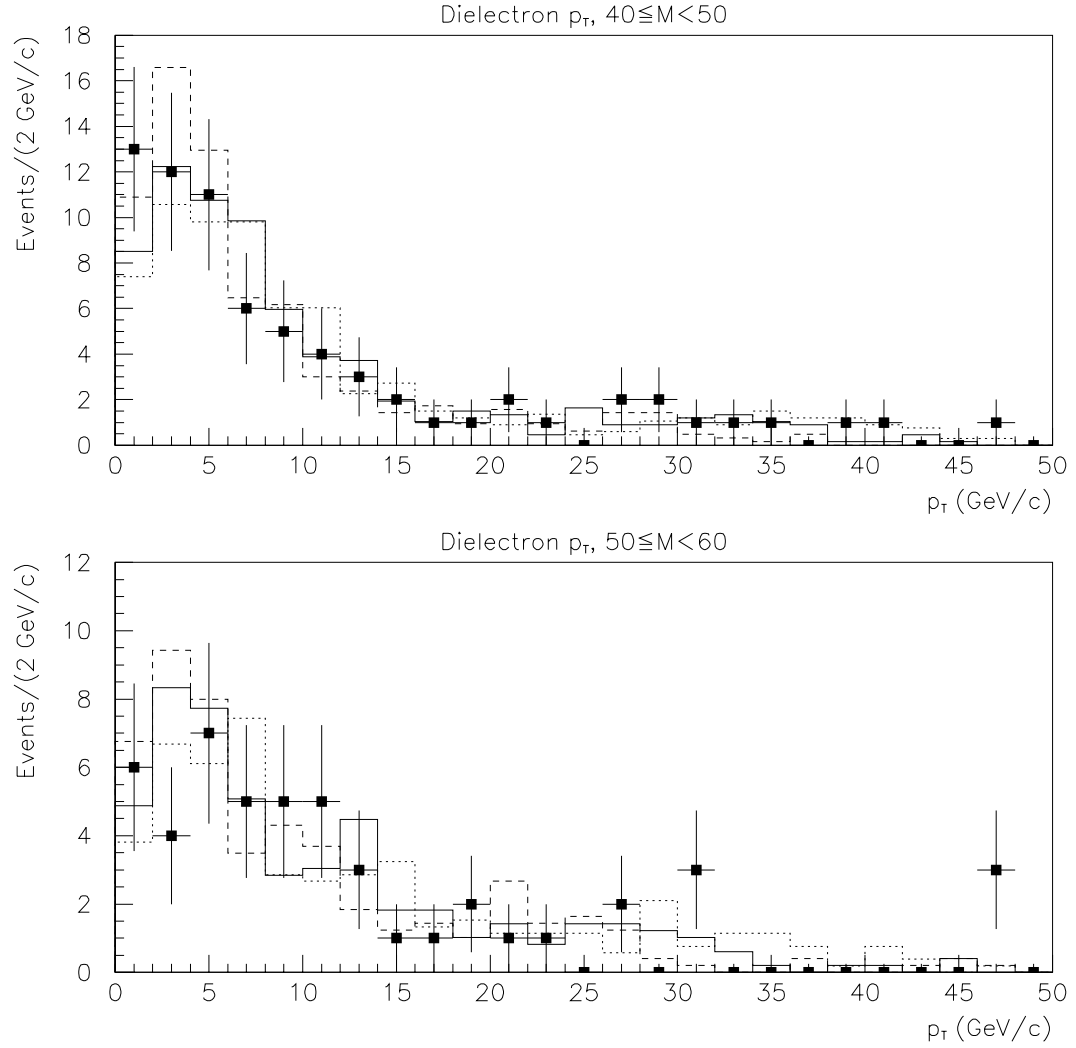


Figure 6.17: p_T distributions for data (points) and Monte Carlo with minimized χ^2 (solid line) and $\pm 4\sigma$ (dashed lines) scaling values on the Monte Carlo p_T .

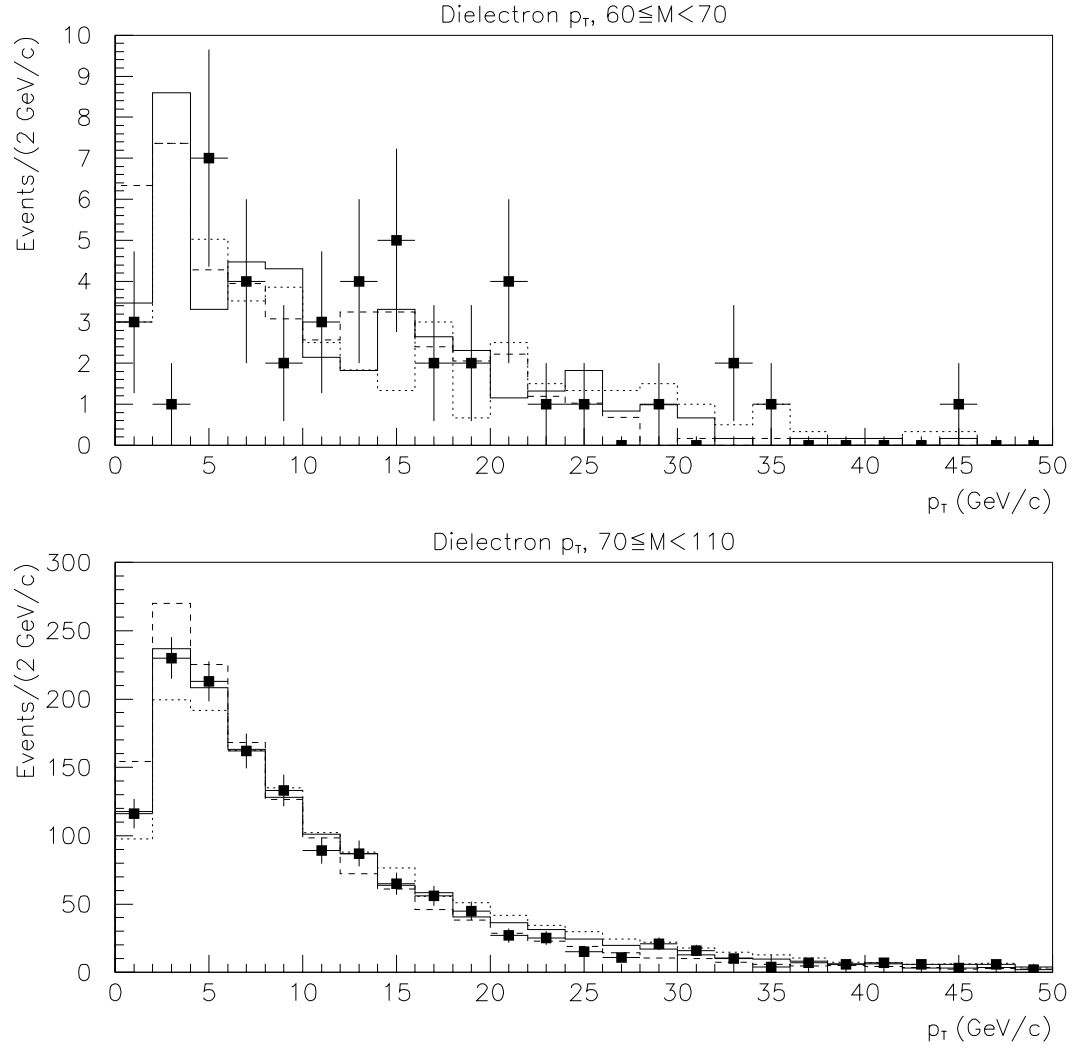


Figure 6.18: p_T distributions for data (points) and Monte Carlo with minimized χ^2 (solid line) and $\pm 4\sigma$ (dashed lines) scaling values on the Monte Carlo p_T .

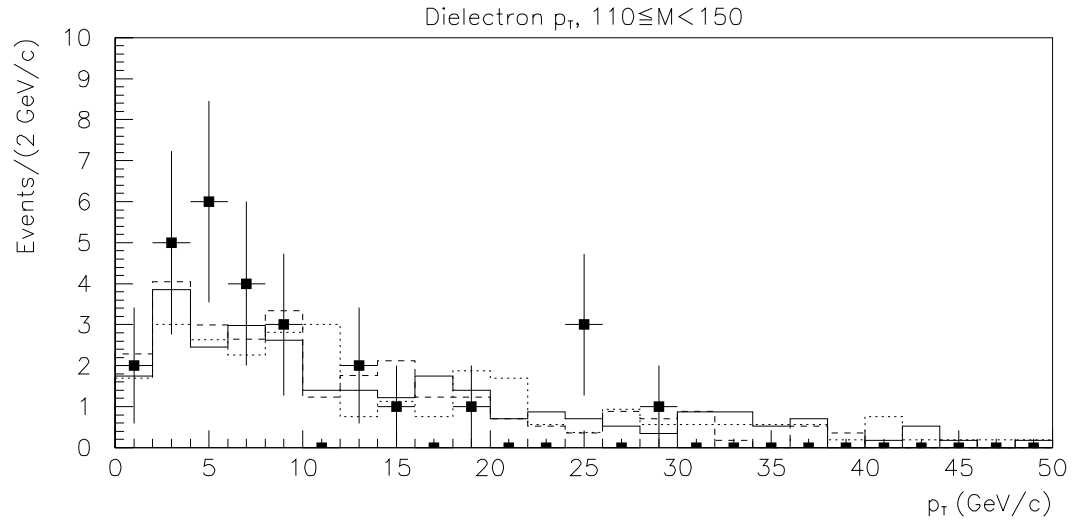


Figure 6.19: p_T distributions for data (points) and Monte Carlo with minimized χ^2 (solid line) and $\pm 4\sigma$ (dashed lines) scaling values on the Monte Carlo p_T .

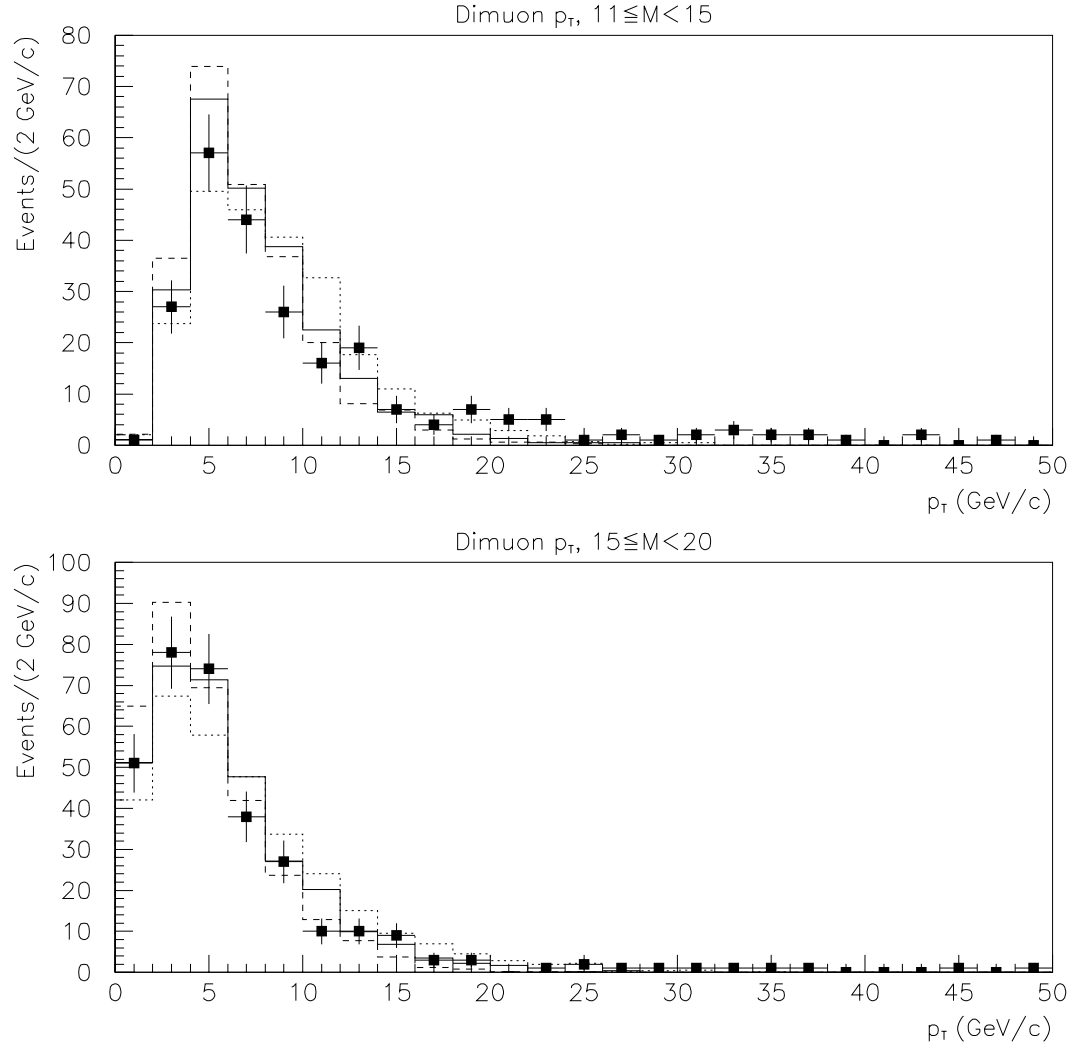


Figure 6.20: p_T distributions for data (points) and Monte Carlo with minimized χ^2 (solid line) and $\pm 4\sigma$ (dashed lines) scaling values on the Monte Carlo p_T .

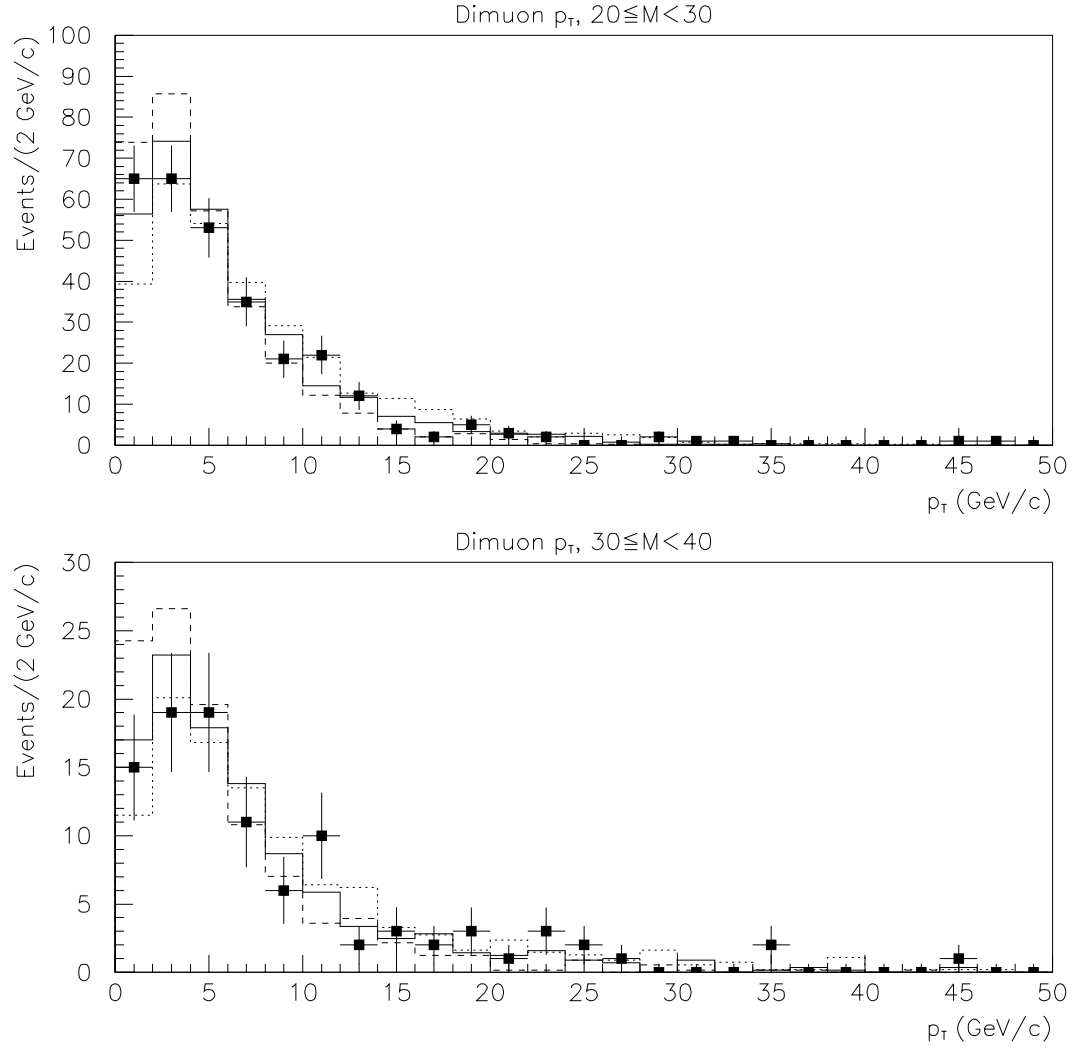


Figure 6.21: p_T distributions for data (points) and Monte Carlo with minimized χ^2 (solid line) and $\pm 4\sigma$ (dashed lines) scaling values on the Monte Carlo p_T .

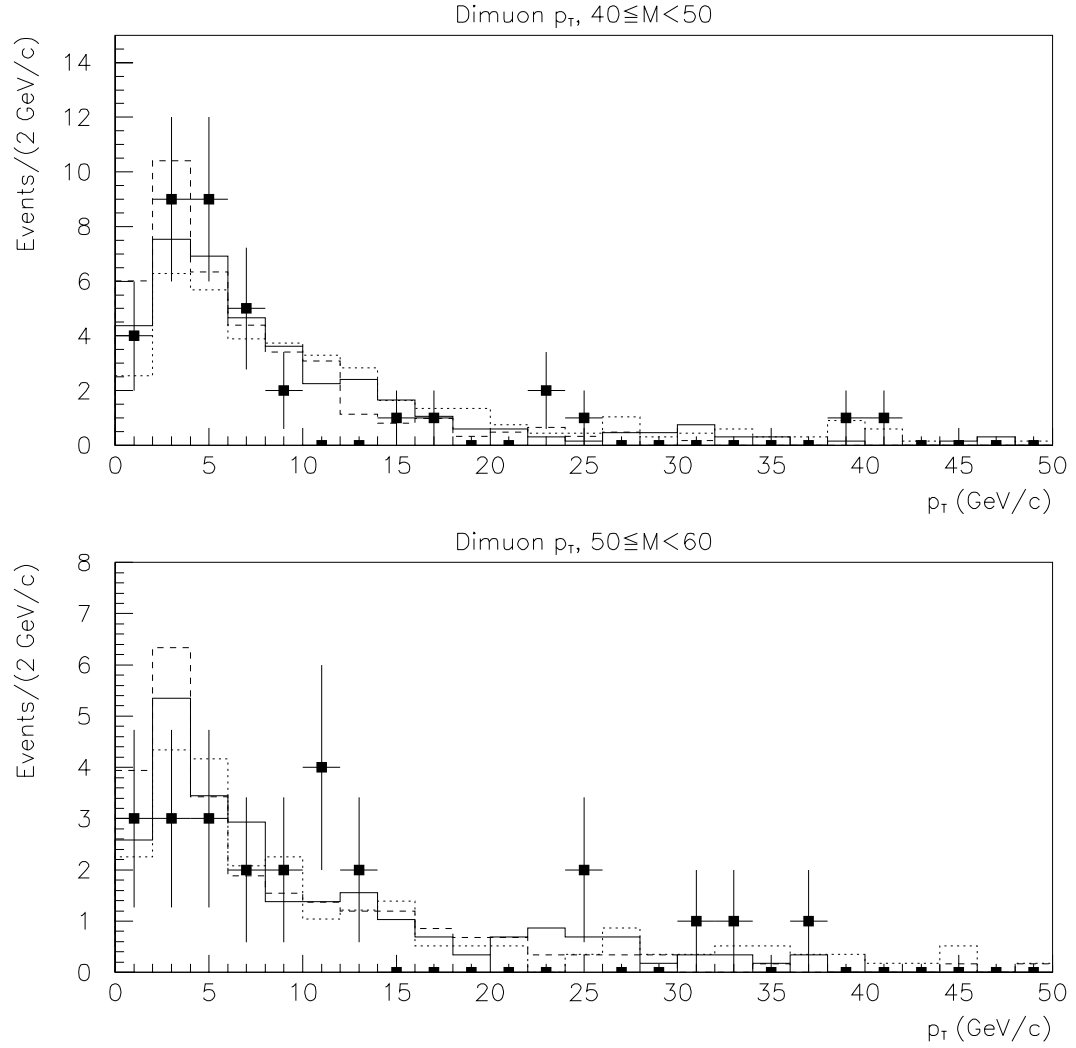


Figure 6.22: p_T distributions for data (points) and Monte Carlo with minimized χ^2 (solid line) and $\pm 4\sigma$ (dashed lines) scaling values on the Monte Carlo p_T .

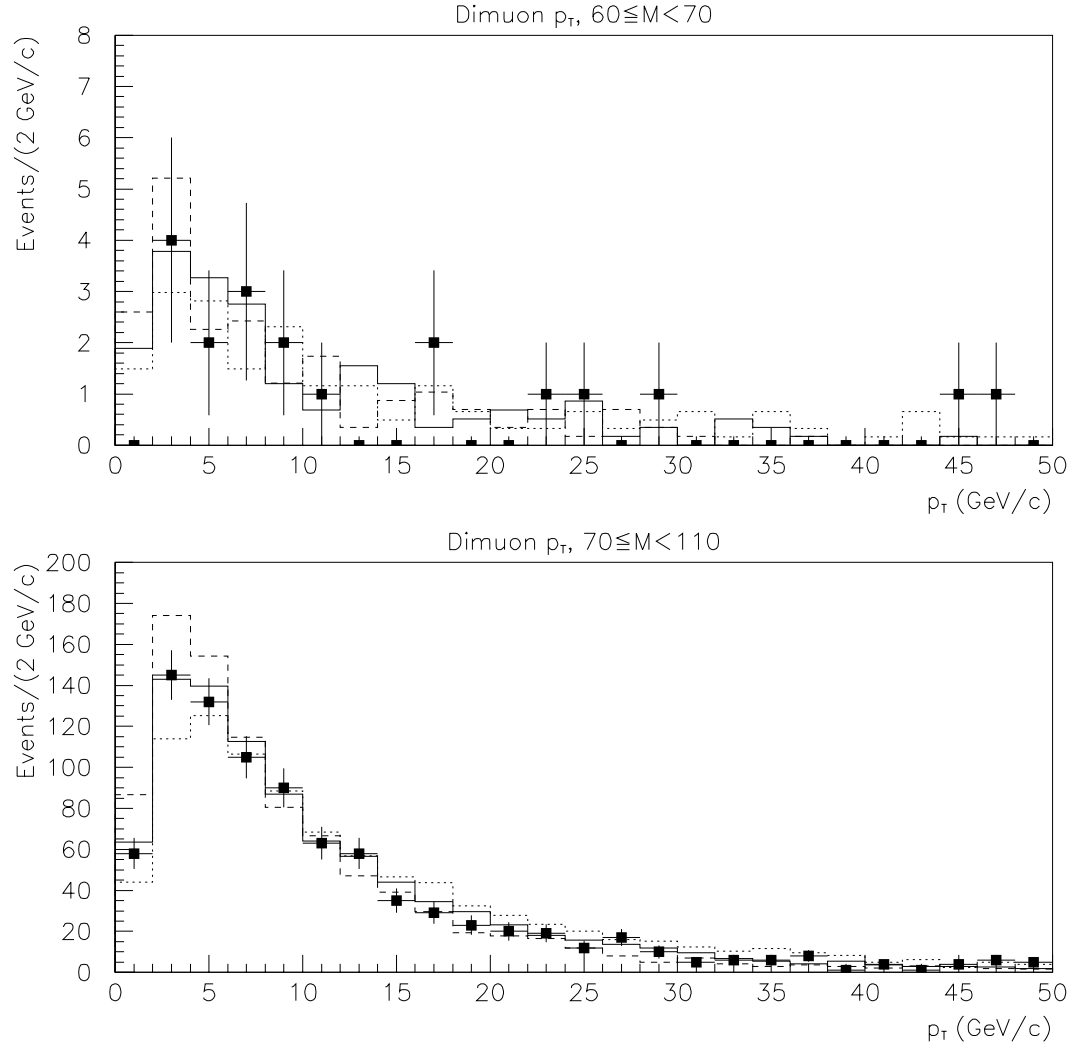


Figure 6.23: p_T distributions for data (points) and Monte Carlo with minimized χ^2 (solid line) and $\pm 4\sigma$ (dashed lines) scaling values on the Monte Carlo p_T .

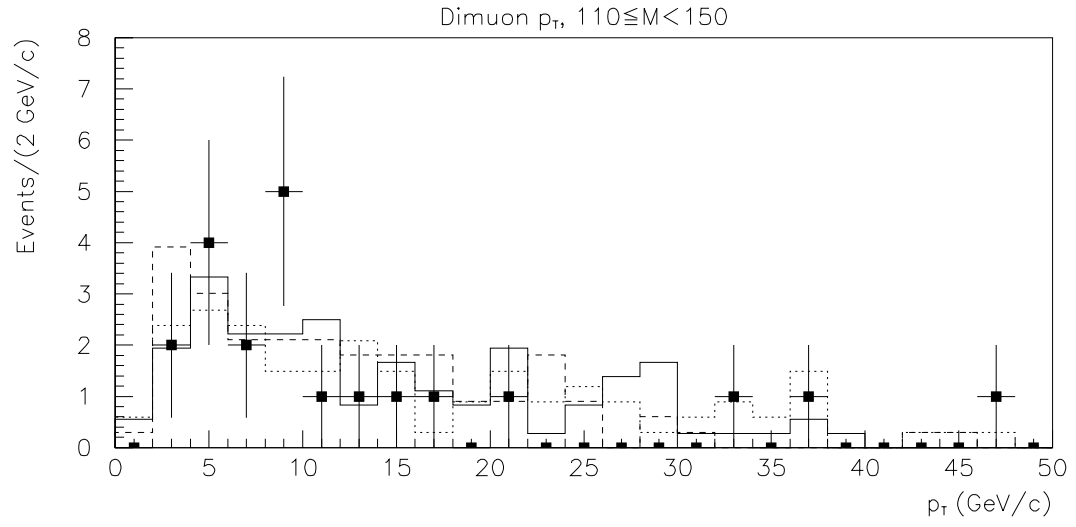


Figure 6.24: p_T distributions for data (points) and Monte Carlo with minimized χ^2 (solid line) and $\pm 4\sigma$ (dashed lines) scaling values on the Monte Carlo p_T .

Chapter 7

Background Analysis

Within our dilepton invariant mass range 11-150 GeV/c², there are several physics processes which occur besides Drell-Yan production. We consider four processes which dominate the potential backgrounds in our analysis.

Cosmic ray muons that pass through the CDF detector are often detected as if they were two back-to-back muons. Cuts such as the muon impact parameters, the opening angle of the muon tracks, and the timing of the TDCs in the hadronic calorimeter can be used to flag a dimuon event as cosmic.

Misidentification can occur as a result of photon conversion, decay-in-flight of hadrons, such as π^\pm or K^\pm , and misidentification of hadrons as leptons.

$Z \rightarrow \tau^+ \tau^-$ events in which both taus decay into leptons plus neutrinos create a wide distribution of background events in all samples (ee, e μ , and $\mu\mu$). We estimate this contribution using Monte Carlo $Z \rightarrow \tau^+ \tau^-$ events for which the detector simulation described in Chapter 5 and the identification and isolation efficiencies presented in Chapter 4 were applied to the leptonic decay products. The estimated background is found to peak in the 40-50 GeV mass range, approximately half the

Z mass.

Heavy flavor or QCD backgrounds such as b and \bar{b} semileptonic decays are considerable at lower invariant masses (11-40 GeV). The leptons in these interactions tend to be non-isolated. Also, heavy flavor decays are by far the largest contribution to the $e\mu$ event sample, so we use a normalization of high-isolation $e\mu$ events to our ee and $\mu\mu$ high-isolation samples to estimate the heavy flavor backgrounds in our isolated samples.

7.1 Removal of Cosmic Ray Muons (DIMUCOS)

The standard CDF cosmic ray filter, CMCOS^[10], was initially going to be used in this analysis, but we found that it did not remove many events in our sample which were clearly cosmic rays. This is evidenced by the peak near zero in dimuon rapidity as shown in Figure 7.1b. We devised a cosmic ray filter which is better suited to our analysis of Drell-Yan dimuons.

Our cosmic ray filter is defined as

$$\begin{aligned} Cosmic = [& (\max(d0_{\mu1}, d0_{\mu2}) > 0.15 \text{ cm}) \text{ AND } (178^\circ < \Delta\phi < 182^\circ)] \\ \text{OR } [& (\Delta TDC > 10 \text{ ns OR } TDC \text{ not valid}) \text{ AND } \textit{back to back}], \end{aligned} \quad (7.1)$$

where “back-to-back” refers to one of the two muons being within two degrees of back-to-back in ϕ with another muon in the event when the sum of the two pseudorapidities is less than 0.2. $d0$ is the impact parameter of the muon track with respect to the beam. TDC refers to the Hadron TDC, and ΔTDC is the difference in Hadron TDC timings for the two muons. ΔTDC should be zero for

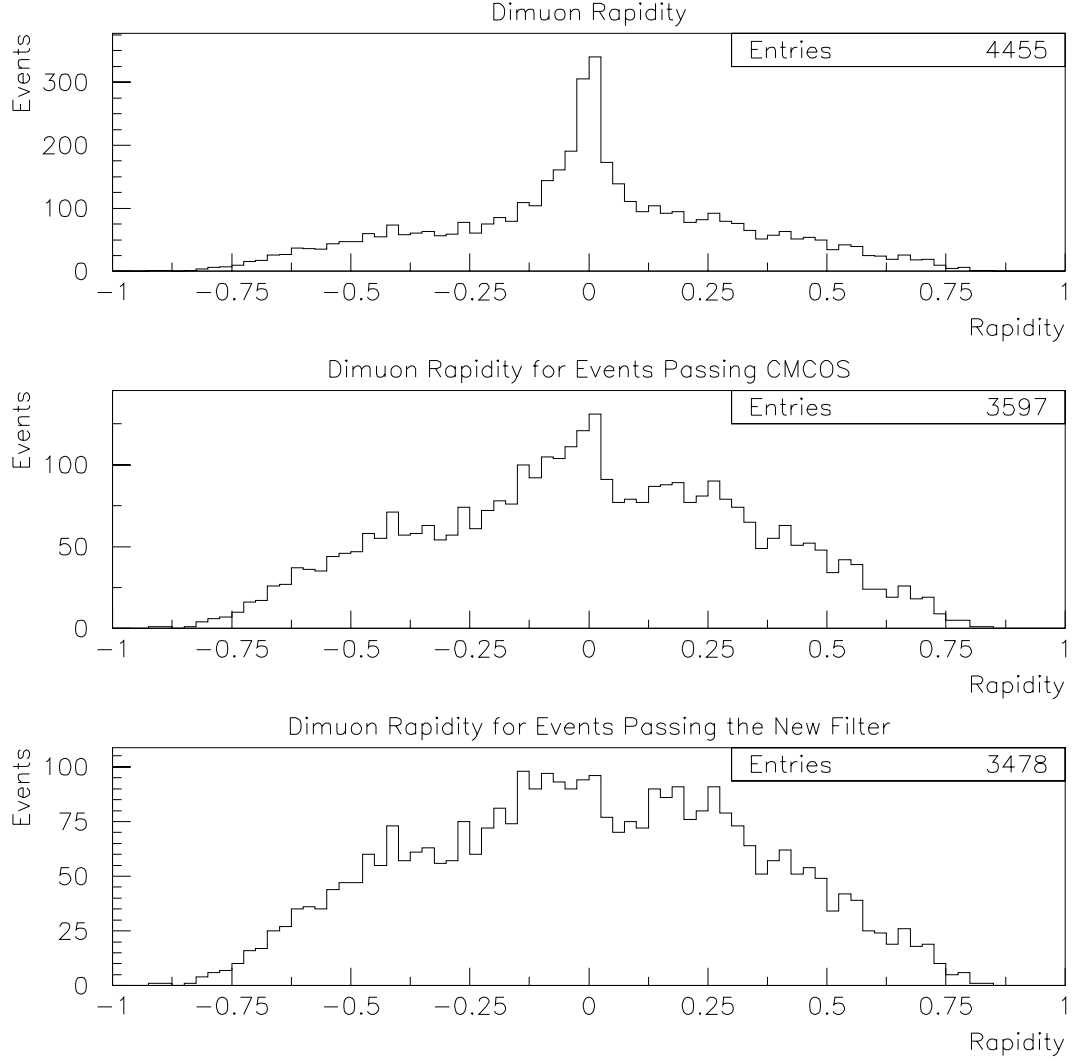


Figure 7.1: Top(a): Dimuon rapidity for selected events with no cosmic ray filter active. The peak at zero is populated by cosmic rays. Middle(b): Dimuon rapidity for selected events which passed the CMCOS filter. The peak at zero is still present. Bottom(c): Dimuon rapidity for events passing the new filter, showing no remaining cosmic rays.

real events, while most cosmics have a timing difference greater than 10 ns. Roughly 10% of the events have at least one muon with invalid Hadron TDC information. The placements of the cuts are motivated by the plots in Figures 7.2, 7.3, 7.4, 7.5, and 7.6. The plots show the effect of each cut on cosmics and Z events for comparison.

The efficiencies of each of the four individual cuts were measured using the others to pick out cosmics from a sample of non- Z s ($M_{\mu\mu} < 70$ GeV or $M_{\mu\mu} > 110$ GeV). In other words,

$$\varepsilon_{TDC} = \frac{(\Delta TDC > 10 \text{ ns } OR \text{ ~~TDC~~) AND } back \text{ to } back \text{ AND } \max(d_0^{\mu 1}, d_0^{\mu 2}) > 0.15}{back \text{ to } back \text{ AND } \max(d_0^{\mu 1}, d_0^{\mu 2}) > 0.15 \text{ cm}}$$

where ~~TDC~~ indicates that the muons did not have valid Hadron TDC information.

$$\varepsilon_{TDC} = 138/140 = 0.9857$$

$$\varepsilon_{b2b} = \frac{back \text{ to } back \text{ AND } \Delta TDC > 10 \text{ ns AND } \max(d_0^{\mu 1}, d_0^{\mu 2}) > 0.15 \text{ cm}}{\Delta TDC > 10 \text{ ns AND } \max(d_0^{\mu 1}, d_0^{\mu 2}) > 0.15 \text{ cm}}$$

$$\varepsilon_{b2b} = 122/123 = 0.9919$$

$$\varepsilon_{d0} = \frac{\max(d_0^{\mu 1}, d_0^{\mu 2}) > 0.15 \text{ cm AND } \Delta TDC > 10 \text{ ns AND } back \text{ to } back}{\Delta TDC > 10 \text{ ns AND } back \text{ to } back}$$

$$\varepsilon_{d0} = 180/293 = 0.6143$$

$$\varepsilon_{b2b\phi} = \frac{\Delta TDC > 10 \text{ ns AND } \max(d_0^{\mu 1}, d_0^{\mu 2}) > 0.15 \text{ cm AND } back \text{ to } back}{\Delta TDC > 10 \text{ ns AND } \max(d_0^{\mu 1}, d_0^{\mu 2}) > 0.15 \text{ cm AND } |\eta_{L1} + \eta_{L2}| < 0.2}$$

$$\varepsilon_{b2b\phi} = 181/182 = 0.9945$$

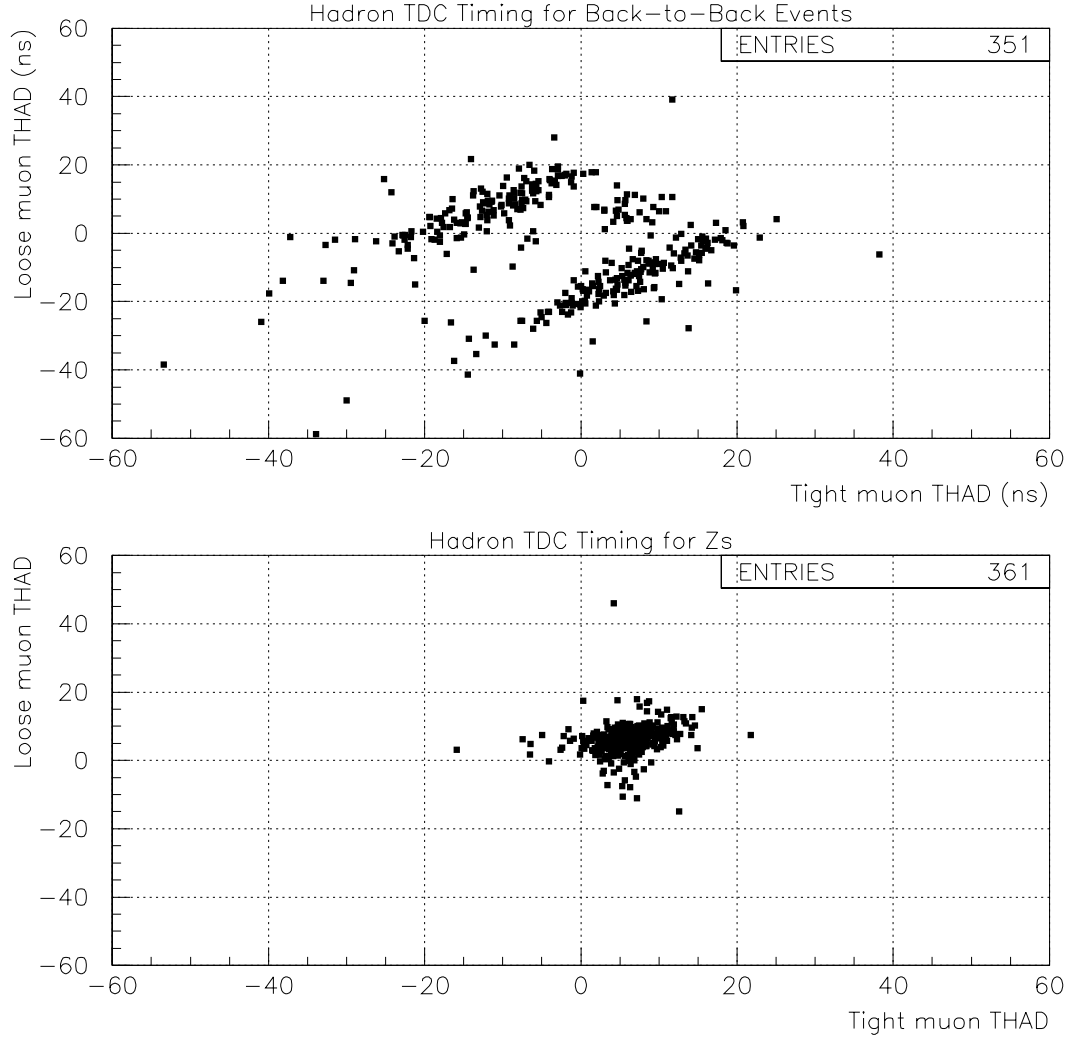


Figure 7.2: Top: Hadron TDC timings for both muons for back-to-back events outside the Z mass window. Bottom: Hadron TDC timings for Z events ($86 < M_{\mu\mu} < 96 \text{ GeV}/c^2$). Note that the two diagonal bands in the top plot clearly represent cosmic rays. Events with invalid Hadron TDC data are not shown.

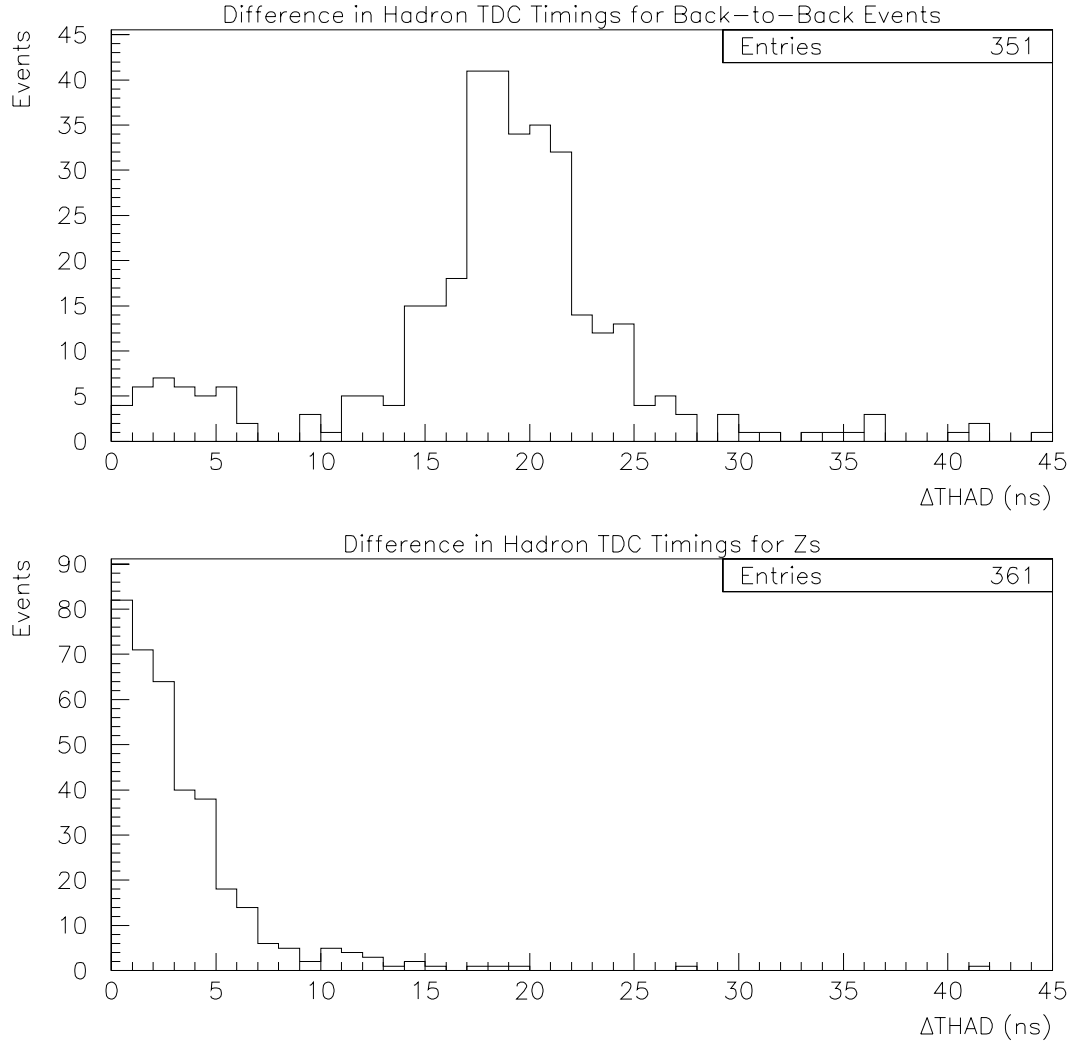


Figure 7.3: Top: Hadron TDC timing difference for back-to-back events outside the Z mass window. Bottom: Hadron TDC timing difference for Z events ($86 < M_{\mu\mu} < 96 \text{ GeV}/c^2$). Events with invalid Hadron TDC data are not shown.

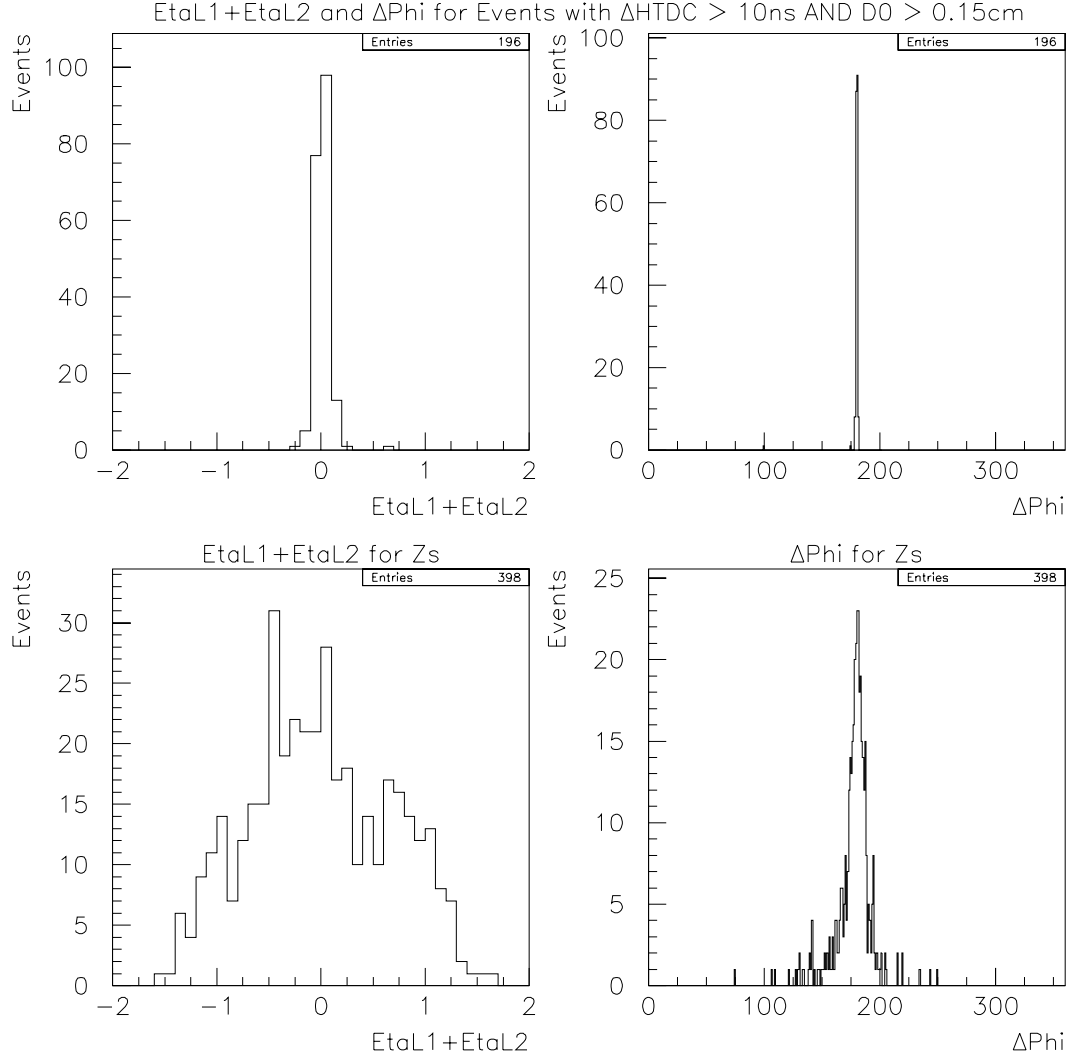


Figure 7.4: Top: Sum of the muon pseudorapidities and difference in ϕ for events outside the Z mass window for which the Hadron TDC timing and impact parameter are consistent with cosmic rays. Bottom: Sum of the muon pseudorapidities and difference in ϕ for Z events ($86 < M_{\mu\mu} < 96 \text{ GeV}/c^2$).

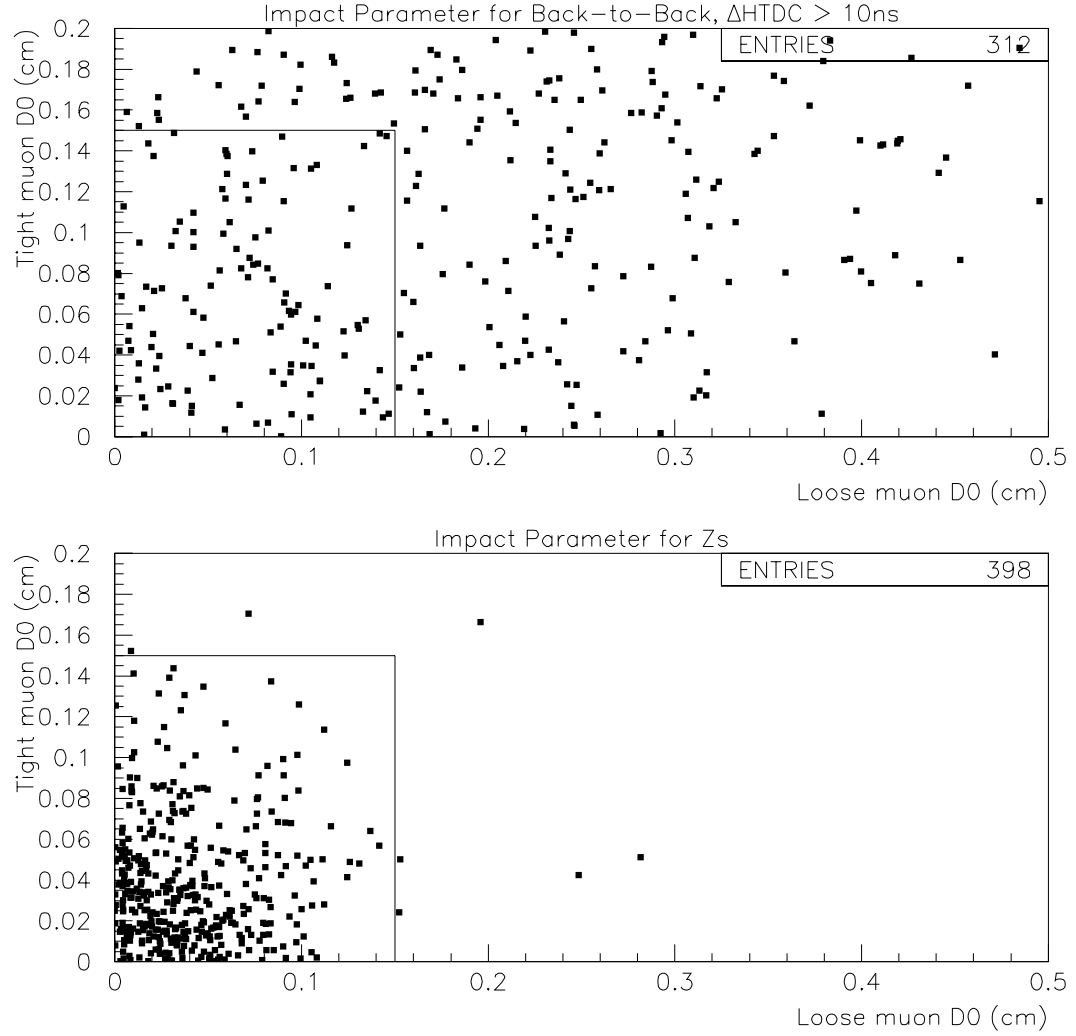


Figure 7.5: Top: Impact parameters for back-to-back events outside the Z mass window for which the Hadron TDC timing is consistent with cosmic rays. Bottom: Impact parameters for Z events ($86 < M_{\mu\mu} < 96 \text{ GeV}/c^2$). The boxed area is the area not removed by the impact parameter cut at 0.15cm.

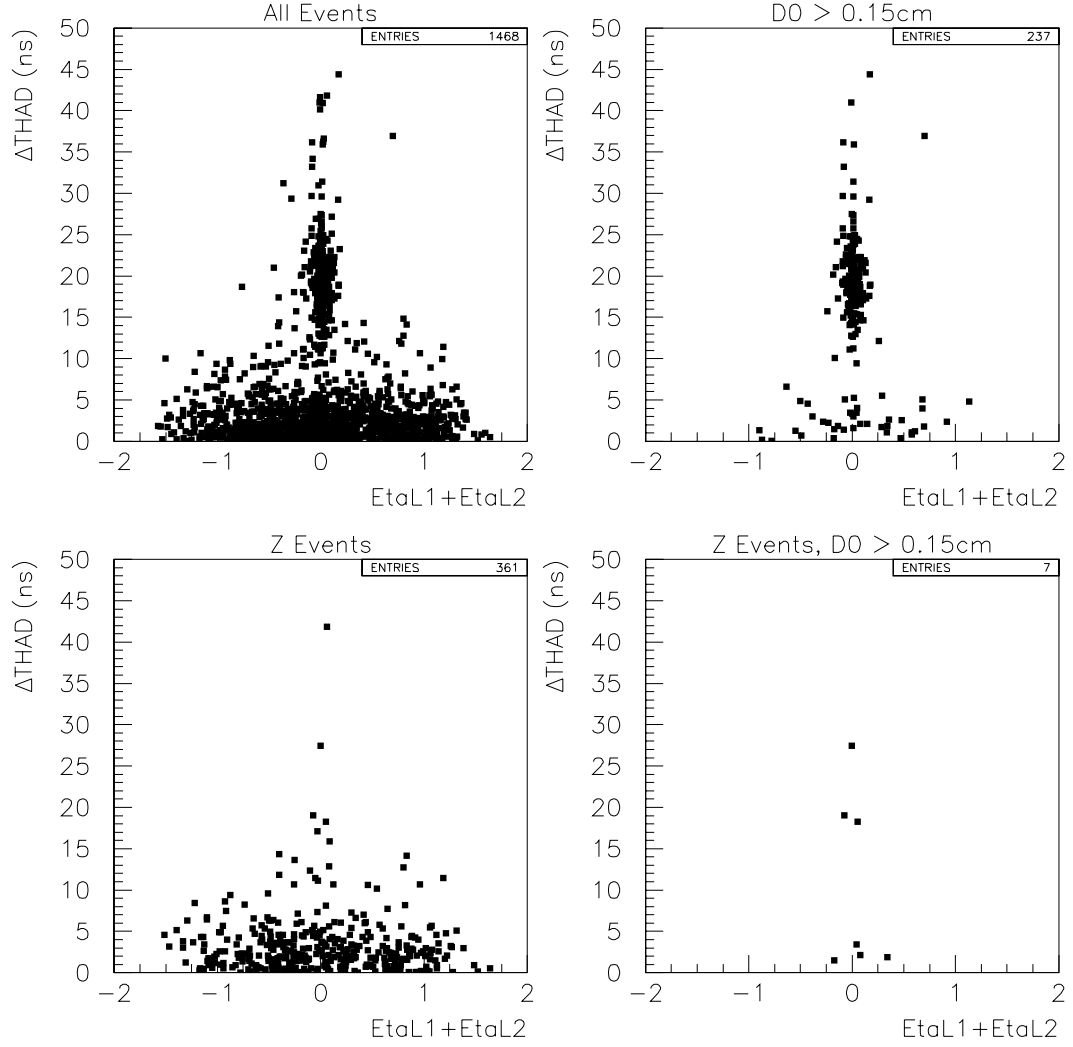


Figure 7.6: Top Left: Difference between the Hadron TDC timings plotted against the sum of the muon pseudorapidities for all events in the sample that have valid Hadron TDC information. Top Right: The same as the top left plot, requiring also that the impact parameter is greater than 0.15cm. Bottom Left and Right: The same as the top plots, but including only Z events ($86 < M_{\mu\mu} < 96 \text{ GeV}/c^2$).

The fraction of cosmic rays expected to slip through the filter is

$$(1 - \varepsilon_{filter}) = (1 - \varepsilon_{d0}\varepsilon_{b2b\phi})(1 - \varepsilon_{b2b}\varepsilon_{TDC})$$

This number is 0.0087. Therefore, our cosmic ray filter is found to be 99.13% efficient. For example, since the Drell-Yan sample is about 20% cosmics before running this filter, we expect only $0.0087 \times 20\% = 0.2\%$ contamination of the final sample with cosmics.

A sample of 398 Z events (mass between 86 and 96 GeV/c^2 , and passing our trigger/selection requirements) had 5 events which have been flagged as cosmic rays by our filter. For each of those 5 events we performed an additional check of CTC timing using a **ctcosm** routine, which is a part of the CMCOS filter algorithm. For technical reasons, **ctcosm** could only be run on selected events. Given two tracks, which are assumed to be two legs of a single particle, **ctcosm** calculates particle propagation velocity in units of the speed of light. If both tracks are coming from the primary vertex, the velocity should be zero, while for a cosmic muon it should be one. Of the 5 events, 4 pairs of back-to-back muon tracks have velocity consistent with one. We therefore conclude that only 1 event out of the 5 is not a cosmic, so the over-efficiency of the filter for $Z \rightarrow \mu\mu$ is 0.25%.

A separate estimate of the number of cosmics in our sample of 398 Z events predicts approximately six events. This estimate was done by first predicting the total number of cosmics in the unfiltered sample using Figure 7.7. The number of cosmics was predicted to be 314 ± 41 ; the actual number of events which our filter flagged as cosmic was 358. The number of those which fell in the two 5 GeV/c^2 sidebands near the Z peak is 7. Therefore, a crude estimate of the number of

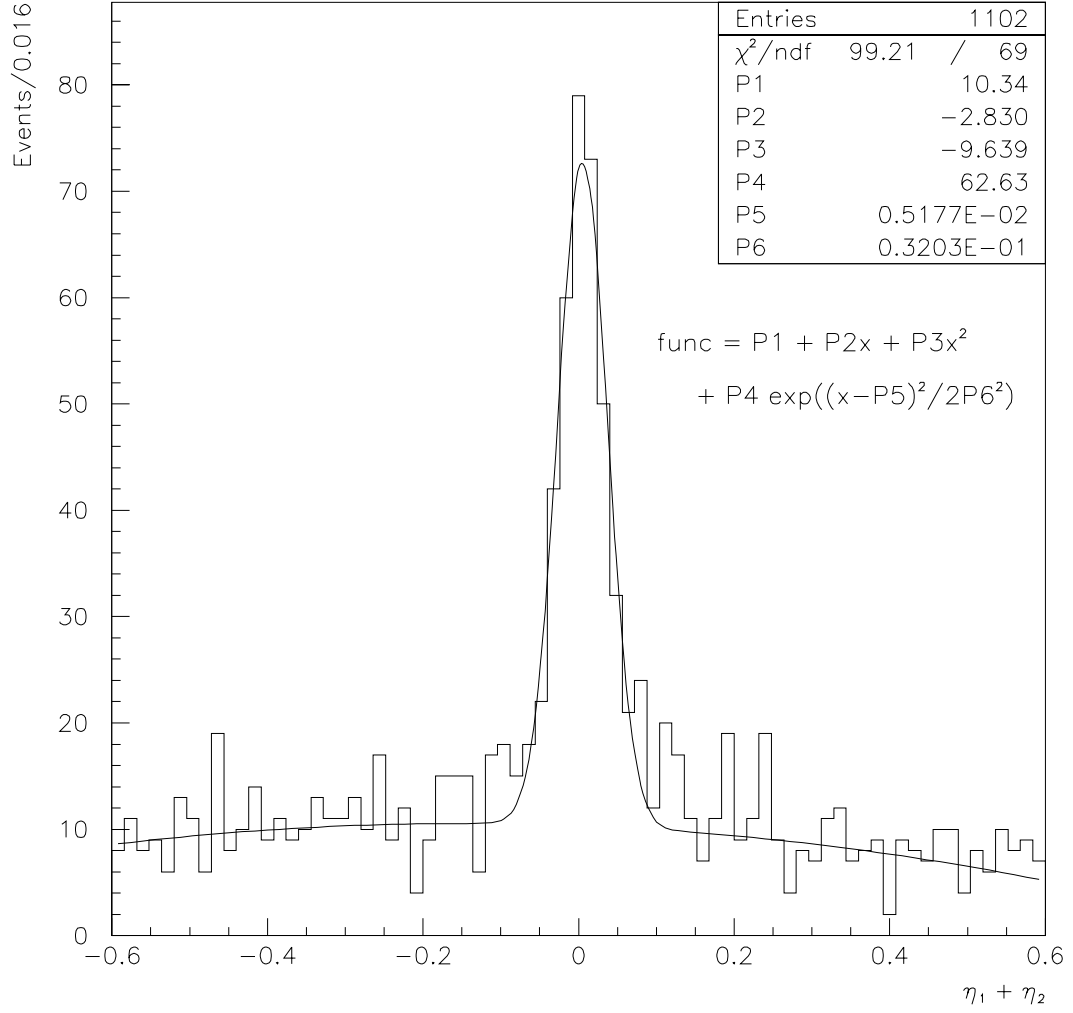


Figure 7.7: Distribution of $\eta_{\mu 1} + \eta_{\mu 2}$ for cosmics and data. The peak is fit with a gaussian, and the number of cosmics in the sample is estimated to be $P4 \times P6 \times \sqrt{2\pi}/0.016 = 314.2$.

cosmics in the Z mass window is $(7/358) \times 314 = 6 \pm 2$. This is consistent with both the CTC timing check (4 events) and with the results of our filter (5 events).

7.2 Subtraction of Misidentification Backgrounds

The dilepton data sample contains background events due to photon conversion, decay in flight of hadrons, and misidentification of hadrons as leptons. All of these backgrounds are equally likely to produce same-sign lepton pairs as they are opposite-sign lepton pairs (see the earlier discussion regarding the isolation distributions shown in Figures 4.5 and 4.6). Therefore, to remove this type of background, the number of same-sign events in each mass bin is subtracted from the number of opposite-sign events.

The electron data set had 61 same-sign events (27 positive, 34 negative). The muon data set had 120 same-sign events (64 positive, 56 negative).

7.3 $Z \rightarrow \tau^+ \tau^-$ Background

The HERWIG Monte Carlo described in Chapter 5 was used to generate 250,000 $\gamma^*/Z \rightarrow \tau^+ \tau^-$ events in the mass range $9 < M < 120$ GeV. The mass distribution is shown in Figure 7.8 (top). The taus were then “decayed” leptonically (e.g. $\tau \rightarrow e \nu \nu$) into three categories, ee , $\mu\mu$, and $e\mu$, after which the detector simulation described in Section 5.2 was applied. Figure 7.8 (bottom) shows the $\tau\tau$ mass distribution of the events in which the electron and muon decay products survived the detector simulation. Clearly, the vast majority of surviving $\tau\tau$ events originated as Z s. For this reason, and because the cross-section for $Z \rightarrow \tau\tau$ is well known (approximately 225 ± 15 pb)^[23], we consider only $\tau\tau$ events that originated as Z s (i.e. $66 < M <$

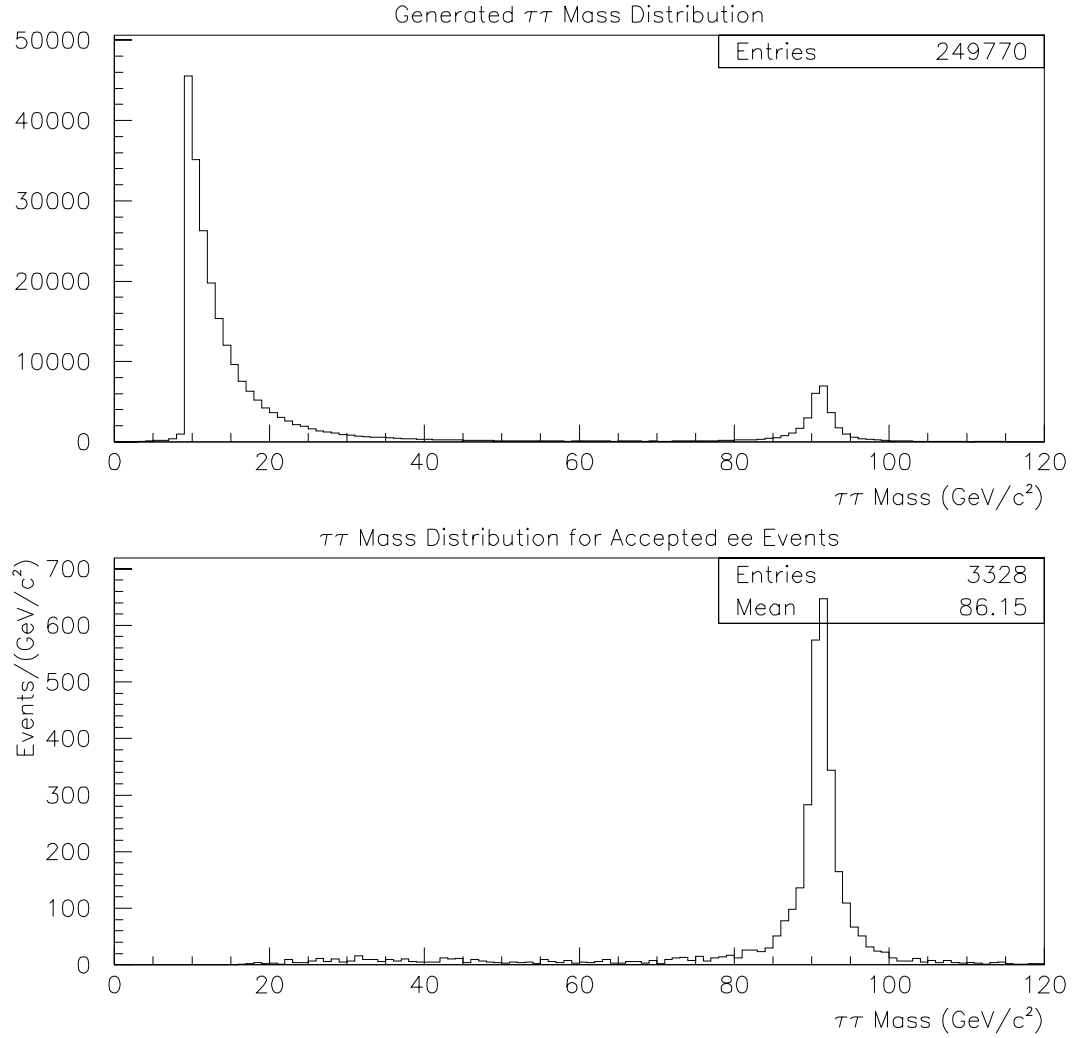


Figure 7.8: Mass distributions of $\gamma^*/Z \rightarrow \tau^+\tau^-$ Monte Carlo events. The top plot show the invariant mass of tau lepton pairs that were generated using the HERWIG Monte Carlo. The bottom plot shows the invariant mass of the tau lepton pairs that were “decayed” into electron pairs plus neutrinos and accepted by the detector and trigger simulations. The majority of the events that survive are from $Z \rightarrow \tau^+\tau^-$.

116 GeV) in our background estimation.

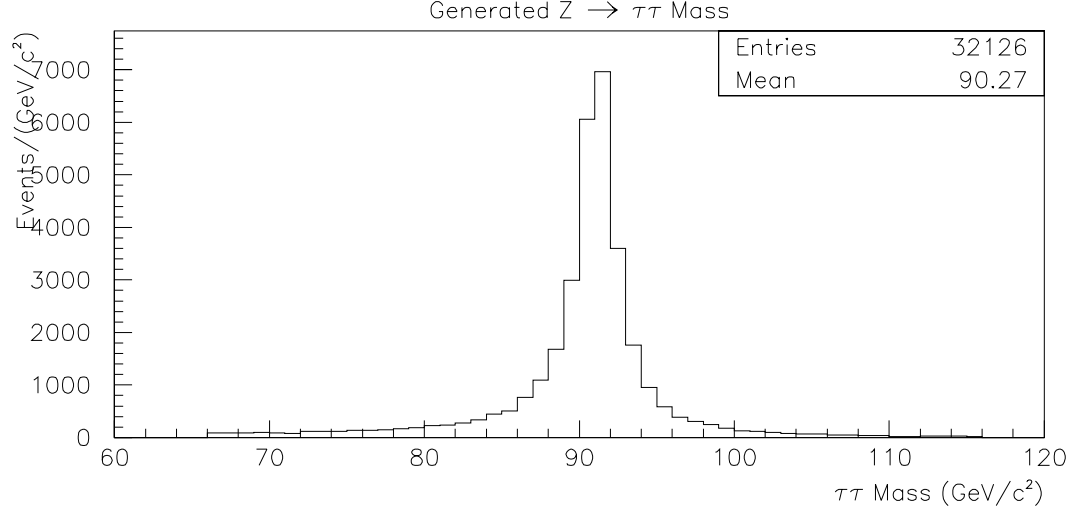


Figure 7.9: Mass distribution of $Z \rightarrow \tau^+\tau^-$ Monte Carlo events. This is the subset of the $\gamma^*/Z \rightarrow \tau^+\tau^-$ Monte Carlo where the tau lepton pairs are within the mass range $66 < M < 116$ GeV.

Both of our data samples, electron and muon, had integrated luminosities of roughly 85 pb^{-1} , so we assume the same integrated luminosity of $\tau^+\tau^-$. Throughout the entire CDF Run 1b approximately ($220 \text{ pb} \times 85 \text{ pb}^{-1} = 18700$) $Z \rightarrow \tau\tau$ events should have been produced. Of the 250,000 Monte Carlo events generated, 32,126 were in the $66 < M < 116$ GeV mass range (Figure 7.9), so we use a luminosity normalization of ($18700/32126 = 0.58$). The estimated contribution of $Z \rightarrow \tau\tau$ in our data samples is given by equation 7.2.

$$N_{data}^{\tau\tau \rightarrow l_1 l_2} = N_{MC}^{\tau\tau \rightarrow l_1 l_2} \times \frac{85 \text{ pb}^{-1} \times 220 \text{ pb}}{N_{MC}^{Z \rightarrow \tau\tau}} \times BR(\tau \rightarrow l_1) BR(\tau \rightarrow l_2) \times \varepsilon_{iso}^{l_1 l_2} \times \varepsilon_{ID}^{l_1 l_2} \times \varepsilon_{zvert} \quad (7.2)$$

Where the branching ratios $BR(\tau \rightarrow e\bar{\nu}_e\nu_\tau) = (17.81 \pm 0.07)\%$ and $BR(\tau \rightarrow \mu\bar{\nu}_\mu\nu_\tau) = (17.37 \pm 0.09)\%$ [22] were used. The number of $e\mu$ events was multiplied by two

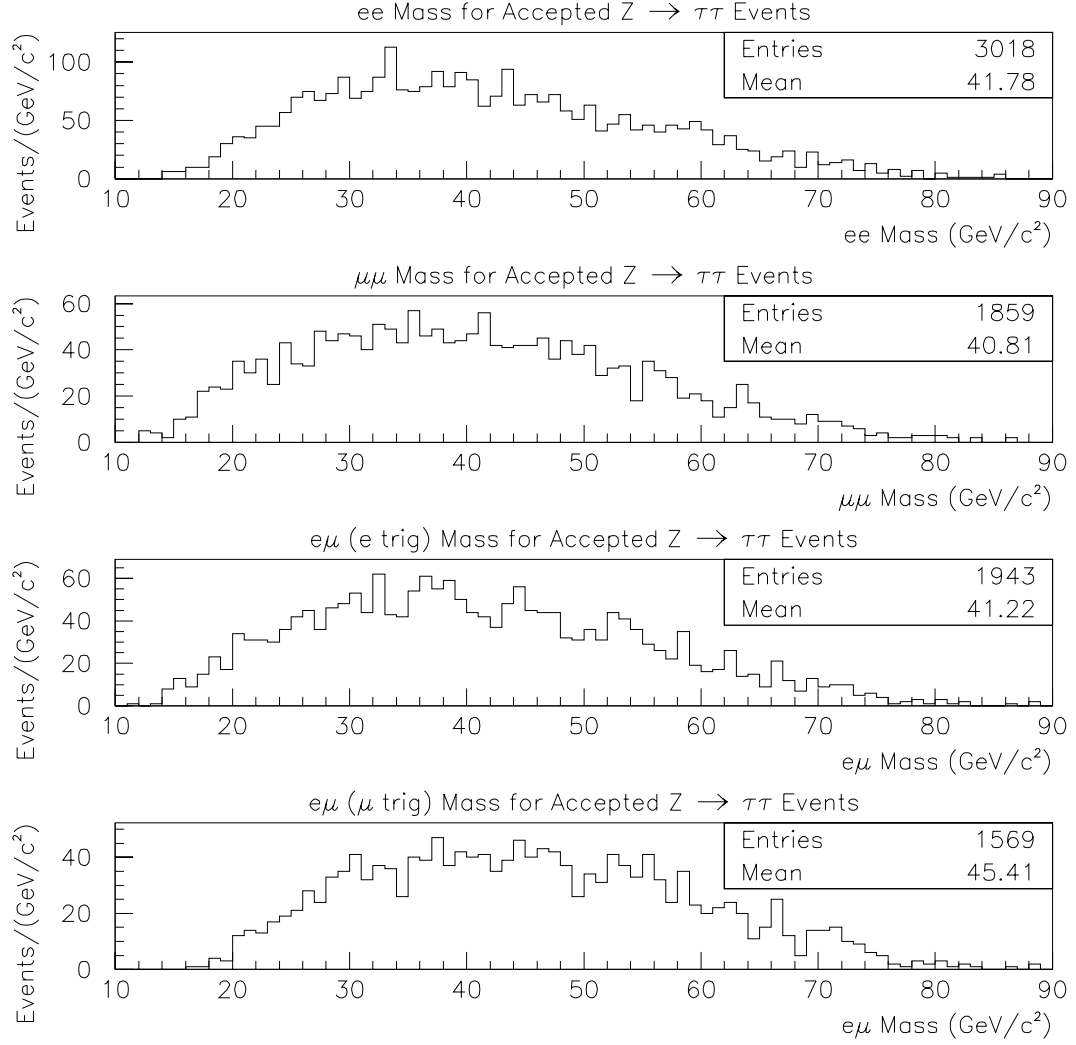


Figure 7.10: Mass distributions of accepted $Z \rightarrow \tau^+\tau^- \rightarrow l^+l^-$ Monte Carlo events. The top plot is for $\tau\tau$ events in which both taus decay into electrons plus neutrinos, and for which both electrons passed the simulated detector and trigger efficiencies. The plots following it are analogous, and they contain, respectively, $\mu\mu$, $e\mu$ (passing e triggers), and $e\mu$ (passing μ triggers) Monte Carlo events.

since the $\tau\tau$ decay products could be either $e\mu$ or μe . The isolation efficiencies are the same as those in Section 4.5.1, namely $\varepsilon_{iso}^{ee} = .681 \pm .013$, $\varepsilon_{iso}^{\mu\mu} = .756 \pm .016$, and the extrapolation $\varepsilon_{iso}^{e\mu} = .717 \pm .010$.

The four plots in Figure 7.10 show the mass distributions of the ee , $\mu\mu$, $e\mu$ (passing e triggers), and $e\mu$ (passing μ triggers) simulated events. The numbers of events are, respectively, 3018, 1859, 1943, and 1569. Using Equation 7.2, we determine that 27.7 ± 1.6 ee , 19.3 ± 1.4 $\mu\mu$, 18.3 ± 1.3 $e\mu$ (e triggers), and 15.2 ± 1.2 $e\mu$ (μ triggers) events should appear in our data sample. The contribution to the data samples is shown for each mass bin in Table 7.1.

Table 7.1: Estimate of $\tau\tau$ contribution to data samples.

Mass bin	ee	$\mu\mu$	$e\mu$ (e trig)	$e\mu$ (μ trig)
11-15	0.06 ± 0.02	0.11 ± 0.04	0.19 ± 0.06	0.00 ± 0.00
15-20	0.69 ± 0.09	0.93 ± 0.12	0.72 ± 0.10	0.09 ± 0.03
20-30	5.4 ± 0.5	3.9 ± 0.4	3.5 ± 0.3	2.1 ± 0.2
30-40	7.7 ± 0.6	4.9 ± 0.4	4.9 ± 0.4	3.7 ± 0.3
40-50	6.4 ± 0.5	4.5 ± 0.4	4.0 ± 0.3	3.8 ± 0.3
50-60	4.3 ± 0.4	3.0 ± 0.3	3.0 ± 0.3	3.2 ± 0.3
60-70	2.3 ± 0.2	1.4 ± 0.2	1.4 ± 0.2	1.6 ± 0.2
70-110	0.89 ± 0.11	0.59 ± 0.09	0.58 ± 0.08	0.77 ± 0.10

7.4 Heavy Flavor Background

Unlike misidentification background, heavy flavor background will produce more opposite-sign dilepton events than same-sign events. Heavy flavor background differs from the Drell-Yan signal in that it is mostly non-isolated. The isolation of leptons from heavy flavor decays also should not depend on whether the dileptons are ee , $e\mu$, or $\mu\mu$. We therefore use the numbers of isolated and non-isolated dilep-

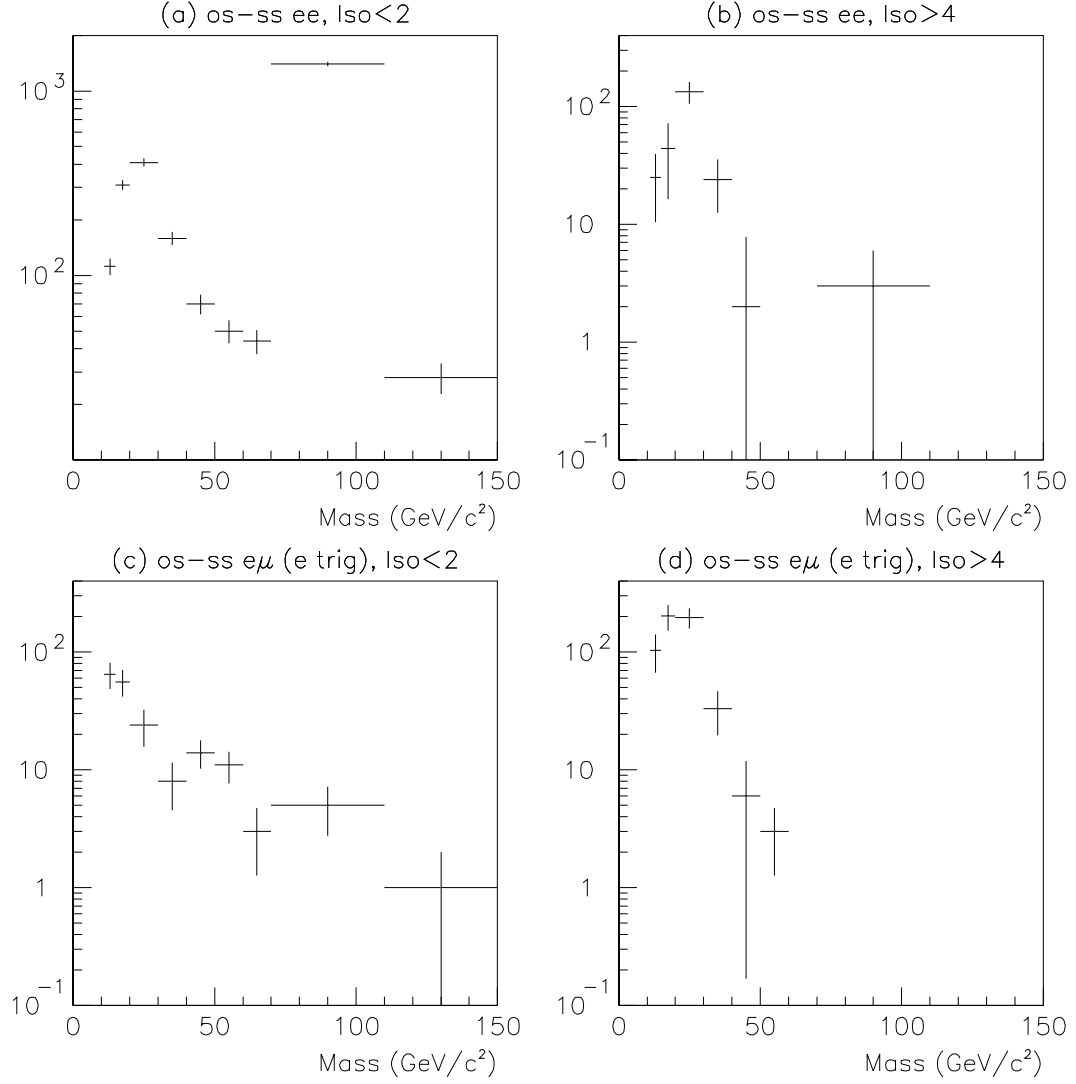


Figure 7.11: Mass distributions of e^+e^- data and background. (a) shows the mass distribution of the Drell-Yan data, with only the misidentification (same-sign) background subtracted. (b) shows the mass distribution of non-isolated e^+e^- events. The plot represents the distribution of heavy-flavor background events in the data sample. (c) shows the mass distribution of isolated $e\mu$ events which passed the electron trigger path. The $\tau\tau$ contribution has not been subtracted yet (see Figure 7.13). (d) shows the mass distribution of non-isolated $e\mu$ events which passed the electron trigger path.

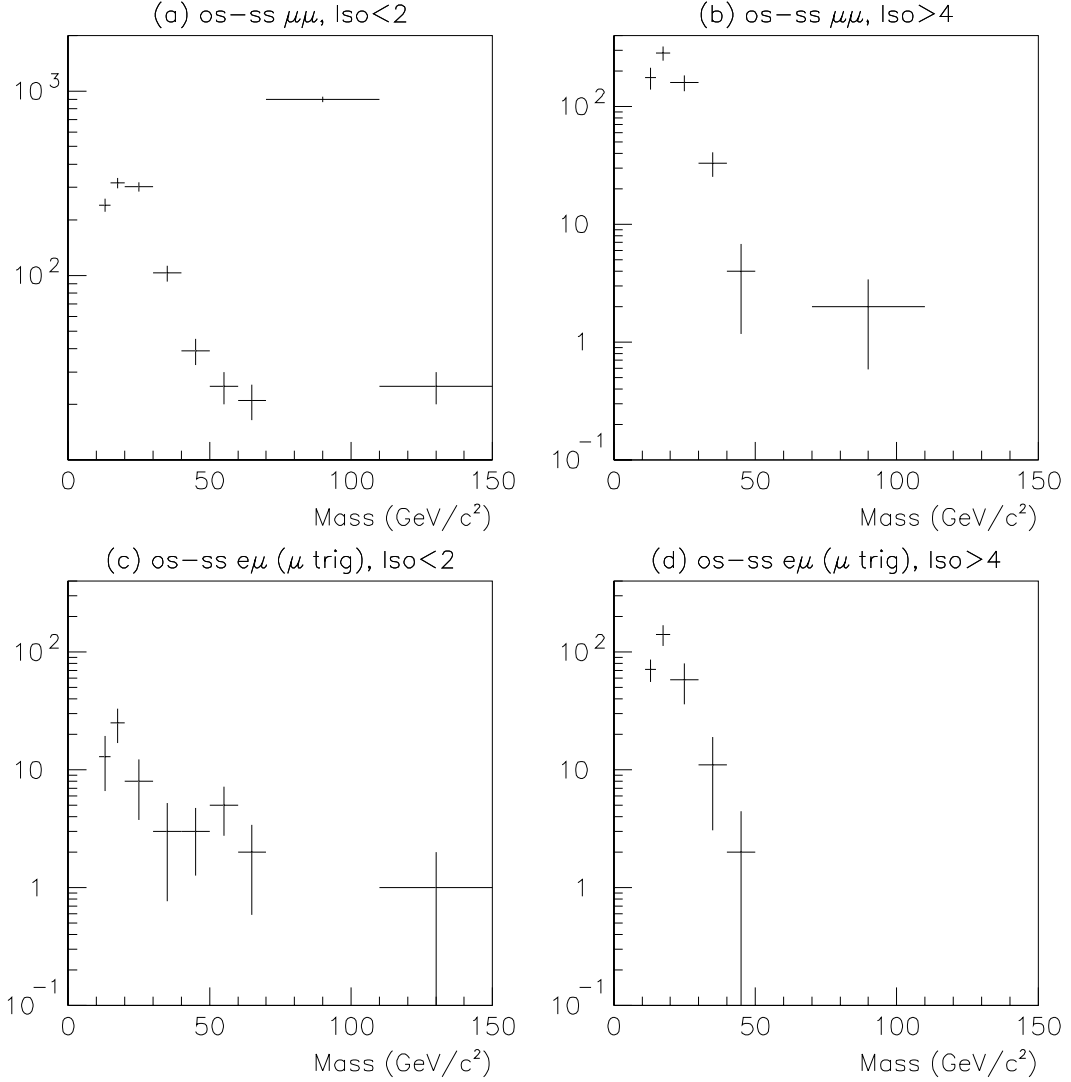


Figure 7.12: Mass distributions of $\mu^+\mu^-$ data and background. (a) shows the mass distribution of the Drell-Yan data, with only the misidentification (same-sign) background subtracted. (b) shows the mass distribution of non-isolated $\mu^+\mu^-$ events. The plot represents the distribution of heavy-flavor background events in the data sample. (c) shows the mass distribution of isolated $e\mu$ events which passed the muon trigger path. The $\tau\tau$ contribution has not been subtracted yet (see Figure 7.13). (d) shows the mass distribution of non-isolated $e\mu$ events which passed the muon trigger path.

tons in the $e\mu$ channel to determine the background to Drell-Yan from this source in the ee and $\mu\mu$ channels.

Figures 7.11 and 7.12 show the mass distributions for signal and background contributions to the dielectron and dimuon data samples. Figure 7.11(a) shows the mass distribution of isolated Drell-Yan ee events where only the misidentification (same-sign) background has been subtracted. Figure 7.11(b) shows the mass distribution of ee events where both of the electrons have an isolation value greater than 4 GeV. The isolation cut is higher than we use elsewhere in this analysis to ensure that little or no signal penetrates the background sample. Only three possible $Z \rightarrow e^+e^-$ events ($70 < M < 110$ GeV) passed the cut, compared to approximately 1400 isolated Zs in the Drell-Yan sample. Figure 7.11(c) shows the mass distribution of isolated $e\mu$ events which passed our electron trigger path. There is a slight bump at about 40-60 GeV which probably represents the $\tau\tau$ contribution. Figure 7.11(d) shows the mass distribution of non-isolated $e\mu$ events. We expect nothing but heavy flavor events in this plot, so it shows the relative heavy flavor contribution in each mass bin. There are no events above 60 GeV. Figures 7.11(b) and (d) are similar, as expected because they both contain only high-isolation heavy flavor background. Figure 7.12(a)-(d) show the analogous plots for dimuon background estimation. Again, Figures 7.12(b) and (d) are similar.

$Z \rightarrow \tau^+\tau^-$ events are twice as likely to show up in the $e\mu$ samples as they are in either of the ee or $\mu\mu$ samples. To avoid double-counting, the estimated $\tau\tau$ contribution to the $e\mu$ samples is removed before calculating the heavy flavor background. The number of expected $\tau\tau$ events in each mass bin is given in Table 7.1. The two plots in Figure 7.13 show the mass distributions of isolated $e\mu$ events which pass the electron and muon triggers.

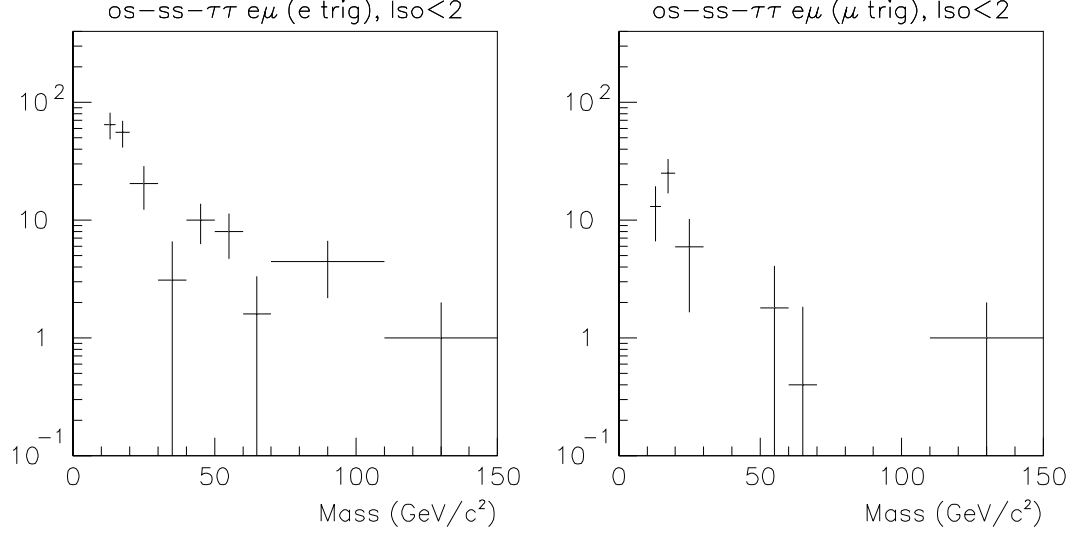


Figure 7.13: Mass distributions of isolated $e\mu$ events with the estimated $\tau\tau$ contribution subtracted. The left plot is the same as Figure 7.11(c) minus the $\tau\tau \rightarrow e\mu$ (e trigger) background given in Table 7.1. The right plot is the same as Figure 7.12(c) minus the $\tau\tau \rightarrow e\mu$ (μ trigger) background given in Table 7.1.

The heavy flavor background estimation is done by scaling the $e\mu$ data so that the number of high-isolation $e\mu$ events ($I_1, I_2 > 4$ GeV) appears to be the same as the number of high-isolation dielectron (dimuon) events. The background, i.e. the expected number of heavy flavor events in the low-isolation ee ($\mu\mu$) region is then the same as the number of low-isolation $e\mu$ events, scaled by the relative numbers of high-isolation events in the ee and $e\mu$ samples. The amount of expected heavy flavor background in each sample is given by the following equations.

$$N_{bgd}^{ee} = \frac{(N_{os}^{ee} - N_{ss}^{ee})^{Iso>4}}{(N_{os}^{e\mu} - N_{ss}^{e\mu})^{Iso>4}} \times (N_{os}^{e\mu} - N_{ss}^{e\mu} - N^{\tau\tau \rightarrow e\mu})^{Iso<2} \quad (7.3)$$

where the $e\mu$ events have passed the electron trigger path, and the estimated number

of $\tau\tau \rightarrow e\mu$ events ($N^{\tau\tau \rightarrow e\mu}$) is given in the fourth column of Table 7.1.

$$N_{bkgd}^{\mu\mu} = \frac{(N_{os}^{\mu\mu} - N_{ss}^{\mu\mu})^{Iso>4}}{(N_{os}^{e\mu} - N_{ss}^{e\mu})^{Iso>4}} \times (N_{os}^{e\mu} - N_{ss}^{e\mu} - N^{\tau\tau \rightarrow e\mu})^{Iso<2} \quad (7.4)$$

where the $e\mu$ events have passed the muon trigger path, and the estimated number of $\tau\tau \rightarrow e\mu$ events ($N^{\tau\tau \rightarrow e\mu}$) is given in the fifth column of Table 7.1.

Table 7.2 summarizes the heavy flavor background estimation. The uncertainties arise from propagating the statistical errors in all samples used for the determination: opposite and same-sign samples in both high and low isolation regions.

We intended to test our background estimations using impact parameters from the SVX detector. However, only half the leptons had tracks that traversed the SVX, and the statistics were too low to do a good background estimation.

Table 7.2: Heavy Flavor Background from (os-ss) Isolation Distributions.

Electrons									
Mass	Iso>4 GeV				Norm.	Iso<2 GeV			Est. Bkgd.
	os $e\mu$	ss $e\mu$	os ee	ss ee		os $e\mu$	ss $e\mu$	$\tau\tau \rightarrow e\mu$	
11-15	742	638	119	94	0.24	166	101	0.19	15.6 ± 11.4
15-20	1326	1124	407	363	0.22	129	73	0.72	12.0 ± 8.7
20-30	844	647	464	331	0.68	46	22	3.5	13.8 ± 6.9
30-40	107	74	79	55	0.73	10	2	4.9	2.3 ± 2.9
40-50	20	14	18	16	0.33	14	0	4.0	3.3 ± 10.4
Muons									
Mass	Iso>4 GeV				Norm.	Iso<2 GeV			Est. Bkgd.
	os $e\mu$	ss $e\mu$	os $\mu\mu$	ss $\mu\mu$		os $e\mu$	ss $e\mu$	$\tau\tau \rightarrow e\mu$	
11-15	151	80	745	573	2.42	27	14	0.00	31.5 ± 18.2
15-20	459	318	911	639	1.93	45	20	0.09	48.1 ± 19.5
20-30	273	215	376	226	2.59	13	5	2.1	15.3 ± 12.7
30-40	37	26	45	13	2.91	4	1	3.7	0.0 ± 6.7
40-50	4	2	6	2	2.00	3	0	3.8	0.0 ± 4.1

7.5 Summary of Estimated Backgrounds

Table 7.3 summarizes all of the estimated backgrounds to the Drell-Yan di-electron and dimuon samples. The same-sign misidentification background is not included in the total background, since it was subtracted before the heavy flavor background was estimated.

Table 7.3: Table of estimated backgrounds to the Drell-Yan samples. The final column is the ratio of the total background to the same-sign subtracted number of events.

Electrons						
Mass bin	N_{os}	N_{ss}	$\tau\tau \rightarrow ee$	Heavy flavor	Total Bkgd	% Bkgd.
11-15	124	12	0.06 ± 0.02	15.6 ± 11.4	15.6 ± 11.4	14.0 ± 10.1
15-20	337	27	0.69 ± 0.09	12.0 ± 8.7	12.7 ± 8.7	4.1 ± 2.8
20-30	428	18	5.4 ± 0.5	13.8 ± 6.9	19.2 ± 6.9	4.7 ± 1.7
30-40	161	2	7.7 ± 0.6	2.3 ± 2.9	9.9 ± 3.0	6.2 ± 1.9
40-50	72	2	6.4 ± 0.5	3.3 ± 10.4	9.7 ± 10.4	13.9 ± 14.8
50-60	50	0	4.3 ± 0.4	0.0 ± 3.3	4.3 ± 3.3	8.7 ± 6.7
60-70	44	0	2.3 ± 0.2	0.0 ± 1.7	2.3 ± 1.7	5.2 ± 4.0
70-110	1404	0	0.9 ± 0.1	0.0 ± 2.2	0.9 ± 2.2	0.1 ± 0.2
110-150	28	0	0.0 ± 0.0	0.0 ± 1.0	0.0 ± 1.0	0.0 ± 3.6
Muons						
Mass bin	N_{os}	N_{ss}	$\tau\tau \rightarrow \mu\mu$	Heavy flavor	Total Bkgd	% Bkgd.
11-15	312	77	0.11 ± 0.04	31.5 ± 18.2	31.6 ± 18.2	13.4 ± 7.7
15-20	348	35	0.9 ± 0.1	48.1 ± 19.5	49.0 ± 19.5	15.7 ± 6.2
20-30	303	8	3.9 ± 0.4	15.3 ± 12.7	19.2 ± 12.7	6.5 ± 4.3
30-40	101	0	4.9 ± 0.4	0.0 ± 6.7	4.9 ± 6.7	4.8 ± 6.7
40-50	39	0	4.5 ± 0.4	0.0 ± 4.1	4.5 ± 4.2	11.5 ± 10.7
50-60	24	0	3.0 ± 0.3	0.0 ± 2.2	3.0 ± 2.3	12.4 ± 9.4
60-70	20	0	1.4 ± 0.2	0.0 ± 1.4	1.4 ± 1.4	7.1 ± 7.1
70-110	884	0	0.59 ± 0.09	0.0 ± 0.0	0.6 ± 0.1	0.1 ± 0.0
110-150	25	0	0.0 ± 0.0	0.0 ± 1.0	0.0 ± 1.0	0.0 ± 4.0

Chapter 8

Results and Conclusions

This chapter describes the Drell-Yan differential cross-section calculation and presents the results of this analysis. The cross-section results are compared with theoretical predictions and published measurements of $\sigma B(Z \rightarrow l^+l^-)$ as a cross-check of our experimental validity. A discussion of the results concludes the chapter and the dissertation.

8.1 Cross-Section Calculation

In order to make comparisons with predictions and previous cross-section measurements we measure the differential cross-section $d\sigma/dM$. Since we use the central region of the CDF detector, $|y| < 1$, we add the rapidity differential, dy , by dividing by the width in rapidity. The differential cross-section for Drell-Yan production is calculated using the following equation:

$$\left. \frac{d^2\sigma}{dMdy} \right|_{|y|<1} = \frac{N_{os} - N_{ss} - N_{bg}}{\Delta M \Delta y A \varepsilon_{trig} \varepsilon_{id} \varepsilon_{iso} \varepsilon_{cosmic} \varepsilon_{zvert} \int \mathcal{L} dt} \quad (8.1)$$

where ΔM refers to the width of the mass bin (for example, 4 GeV in the mass range $11 < M_{ll} < 15$ GeV), and $\Delta y = 2.0$ is the width in rapidity. The detector acceptance, A , and the other efficiencies were discussed in the previous chapters.

Table 8.1 lists some of the quantities that are used in the cross-section calculations for dielectrons and dimuons. N_{os} is the number of opposite-sign events in the sample for the given mass bin. N_{ss} is the number of same-sign events which are to be subtracted from N_{os} to remove misidentification backgrounds. N_{bg} is the estimated amount of heavy flavor and $Z \rightarrow \tau^+ \tau^-$ backgrounds. The quantity N_{corr} is the number of background subtracted Drell-Yan events ($N_{os} - N_{ss} - N_{bg}$) in the mass bin, corrected for photon radiation and transverse energy/momentum smearing as described in Section 6.2. The detector acceptance, A , was also described in Section 6.2. The trigger efficiency, ε_{trig} was described in Section 6.1.4.

The following efficiencies are used in the cross-section calculation and are *not* listed in Table 8.1, because they have no mass dependence: the lepton identification efficiencies, $\varepsilon_{ID}^{ee} = 0.78 \pm 0.01$ and $\varepsilon_{ID}^{\mu\mu} = 0.83 \pm 0.01$; the isolation efficiencies, ε_{iso}^{ee} and $\varepsilon_{iso}^{\mu\mu}$ (see Section 4.5.1); and the z vertex efficiency $\varepsilon_{zvert} = 0.937 \pm 0.011$. All of these quantities were described in Chapter 4. The dimuon cosmic ray efficiency, ε_{cosmic} , is 0.9975 ± 0.0025 (see Section 7.1). For dielectrons, ε_{cosmic} is 1.0.

Lepton pair statistical and systematic uncertainties are listed in Table 8.2 (electrons) and Table 8.3 (muons). The percent uncertainty on the cross-section measurement is listed for: *statistical*, calculated from Poisson errors on the quantities N_{os} and N_{ss} relative to the corrected, background-subtracted number of events, N_{corr} ; *luminosity*, which had a 4.1% uncertainty in Run 1b; *backgrounds*, described in Chapter 7; *p_T scaling* and *varying the structure function set*, which as shown in Sections 6.3.1 and 6.3.2 reveal a significant uncertainty on the value $A \times \varepsilon_{trig}$,

Table 8.1: Values Used in the Cross-Section Calculation

Electrons, $\int \mathcal{L} dt = 85.37 \pm 3.50 \text{ pb}^{-1}$						
Mass	N_{os}	N_{ss}	N_{bg}	N_{corr}	Acceptance	ε_{trig}
11-15	124	12	15.6 ± 11.4	88.1 ± 18.7	0.033 ± 0.002	0.28 ± 0.02
15-20	337	27	12.7 ± 8.7	292.2 ± 23.9	0.198 ± 0.010	0.42 ± 0.02
20-30	428	18	19.2 ± 6.9	398.8 ± 24.3	0.255 ± 0.013	0.66 ± 0.02
30-40	161	2	9.9 ± 3.0	152.0 ± 14.6	0.263 ± 0.013	0.80 ± 0.02
40-50	72	2	9.7 ± 10.4	56.9 ± 15.0	0.265 ± 0.013	0.89 ± 0.02
50-60	50	0	4.3 ± 3.3	42.0 ± 9.0	0.271 ± 0.014	0.96 ± 0.02
60-70	44	0	2.3 ± 1.7	37.6 ± 7.9	0.271 ± 0.014	0.97 ± 0.02
70-110	1404	0	0.9 ± 2.2	1416.7 ± 38.0	0.280 ± 0.014	0.98 ± 0.01
110-150	28	0	0.0 ± 1.0	28.7 ± 5.9	0.286 ± 0.014	0.99 ± 0.01
150-200	0	0	0.0 ± 0.0	0.0 ± 0.1	0.292 ± 0.015	0.99 ± 0.01
200-600	3	0	0.0 ± 0.0	3.1 ± 1.8	0.310 ± 0.016	0.99 ± 0.01
Muons, $\int \mathcal{L} dt = 83.68 \pm 3.43 \text{ pb}^{-1}$						
Mass	N_{os}	N_{ss}	N_{bg}	N_{corr}	Acceptance	ε_{trig}
11-15	312	77	31.6 ± 18.2	200.3 ± 27.2	0.047 ± 0.002	0.40 ± 0.01
15-20	348	35	49.0 ± 19.5	260.8 ± 28.5	0.163 ± 0.006	0.49 ± 0.02
20-30	303	8	19.2 ± 12.7	278.7 ± 22.6	0.213 ± 0.007	0.56 ± 0.02
30-40	101	0	4.9 ± 6.7	98.2 ± 12.9	0.219 ± 0.007	0.64 ± 0.02
40-50	39	0	4.5 ± 4.2	33.2 ± 8.2	0.216 ± 0.007	0.64 ± 0.02
50-60	24	0	3.0 ± 2.3	18.6 ± 6.1	0.222 ± 0.007	0.64 ± 0.02
60-70	20	0	1.4 ± 1.4	15.6 ± 5.5	0.223 ± 0.007	0.64 ± 0.02
70-110	884	0	0.6 ± 0.1	891.7 ± 30.2	0.228 ± 0.007	0.64 ± 0.02
110-150	25	0	0.0 ± 1.0	25.9 ± 6.0	0.234 ± 0.007	0.64 ± 0.02
150-200	4	0	0.0 ± 0.0	3.8 ± 2.5	0.239 ± 0.008	0.64 ± 0.02
200-600	2	0	0.0 ± 0.0	2.0 ± 1.6	0.255 ± 0.008	0.64 ± 0.02

especially in lower masses; *acceptance*, as determined from the detector simulation (Section 5.2.3); *trigger efficiency*, as determined for each mass bin by simulating the trigger efficiency turn-on curves (see Section 6.1.4); *cosmic filter efficiency*, which was described in Section 7.1 for muons (no uncertainty for electrons); and *identification*, *z vertex*, and *isolation efficiencies*, which were described in Chapter 4. The rows following the individual uncertainties list the total statistical, total systematic, and total (statistical \oplus systematic) uncertainties. In addition, the uncertainties are categorized and listed as follows: common to all electrons (or muons) for all masses, common to both electrons and muons, and unique for each mass range. Common uncertainties exist for all electrons (muons) on the acceptance and identification and isolation efficiencies (same plus cosmic efficiency). Common uncertainties for electrons *and* muons are luminosity and z vertex efficiency. Other uncertainties are considered unique.

Table 8.2: Uncertainty Table for Dielectron Cross-Sections. The values represent the percent uncertainty for each contribution.

	11-15	15-20	20-30	30-40	40-50	50-60	60-70	70-110	110-150
Stat(os-ss)	12.1	6.4	5.4	8.6	14.3	15.5	15.9	2.7	18.9
Luminosity	4.1	4.1	4.1	4.1	4.1	4.1	4.1	4.1	4.1
Bkgd	11.8	2.9	1.8	2.0	17.0	7.3	4.2	0.2	3.6
p_T Scaling	21.7	8.8	2.4	2.6	0.2	0.2	0.2	0.2	0.2
y (SF)	7.1	8.9	1.9	0.7	4.1	1.5	0.1	1.6	1.5
Acceptance:									
cracks	5.0	5.0	5.0	5.0	5.0	5.0	5.0	5.0	5.0
Efficiency:									
Trigger	5.1	4.5	3.5	2.7	2.5	2.2	1.6	1.3	1.4
ID	1.0	1.0	1.0	1.0	1.0	1.0	1.0	1.0	1.0
Z vertex	1.2	1.2	1.2	1.2	1.2	1.2	1.2	1.2	1.2
Isolation	1.9	1.9	1.9	1.9	1.9	1.9	1.9	1.9	1.9
Total Stat	12.1	6.4	5.4	8.6	14.3	15.5	15.9	2.7	18.9
Total Syst	27.1	15.3	8.5	8.1	19.1	10.4	8.2	7.2	8.0
Total	29.7	16.6	10.1	11.8	23.9	18.7	17.9	7.7	20.5
Common Unc.:									
e only	5.4	5.4	5.4	5.4	5.4	5.4	5.4	5.4	5.4
e and μ	4.3	4.3	4.3	4.3	4.3	4.3	4.3	4.3	4.3
Unique Unc.:	28.9	15.1	7.4	9.6	22.9	17.3	16.5	3.4	19.3

Table 8.3: Uncertainty Table for Dimuon Cross-Sections. The values represent the percent uncertainty for each contribution.

	11-15	15-20	20-30	30-40	40-50	50-60	60-70	70-110	110-150
Stat(os-ss)	9.7	7.4	6.4	10.5	18.2	23.5	24.2	3.4	20.0
Luminosity	4.1	4.1	4.1	4.1	4.1	4.1	4.1	4.1	4.1
Bkgd	8.9	7.4	4.6	7.1	12.7	10.8	7.7	0.0	4.0
p_T Scaling	19.1	2.1	4.4	3.6	0.3	0.3	0.3	0.3	0.3
y (SF)	4.8	3.0	1.3	0.1	1.5	1.4	2.5	2.1	1.0
Acceptance:									
cracks	3.1	3.1	3.1	3.1	3.1	3.1	3.1	3.1	3.1
Efficiency:									
Trigger	2.7	4.0	3.5	2.9	3.2	3.5	3.0	3.0	3.1
ID	1.7	1.7	1.7	1.7	1.7	1.7	1.7	1.7	1.7
Cosmic	0.3	0.3	0.3	0.3	0.3	0.3	0.3	0.3	0.3
Z vertex	1.2	1.2	1.2	1.2	1.2	1.2	1.2	1.2	1.2
Isolation	2.1	2.1	2.1	2.1	2.1	2.1	2.1	2.1	2.1
Total Stat	9.7	7.4	6.4	10.5	18.1	23.3	24.1	3.4	20.0
Total Syst	22.6	11.0	9.5	10.3	13.9	12.8	10.4	7.0	7.9
Total	24.6	13.2	11.4	14.7	22.8	26.6	26.2	7.8	21.5
Common Unc.:									
μ only	4.1	4.1	4.1	4.1	4.1	4.1	4.1	4.1	4.1
e and μ	4.3	4.3	4.3	4.3	4.3	4.3	4.3	4.3	4.3
Unique Unc.:	23.9	11.8	9.8	13.4	22.0	25.9	25.6	5.0	20.7

8.1.1 Cross-Section Results

Equation 8.1 was used to calculate the Drell-Yan differential cross-sections ($d^2\sigma/dMdy$ for $|y| < 1$) for the data in Table 8.1. The uncertainties were calculated from Tables 8.2 and 8.3. The results are listed in Table 8.4. Negative cross-section results are shown as zero. Figure 8.1 shows the cross-section results plotted on a log scale and compared to both the Run 0 CDF measurement (hollow squares and triangles) and an $\mathcal{O}(\alpha_s^2)$ theoretical prediction (line). Figure 8.2 shows the combined Run 1B electron and muon results compared to the $\mathcal{O}(\alpha_s^2)$ theoretical prediction.

Table 8.4: Drell-Yan Differential Cross-Section Results. For masses above 150 GeV, the systematic uncertainty was an order of magnitude lower than the statistical uncertainty, and it is not shown here.

Mass bin (GeV/c ²)	Centroid (GeV/c ²)	Dielectron [pb/(GeV/c ²)]	Dimuon [pb/(GeV/c ²)]	Combined [pb/(GeV/c ²)]
11-15	12.7	25.85 ± 3.13 ± 7.01	27.25 ± 2.64 ± 6.16	26.64 ± 5.11
15-20	17.1	7.69 ± 0.49 ± 1.18	6.68 ± 0.50 ± 0.73	7.00 ± 0.75
20-30	23.8	2.58 ± 0.14 ± 0.22	2.36 ± 0.15 ± 0.22	2.48 ± 0.20
30-40	34.1	0.79 ± 0.07 ± 0.06	0.71 ± 0.07 ± 0.07	0.76 ± 0.07
40-50	44.3	0.27 ± 0.04 ± 0.05	0.24 ± 0.04 ± 0.03	0.26 ± 0.04
50-60	54.6	0.18 ± 0.03 ± 0.02	0.13 ± 0.03 ± 0.02	0.16 ± 0.03
60-70	64.9	0.16 ± 0.03 ± 0.01	0.11 ± 0.03 ± 0.01	0.14 ± 0.02
70-110	90.9	1.52 ± 0.04 ± 0.11	1.55 ± 0.05 ± 0.11	1.53 ± 0.09
110-150	122.9	0.03 ± 0.01 ± 0.003	0.04 ± 0.01 ± 0.003	0.03 ± 0.01
150-200	169.1	0.0000	0.0050 ± 0.0025	0.0025 ± 0.0013
200-600	258.2	0.0003 ± 0.0002	0.0003 ± 0.0002	0.0003 ± 0.0001

The mass centroid was determined from the mass distributions of generated Monte Carlo events before running the detector simulation so that the mass distributions would not be shaped by the acceptance cuts. In the lowest mass range, for instance, the kinematic acceptance favors lepton pairs with higher invariant mass.

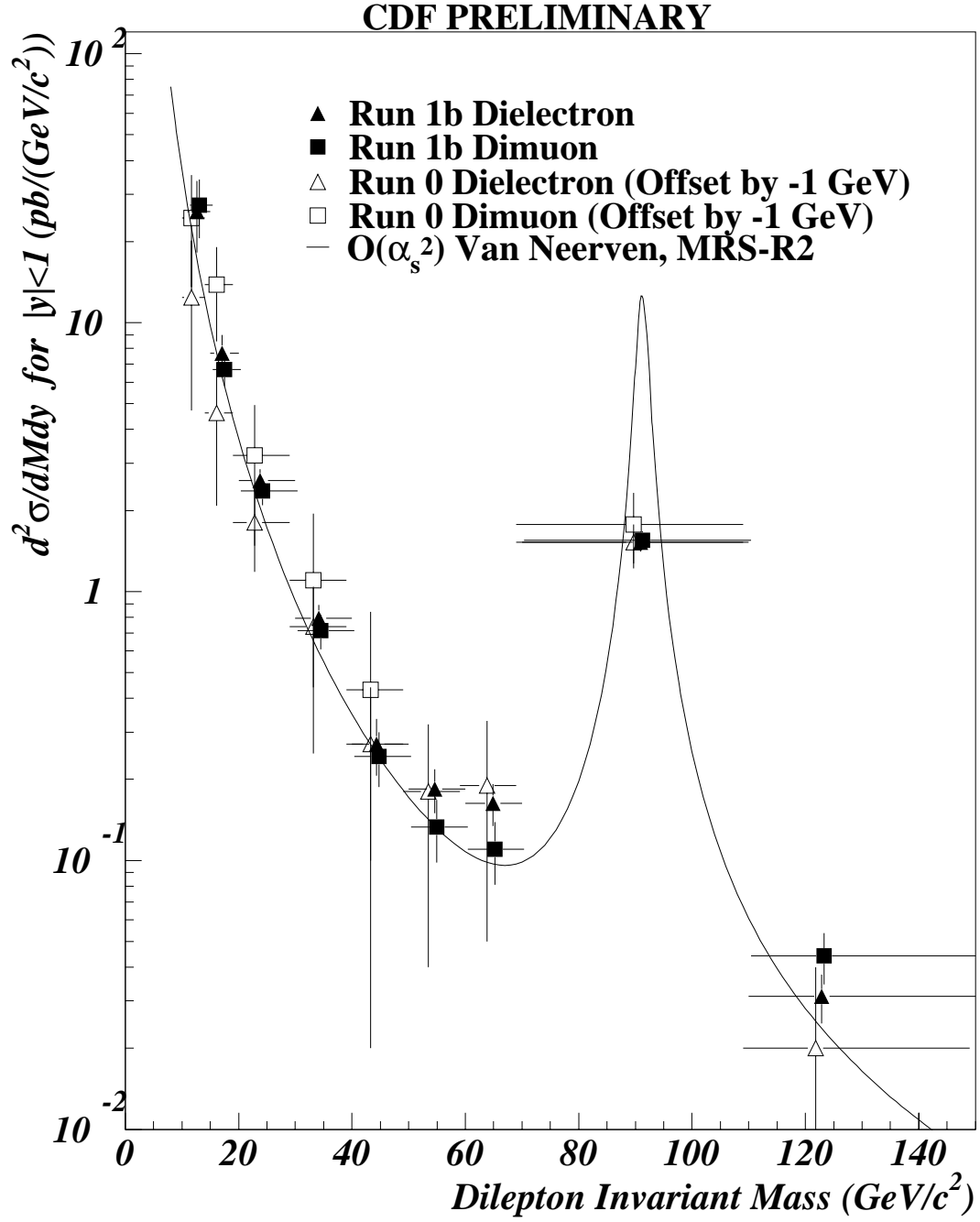


Figure 8.1: Run 1B preliminary Drell-Yan plus Z cross-sections (solid points), as well as published Run 0 cross-sections (open points). Dielectrons and dimuons are plotted separately.

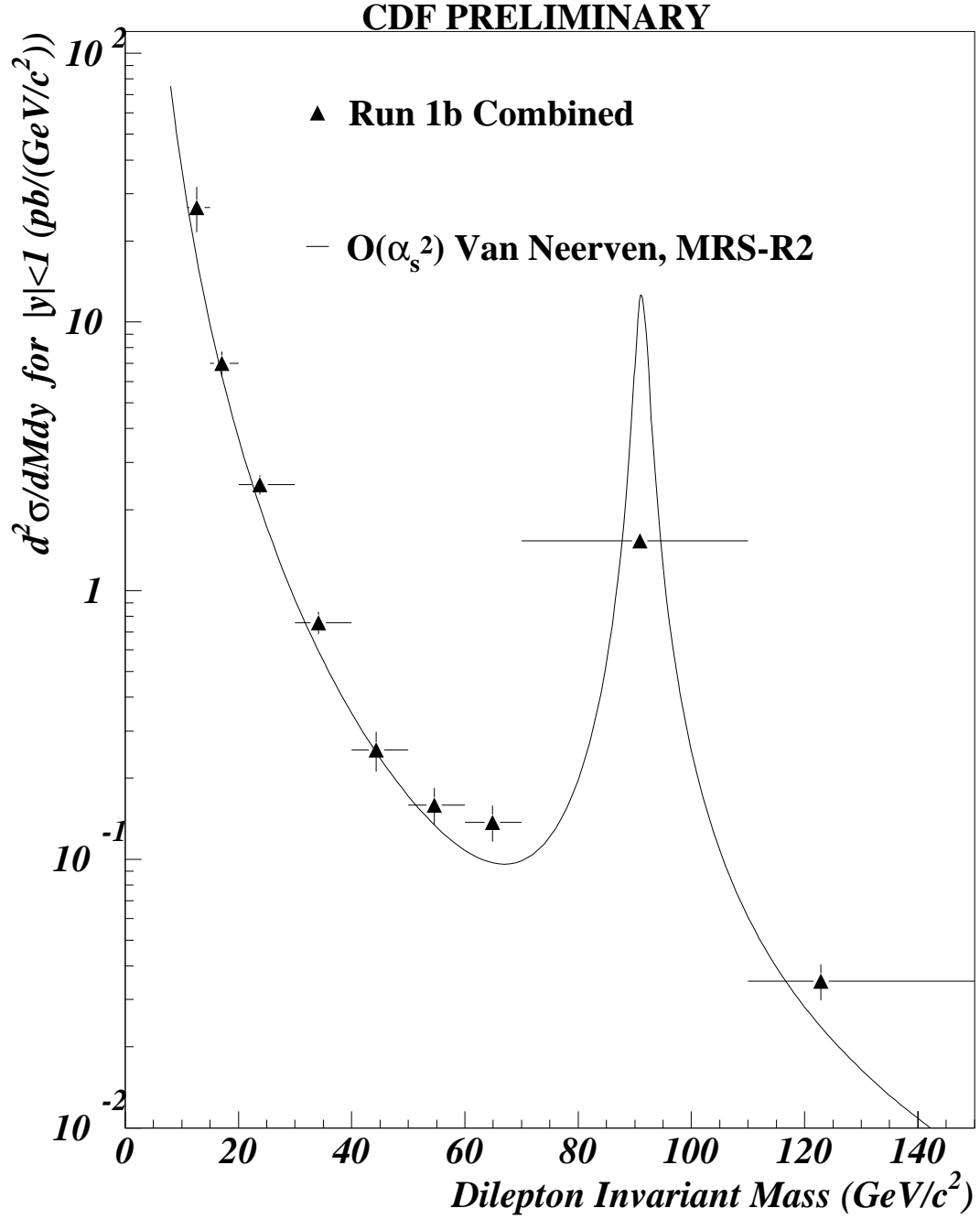


Figure 8.2: Run 1B preliminary Drell-Yan plus Z combined electron and muon cross-sections (points) compared with a NNLO theoretical prediction (line).

The Monte Carlo generated mass centroid for the 11-15 GeV mass bin is 12.7 GeV. With detector and trigger simulations the centroid is 13.2 GeV. This small difference is amplified when the differential cross-section is multiplied by M^3 .

The differential cross-sections were multiplied by M^3 , and the results are shown in Figure 8.3. The plot shows the dielectron (solid triangles) and dimuon (solid squares) cross-sections ($M^3 d^2\sigma/dMdy$ for $|y| < 1$) compared to an $\mathcal{O}(\alpha_s^2)$ theoretical prediction (line). It is clear that all are within reasonable agreement, especially with respect to the shape of the distribution, though the dielectron and dimuon results disagree by more than one sigma.

An attempt was made to quantify the discrepancy between the dielectron and dimuon cross-sections in Figure 8.3. Since the discrepancy appears to be an overall scaling of one or both cross-sections, the weighted average of all the dielectron points in $11 < M_{ll} < 70$ GeV was compared to the weighted average of all the dimuon points in the same mass range. The weighted average for dielectrons, X_{ee} , was found to be 33.30 ± 2.42 nb·GeV², while the weighted average for dimuons, $X_{\mu\mu}$, was found to be 29.27 ± 2.10 nb·GeV². The ratio

$$\frac{X_{ee} - X_{\mu\mu}}{\frac{1}{2}(X_{ee} + X_{\mu\mu})} = 0.129 \pm 0.102$$

should be close to zero if the cross-sections are the same. The measured ratio reveals that when we account for correlated uncertainty, we observe a discrepancy between the dielectron and dimuon cross-section results of less than 1.3 sigma. There is little evidence, therefore, of any physical discrepancy. The combined dielectron and dimuon cross-sections ($M^3 d^2\sigma/dMdy$ for $|y| < 1$) are shown in Figures 8.4 and 8.5.

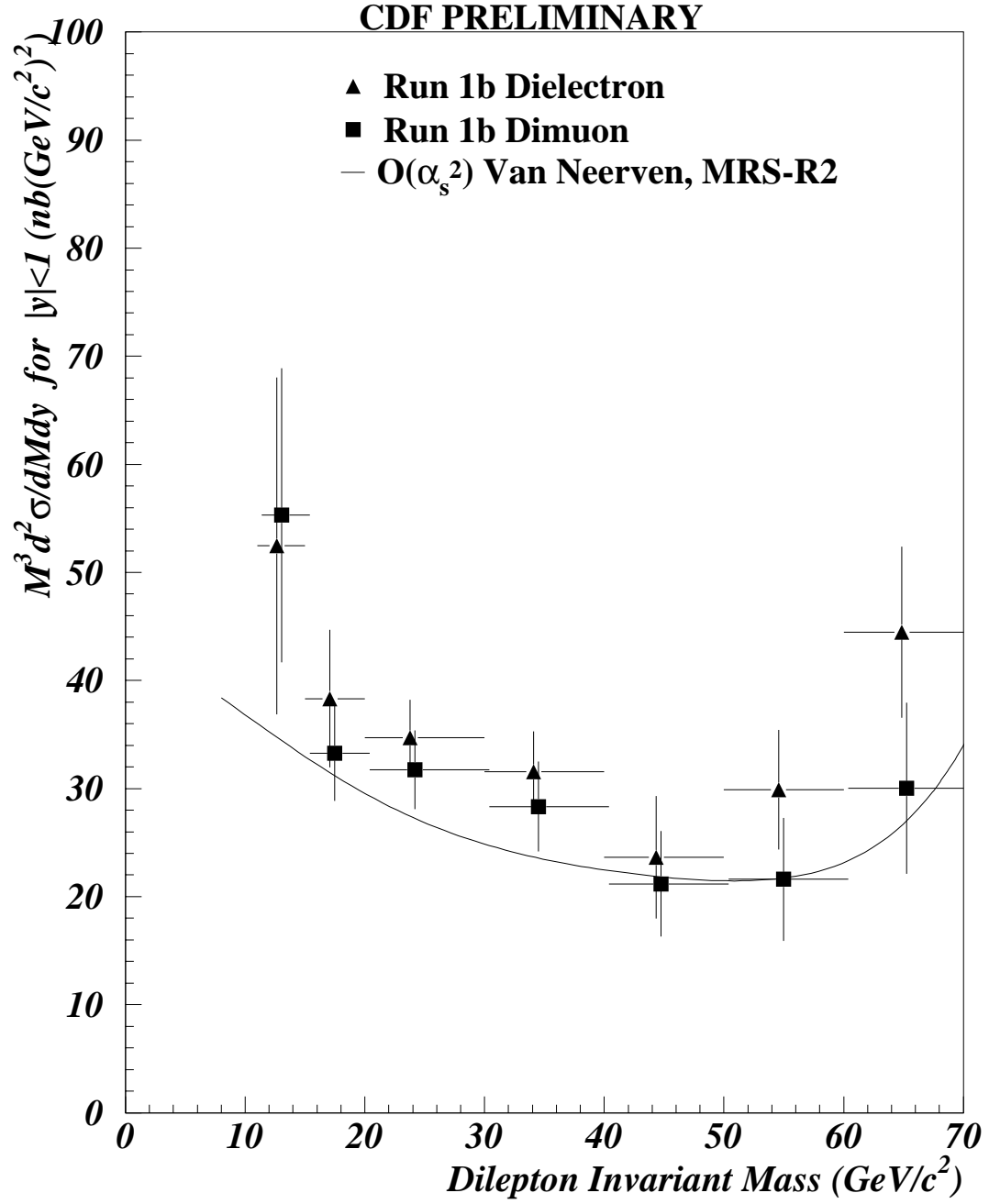


Figure 8.3: Drell-Yan cross-sections scaled by M^3 in the 10-70 GeV/c^2 range below the Z mass region. Dielectrons and dimuons are plotted separately. Data is compared to NNLO theory using the MRS-R2 structure functions and van Neerven corrections^[5].

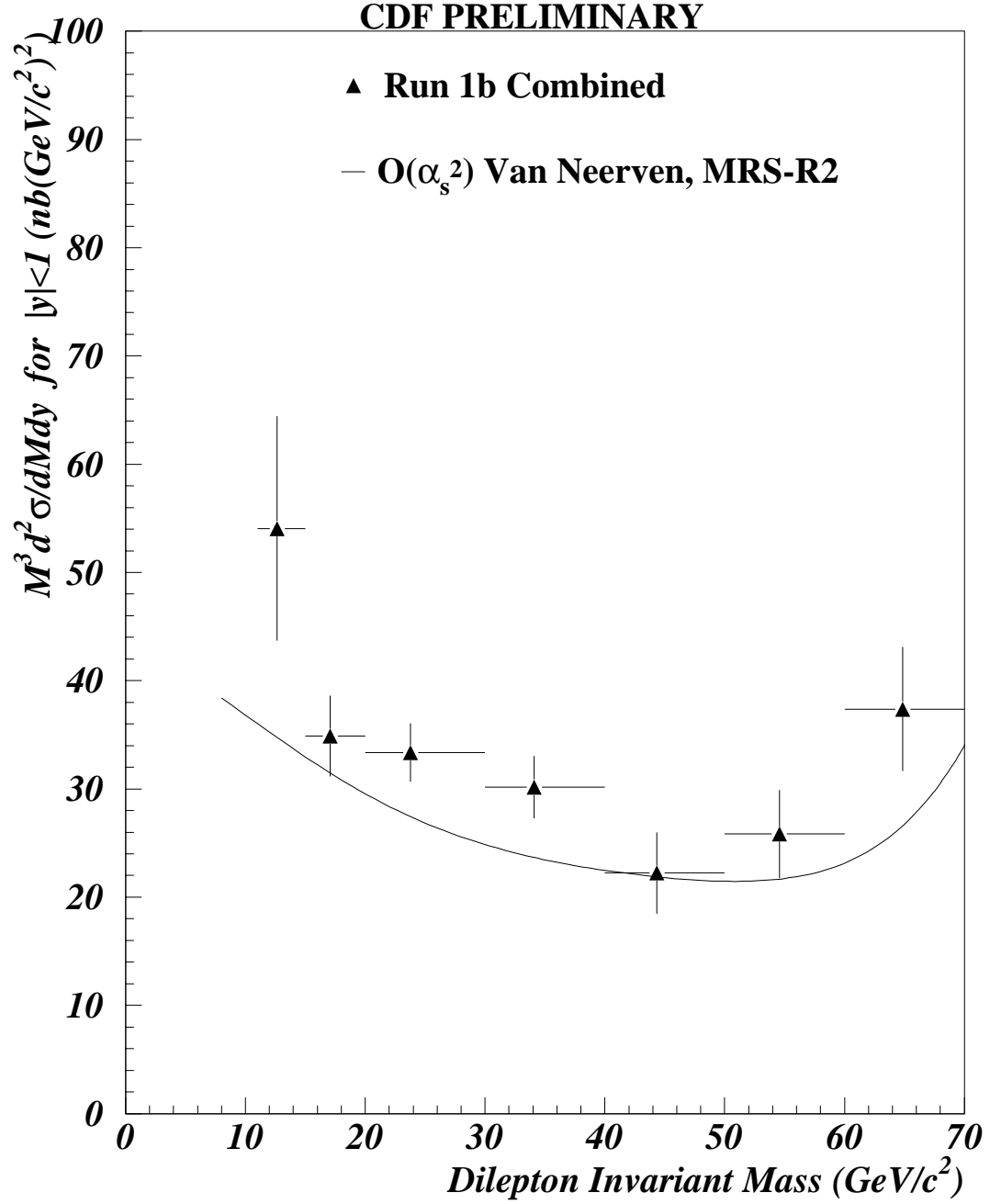


Figure 8.4: Combined Run 1B dielectron and dimuon Drell-Yan cross-sections scaled by M^3 in the 10-70 GeV/c^2 range below the Z mass region. Data is compared to NNLO theory using the MRS-R2 structure functions and van Neerven corrections^[5].

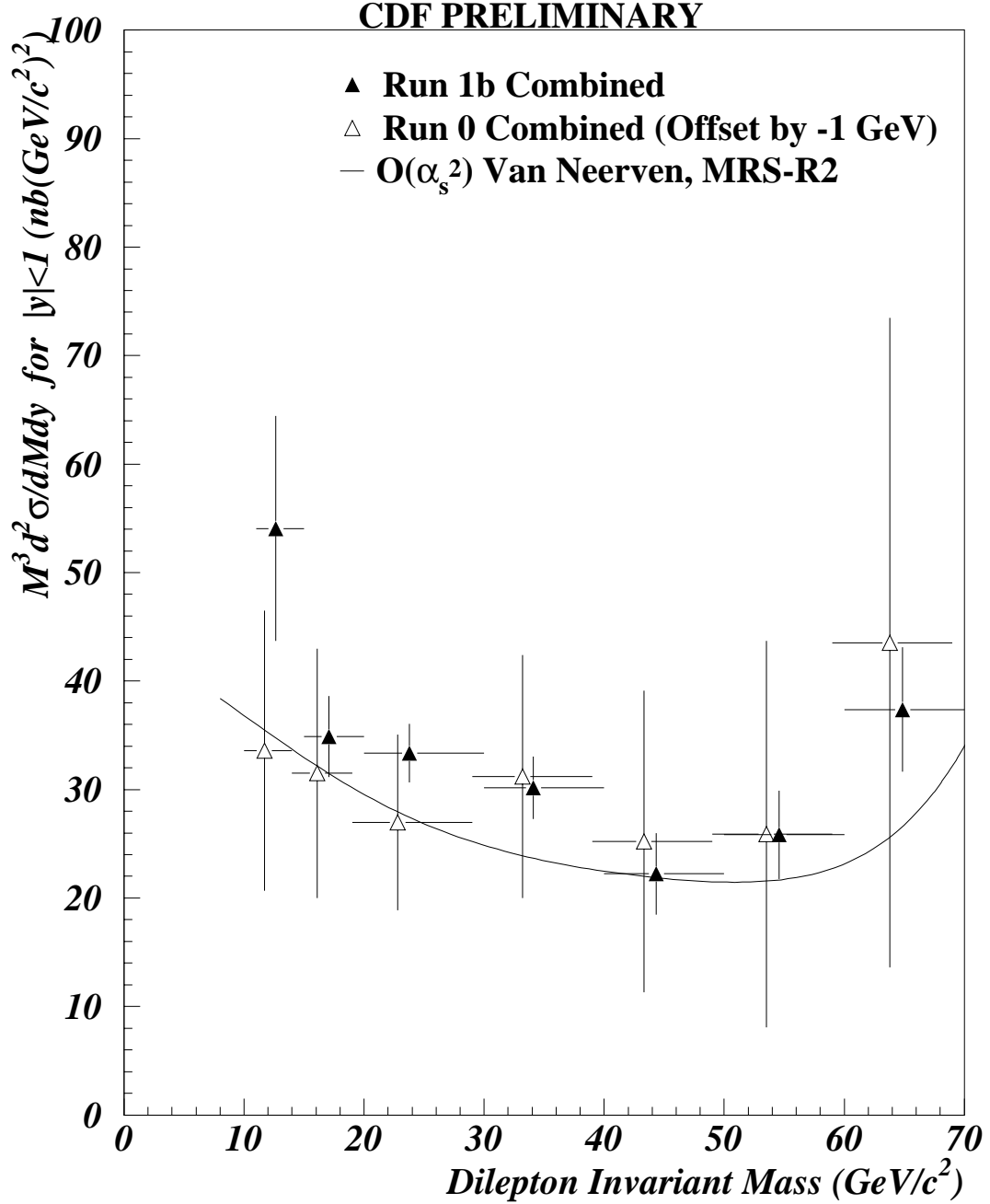


Figure 8.5: Combined dielectron and dimuon Drell-Yan cross-sections scaled by M^3 in the 10-70 GeV/c^2 range below the Z mass region. Run 1B preliminary cross-sections are plotted as solid triangles, while published Run 0 cross-sections are included as open triangles. Data is compared to NNLO theory using the MRS-R2 structure functions and van Neerven corrections^[5].

8.2 Cross Check With Published $\sigma B(Z \rightarrow l^+ l^-)$

The Drell-Yan differential cross-sections in the Z mass window were used to cross check our results with published Z cross-sections, $\sigma B(Z \rightarrow l^+ l^-)$, and with theoretical predictions. The Standard Model dictates that the dielectron and dimuon Z cross-sections, $\sigma B(Z \rightarrow e^+ e^-)$ and $\sigma B(Z \rightarrow \mu^+ \mu^-)$, are equal. The QCD theoretical prediction using MRS-A structure functions is 222 pb^[24].

The Z cross-section was determined with the following equation:

$$\sigma B(Z \rightarrow l^+ l^-) = \left. \frac{d^2 \sigma}{dM dy} \right|_{|y| < 1} \times \Delta M \times \Delta y \times 1.84 \quad (8.2)$$

where ΔM is the width of the Z mass bin (40 GeV for $70 < M_{ll} < 110$ GeV), and Δy is the width of the accepted rapidity range (2 for $|y| < 1$) in the differential cross-section calculation. The factor of 1.84 is the ratio of the theoretical cross-section for $Z \rightarrow l^+ l^-$ including all masses and rapidities to the theoretical cross-section for $\gamma^*/Z \rightarrow l^+ l^-$ in the mass range $70 < M_{ll} < 110$ GeV and the rapidity range $|y| < 1$ ^[23].

The dielectron Drell-Yan differential cross-section 1.52 ± 0.12 pb/GeV corresponds to the cross-section $\sigma B(Z \rightarrow e^+ e^-) = 224 \pm 17$ pb. The dimuon differential cross-section 1.55 ± 0.12 pb/GeV corresponds to the cross-section $\sigma B(Z \rightarrow \mu^+ \mu^-) = 228 \pm 18$ pb. The dielectron and dimuon results agree very well with each other and with the theoretical prediction, and each agrees reasonably well with the most recent CDF publications from the 1992-1995 run: $\sigma B(Z \rightarrow e^+ e^-) = 249 \pm 5 \pm 10$ pb and $\sigma B(Z \rightarrow \mu^+ \mu^-) = 237 \pm 9 \pm 9$ pb^[24].

8.3 Discussion

This analysis has shown that Run 1B data will allow a measurement of low-mass Drell-Yan production with much better statistical precision than previous measurements, including the CDF Run 0 analysis. This analysis also differs from the Run 0 analysis by a more efficient definition of the isolation cut, a mass bin-dependent normalization of the background from heavy flavor, and the consideration of $Z \rightarrow \tau^+\tau^-$ backgrounds that were not included in the previous analysis. We did not confirm the discrepancy between electron and muon cross-sections that appeared in the Run 0 results. Instead, we measured a $1.3\ \sigma$ difference in the *opposite* direction. There is little evidence of any physical discrepancy in electron and muon cross-sections.

Overall, both the electron and muon Drell-Yan differential cross-sections clearly confirm the shape of the theoretical prediction, though both results were found to be consistently higher than the theoretical prediction. One reason for the discrepancy is that the theoretical prediction does not include all $\mathcal{O}(\alpha_s^2)$ corrections, and it does not include any higher-order corrections beyond $\mathcal{O}(\alpha_s^2)$. Furthermore, Figure 2.5 shows that the predicted cross-sections have increased as newer structure functions have been developed. The results of this analysis indicate that the theory may need more adjustment of the flux of low- x partons in the proton.

Appendix A

Identification Efficiency Method

We define N_Z the number of selected Z events; N_{TT} the number of these events where both leptons pass tight cuts; N_{CT} the number of Z events where one lepton passes tight cuts and the other passes the cut or set of cuts we are interested in; and N_{MT} the total number of events in which one lepton passes the tight cuts and the other passes only a minimal set of cuts, for instance the requirement that an ELES bank have been made.

$$N_{CT} = (\varepsilon_T^2 + \varepsilon_T(\varepsilon_C - \varepsilon_T) + (\varepsilon_C - \varepsilon_T)\varepsilon_T)N_Z \quad (\text{A.1})$$

$$N_{CT} = (2\varepsilon_C\varepsilon_T - \varepsilon_T^2)N_Z \quad (\text{A.2})$$

Similarly,

$$N_{MT} = (2\varepsilon_M\varepsilon_T - \varepsilon_T^2)N_Z \quad (\text{A.3})$$

$$N_{TT} = \varepsilon_T^2 N_Z \quad (\text{A.4})$$

If we assume that $\varepsilon_M = 1$, we can manipulate the above equations to get

$$\varepsilon_C = \frac{N_{CT} + N_{TT}}{2\varepsilon_T N_Z} \quad \text{and} \quad (A.5)$$

$$2\varepsilon_T N_Z = N_{MT} + N_{TT} \quad (A.6)$$

which reduce to

$$\varepsilon_C = \frac{N_{CT} + N_{TT}}{N_{MT} + N_{TT}}. \quad (A.7)$$

Equation A.7 can be abbreviated

$$\varepsilon_C = \frac{N_C + N_{TT}}{N_{tot} + N_{TT}}. \quad (A.8)$$

The uncertainty of the efficiency (A.8) was calculated by assuming binomial statistics.

$$\sigma_{binomial} = \sqrt{\frac{p(1-p)}{n}} \quad (A.9)$$

$$\sigma_{\varepsilon_C} = \sqrt{\left(\frac{1}{N_{tot} + N_{TT}}\right) \left(\frac{N_C + N_{TT}}{N_{tot} + N_{TT}}\right) \left(1 - \frac{N_C + N_{TT}}{N_{tot} + N_{TT}}\right)} \quad (A.10)$$

In summary, the efficiency for a cut or set of cuts C is found to be

$$\varepsilon_C = \frac{N_C + N_{TT}}{N_{tot} + N_{TT}} \pm \sqrt{\frac{(N_C + N_{TT})(N_{tot} - N_C)}{(N_{tot} + N_{TT})^3}}. \quad (A.11)$$

Bibliography

- [1] Sidney D. Drell and Tung-Mow Yan, Phys. Rev. Lett. **25**, 316 (1970).
- [2] J. H. Christenson *et al.*, Phys. Rev. Lett. **25**, 1523 (1970).
L. M. Lederman and B. G. Pope, Phys. Rev. Lett. **27**, 765 (1971).
- [3] W. J. Sterling and M. R. Whalley, J. Phys. G: Nucl. Part. Phys. **19** (1993) D1.
“A compilation of Drell-Yan cross sections.”
- [4] F. Abe *et al.* Phys. Rev. D **49**, 88 (1994).
“Measurement of Drell-Yan electron and muon pair differential cross sections in $\bar{p}p$ collisions at $\sqrt{s} = 1.8$ TeV.”
K. Bloom *et al.*, “Low Mass Drell-Yan in the Dielectron Channel,” CDF Note 1622 (1991).
V. Scarpine *et al.*, “Analysis of the Low Mass Dimuon Drell-Yan Differential Cross Section,” CDF Note 1523 (1993).
- [5] W. L. van Neerven and E. B. Zijlstra, Nucl. Phys. B **382**, 11 (1992).
“The $O(\alpha_s^2)$ corrected Drell-Yan K -factor in the DIS and \overline{MS} schemes.”
- [6] F. Abe *et al.*, Phys. Rev. D **50**, 2966 (1994).
D. Amidei *et al.*, Nucl. Instrum. Methods A **350**, 73 (1994).
- [7] J. P. Done *et al.*, “SUSY Dilepton Selection for Run I,” CDF Note 4446 (1998).
- [8] M. Worcester, D. Saltzberg, J. Nachtman, “Development of New Isolation Variables and Estimation of Fake Rates in Dilepton SUSY Searches at CDF,” CDF Note 5081 (1999).
This note shows that the muon isolation is unchanged when the adjacent ϕ tower is removed from the isolation calculation, while the electron isolation changes by 20%.
- [9] A. Beretvas *et al.*, “Event z Vertex Cut Efficiency as a Luminosity Correction for Run Ib,” CDF Note 5066 (1999).
- [10] M. Krasberg, T. LeCompte, “CMCOS: The Run 1A Cosmic Ray Filter,” CDF Note 2032 (1993).

- [11] A. Scott, J. Hauser, D. Saltzberg, P. Murat, “An Effective Cosmic Ray Filter for Run 1 Dimuon Analyses,” CDF Note 4755 (1998).
- [12] B. Tannenbaum, “Instructions for SIGMON,” CDF Note 2962 (1995).
- [13] J. Wahl, “Electron Identification and Trigger Efficiencies,” CDF Note 4601 (1999).
- [14] K. Maeshima *et al.*, “Search for Pati-Salam Leptoquarks via the decays $B_s \rightarrow e^\pm \mu^\mp$ and $B_d \rightarrow e^\pm \mu^\mp$,” CDF Note 4224 (1998).
- [15] J. P. Done *et al.*, “Study of Run-1B Lepton Identification Efficiencies for SUSY Searches,” CDF Note 4218 (1997).
- [16] A. Clark *et al.*, “Search for the Rare Decays $B_d^0 \rightarrow \mu^+ \mu^-$ and $B_s^0 \rightarrow \mu^+ \mu^-$ using Run IA and Run IB data,” CDF Note 3715 (1997).
- [17] T. A. Keaffaber *et al.*, “Measurement of the B^+ Meson Differential Cross Section Using the Exclusive Decay $B^\pm \rightarrow J/\psi K^\pm$,” CDF Note 4911 (1999).
- [18] D. Kestenbaum and P. Schlabach, “A Measurement of the CMX stub reconstruction efficiency,” CDF Note 3115 (1995).
- [19] G. Marchesini, B. R. Webber, G. Abbiendi, I. G. Knowles, M. H. Seymour and L. Stanco, Computer Phys. Comm. **67** 465 (1992).
- [20] E. Barberio and Z. Was, Computer Phys. Comm. **79**, 291 (1994); E. Barberio, B. van Eijk, and Z. Was, Computer Phys. Comm. **66**, 115 (1991). PHOTOS is part of the LUND package.
- [21] W. K. Sakumoto *et al.*, “Drell-Yan Radiative Corrections,” CDF Note 3497 (1996).
- [22] C. Caso *et al.*, Eur. Phys. J., C3(1-4), 1998. “Review of Particle Physics.”
- [23] The correction factor was determined by Willis Sakumoto by calculating these NLO cross sections: $\sigma(Z, \text{ all masses and rapidities}) = 225.4 \text{ pb}$ and $\sigma(|y| < 1, 70 - 110 \text{ GeV}) = 122.5 \text{ pb}$. The ratio is 1.84.
- [24] T. Affolder *et al.*, Phys. Rev. Lett. **84**, 845 (2000).